

# POLITECNICO DI TORINO

Collegio di Ingegneria Energetica

**Corso di Laurea Magistrale  
in Ingegneria Energetica e Nucleare**

Tesi di Laurea Magistrale

## **Development of a high thermal energy storage device with Form-Stable Phase Change Materials (FPCMs)**

Investigation of structure-property links under performance and costs  
constraints.



### **Relatori**

prof. Andrea Lanzini

prof. Adriano Sciacovelli

### **Candidato**

Serena Ditroia

Ottobre 2018

<b>Acknowledgements</b> .....	3
<b>Abstract (italiano)</b> .....	4
<b>Abstract</b> .....	6
<b>Nomenclature</b> .....	7
<b>1 Scope and motivation</b> .....	8
<b>2 Introduction</b> .....	10
2.1 <i>Thermal Energy Storage (TES)</i> .....	10
2.2 <i>Phase Change Materials (PCM) for Latent Heat Thermal Energy Storage (LHTES)</i> .....	13
2.3 <i>Form-Stable solutions for PCMs</i> .....	17
2.4 <i>Form-Stable Phase Change Materials (FPCMs)</i> .....	19
2.5 <i>Form-Stable PCMs Screening Maps</i> .....	22
<b>3 Experimental methods</b> .....	24
3.1 <i>Differential Scanning Calorimetry (DSC)</i> .....	26
3.2 <i>Laser Flash Apparatus (LFA)</i> .....	27
3.3 <i>Helium Pycnometer (HP)</i> .....	29
3.4 <i>Dilatometry Analysis</i> .....	30
3.5 <i>Scanning Electron Microscope (SEM) and Electron Differential Scanning (EDX)</i> .....	31
3.6 <i>X-Ray micro-Tomography (XRT)</i> .....	34
3.7 <i>Digital Image post-processing for micro-structural investigation</i> .....	37
<b>4 Experimental results</b> .....	42
4.1 <i>Materials experimental selection and characterization</i> .....	42
4.2 <i>Fabrication of the pellets</i> .....	42
4.3 <i>Density and porosity measurements</i> .....	51
4.4 <i>Thermal characterization of the formulations</i> .....	54
4.5 <i>Dilatometry Analysis</i> .....	63
4.6 <i>Complementary micro-structural analysis</i> .....	67
<b>5 Considerations on the development of a LHTES device</b> .....	81
5.1 <i>Conceptual design and system requirements</i> .....	81
5.2 <i>Cost of Storage evaluation methodology</i> .....	83
<b>Conclusions</b> .....	94
<b>Bibliography</b> .....	98

## **Acknowledgements**

I am very thankful to Adriano Sciacovelli and to the Birmingham Centre for Energy Storage (BCES) for giving me the opportunity to develop this project in a motivating environment. Special thanks go to Helena Navarro who supervised all the experimental learning process and to Shivangi Sharma's encouragement throughout.

## **Abstract (italiano)**

Lo scopo principale del presente studio è legato alla selezione, caratterizzazione e analisi sperimentale di materiali compositi a cambiamento di fase, ossia Phase Change Materials (PCM), per l'accumulo di energia termica sotto forma di calore latente accumulato e rilasciato durante le transizioni di fase (solido-solido, solido-liquido, liquido-gas). Lo sfruttamento di tali processi consente alle tecnologie per calore latente, ossia 'Latent Heat Thermal Energy Storage' (LHTES), di operare in maniera reversibile sia come sorgenti che da pozzi di calore.

Dati i recenti obiettivi posti durante la Conferenza sul clima di Parigi (COP21) volti alla decarbonizzazione e al contenimento delle emissioni con l'obiettivo di limitare gli effetti del surriscaldamento globale limitandolo ben al di sotto dei 2°C, lo studio e la ricerca di tecnologie di accumulo sono una valida e sostenibile alternativa per immagazzinare energia sotto diverse forme. Soluzioni di accumulo termico hanno dimostrato di conferire maggior resilienza a grossi impianti di produzione di elettricità [1] o ad altri processi industriali fortemente energivori [2,3] e di garantire una maggior robustezza quando integrati ad impianti che sfruttano fonti rinnovabili intermittenti e caratterizzate da una sfasatura tra produzione e domanda di energia.

La fabbricazione e lo studio di pellets di materiali a cambiamento di fase a forma stabile (Form-Stable PCM) sono una soluzione compatta e pulita per immagazzinare alti contenuti di densità energetiche sfruttando sia il calore latente del PCM selezionato a base di Sale Solare (60% NaNO<sub>3</sub> e 40% KNO<sub>3</sub> in massa) e la componente di calore sensibile principalmente conferita dall'alta capacità termica di un materiale di supporto che è il principale responsabile della formazione di una matrice porosa strutturalmente e di forma stabile. Il mescolamento, la compressione uniassiale e sinterizzazione del Sale Solare con Vermiculite come materiale di supporto e Grafite come componente aggiuntivo per il miglioramento delle prestazioni termiche contribuiscono alla formazione di microstrutture interne che contengono e prevengono il rilascio di PCM verso l'ambiente esterno, problema principale legato allo sviluppo e alla controllabilità dei processi di fabbricazione di tali pellets.

Il focus principale del lavoro presentato include dunque l'analisi dell'affidabilità e replicabilità del processo di produzione dei pellets e l'indagine approfondita sul concetto di stabilità di forma di tali PCM e sui meccanismi che guidano e determinano la formazione della matrice porosa andando alla ricerca dei collegamenti tra caratteristiche microstrutturali e performance termiche. Questo studio è reso possibile facendo affidamento su macchinari e ripetuti test di laboratorio utilizzati per la caratterizzazione di materiali compositi insieme allo sviluppo di una parallela analisi di immagini digitali acquisite tramite Tomografia computerizzata per confrontare e validare in maniera separata e imparziale i risultati prodotti da software di post-processing. L'analisi morfologica e topologica è stata completata in maniera semi-quantitativa dall'utilizzo di microscopio elettronico 'Scanning Electron Microscope' e per spettroscopia EDX.

Lo studio delle performance termiche di sei formulazioni iniziali è stato invece condotto adottando principalmente tecniche di analisi calorimetrica differenziale ‘Differential Scanning Calorimetry’ e tecnica laser tramite ‘Laser Flash Analyzer’.

Il carattere fortemente sperimentale a livello microscopico dello studio dei materiali svolto ha posto le basi per una indagine preliminare a livello di dispositivo proponendo un design concettuale per una possibile applicazione dei pellet a forma stabile assemblati in un teorico reattore di tipo ‘packed-bed’. La panoramica generale presentata sulla valutazione a livello di sistema è completata evidenziando alcuni indicatori di tipo economico e di performance che posizionano i PCM a forma stabile tra le possibili soluzioni future, insieme ad altre tecnologie di accumulo termico, per sostenere il passaggio da una produzione di energia dominata dalle fonti fossili verso un maggior e più sicuro sfruttamento delle fonti rinnovabili.

Il valore aggiunto fornito dal presente lavoro verso il settore della ricerca delle tecnologie di accumulo consiste nell’approfondire la conoscenza dei materiali ad accumulo latente a forma stabile fornendo un’interpretazione dei risultati sperimentali a più ampio respiro strettamente collegati al metodo fabbricazione adottato, e allo stesso tempo riempiendo i vuoti presenti nello stato dell’arte riguardo alle proprietà termo-fisiche dei materiali.

Sebbene questo studio fornisca una prospettiva più dettagliata sulle questioni legate alla stabilità di forma dei PCM e su come questa sia ottenuta da processi affidabili ed economicamente non dispendiosi come la compressione e sinterizzazione di materiali in forma di polvere, una ricerca più approfondita deve essere rivolta verso queste tematiche estendendola ad altri materiali e proponendo diversi approcci per lo studio microstrutturale dei materiali compositi richiamando, allo stesso tempo, l’attenzione dei responsabili delle politiche e decisioni a livello comunitario in tema di per incentivarne la ricerca e una più facile e guidata commercializzazione.

## Abstract

The need for reduction of fossil fuel exploitation along with their emissions as well as the urgency of coping with the latest challenges arose in the energy sector in the last decades to sustain and to make the well-known renewables more resilient, have pushed towards the development of new TES solutions. The manufacturing of Form-Stable Phase Change Materials (FPCM) offer a sustainable, clean, flexible and compact option for collecting thermal energy thanks to their ability of storing higher energy density contents compared to the traditional sensible energy storage-based solutions and proving to be a more effective option for a wider range of temperature applications. The selection, mixing and compressing of a Solar Salt eutectic mixture with a supporting material and a carbon-based component allowed the thermal properties enhancement and, at the same time, the controlled sintering procedure prevented the typical leakage issues of common PCM-based solutions confirming the replicability of the whole procedure. In this no emissions-driven panorama, this study offers a comprehensive overview of the thermo-physical and microstructural investigation of the FPCMs.

Main focuses of the present study have been: the assessment of a reliable thus replicable manufacturing procedure to fabricate the pellets, the investigation on the shape-stability concept connected to the FPCMs in order to find the links between micro-structural features and thermal performances, the development of a parallel digital imaging technique to assess, compare and validate in an unbiased and independent way the reliability of some structural results obtained with existing technologies for the characterization of the samples studied.

Differential Scanning Calorimetry (DSC) and Laser Flash Analyzer (LFA) have been adopted for thermal characterization of six starting formulations selected for the analysis. In a second stage, the complementary use of Scanning Electron Microscope (SEM) and X-Ray micro-tomography (XRT) allowed to shed a light onto the morphology and topology of the shape-stabilized tablets manufactured based onto three final and more performing formulations.

The purpose of this study has then been twofold: the experimental characterization of the materials involved into a micro-scale investigation and a device-scale preliminary evaluation of some key performance indicators related with the cost of storage of FPCMs with some suggestions for further cost and performance-based analysis. The added value of this work to the scientific literature consists on increasing the knowledge on FPCMs filling the present gaps for what thermo-physical properties are concerned as well as to offer a different perspective and insights onto the testing and manufacturing procedure adopted to help developing such new solutions in order to walk their commercialization into the market and to allow policy-makers and stakeholders to favour their production for a future wide applicability range.

## **Nomenclature**

### Abbreviations:

TES – Thermal Energy Storage

LHTES – Latent Heat Thermal Energy Storage

PCM – Phase Change Material

FPCM or SSPCM – Form-Stable or Shape-Stable Phase Change materials

HTF – Heat Transfer Fluid

### Experimental Techniques:

DSC – Differential Scanning Calorimetry

SEM – Scanning Electron Microscope

EDX – Energy Dispersive X-Ray Analysis

micro XRT – X-Ray micro-Tomography

LFA – Laser Flash Analysis

HP – Helium Pycnometer

## 1 Scope and motivation

The topic of FPCMs is a relatively new subject when dealing with Energy Storage (ES) solutions in the development of the energy sector. It is part of the Thermal Energy Storage (TES) technologies which have been investigated for the last decades as a result of the increasing need of containing the greenhouse gas emissions coming from direct primary energy consumption (e.g. fossil fuel burning) and especially from the necessity of recover in a useful way the un-exploited waste heat coming from production processes and other facilities or power plants as a source for extra energy production. As a consequence, the energy sector must not be seen as a static and independent field, it is instead an evolving machine influenced by many variable factors leading to an increasing urge to re-shape the global energy landscape.

For this reason, one of the main debated issues worldwide in the latest years has been denoted as the Energy Transition (ET) which reflects this need of reshaping the future of energy production and of adapting the basic human living needs along with the need for decarbonization. This necessity has been explicated as ET and boosted by COP21 goals defined by the Paris Agreement to solve global warming and by the outstanding population growth and its growing living needs with and uncontrollable and continuously increasing demographic trend. As discussed by many intergovernmental bodies, the term energy transition has been defined as the structural changeover of the energy systems from the current energy production and distribution systems relying mainly onto fossil fuels consumption to low-carbon and more efficient ones. It is believed that ET will encourage new energy models development and policy change, a more oriented research and financing and cost and energy markets turnover.

Even though this is still a slow process due to the inertia caused by the existing infrastructure and still dominating role of the fossils, nonetheless a lot of effort in the research world is being put on finding and testing new technologies to foster the change and to persuade stakeholders and decision-makers towards new solutions like TES. Most of nowadays' power plants, factories and energy supply infrastructures present long lifetime and are replaced/renewed slowly, the inaccessibility of remoted areas and the large amount of fossil resources in regions where energy transition is more expensive rather than exploiting the existing sources are main contributors of this slow process. [5] [7] Policies and government support may accelerate new efficient solutions to gain market share and affect cost deflation decreasing it. [4]

In addition to these drivers, the main reasons for the emerging figure of the TES storage technologies is strictly connected to the matching energy demand and supply of Renewable energy technologies to sustain energy supply in periods of scarce availability or the resources and to collect the surplus produced when large amount of the resource is available. Renewables have always been considered the solution for a more sustainable production and distribution of energy, but their intermittence constitute the main limitation requiring additional integrated solutions.

“Current trends in energy supply and demand are economically, environmentally and socially unsustainable since energy-related emissions of carbon dioxide are expected to be doubled by 2050 and fossil energy demand is expected to be increased over the security of supplies. The International Energy Agency (IEA) recognizes energy storage technologies as a tool to support energy security and climate change goals by helping to integrate electricity and heat systems.” [1]

According to all the reasons outlined, more attention has been paid to look for more safe, reliable and innovating thermal energy storage materials. As composites for LHTES have proved to be a valid solution to take part in the ET process, form-stable PCMs have been deeply investigated for these purposes.

This study reflects indeed the need for finding actual new solutions or materials as well as digging in deeper to existing ones related to PCM-based composites.

As a guideline for the reader, the hereby discussion has been organized into five main Chapters each with subsections providing insights on a specific aspect and challenging issues connected to that topic. Figure 1 shows the main structure of the discussion, where from an overview on the state of the art of the existing technologies in the thermal energy storage panorama, this thesis, taking advantage of the experimental testing, has been built in a top-down structured approach where specific key features related with the formulation, fabrication and performance of the FPCMs, are singularly assessed as part of the main concept of form-stability.

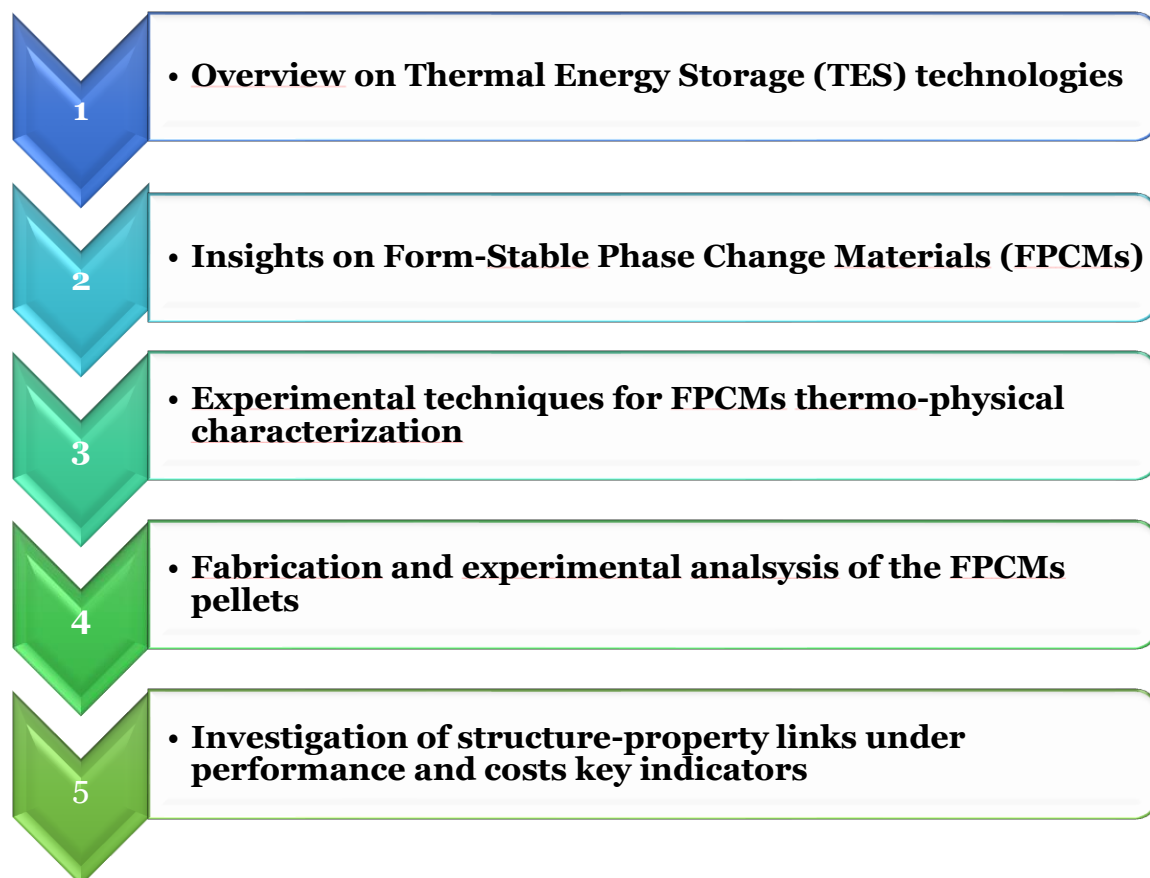


Figure 1 - Roadmap of the thesis.

## 2 Introduction

### 2.1 Thermal Energy Storage (TES)

All the energy required to fulfil the world's population primary living needs, ranging from heating and cooling, transportation, electricity and so on, come from stored types of energy. These sources of energy have historically been achieved by fossil fuels like hydrocarbons in their chemical form. The energy stored usually undergoes transformations from one form to another to allow to be converted from a stored form to a usable one, for example the electrochemical energy collected in batteries can be used in a second moment in the form of electricity when required.

The need of driving decarbonization without changing significantly the standards of our lives along with the imposed action of keeping global warming well above 1.5°C as set by the second article of the Paris Agreement, has paced the increasing interest towards novel energy storage technologies to construct more resilient production and supply systems and to sustain renewables. In addition, the necessity to provide a safe energy supply also in areas where the transmission and distribution of electricity for instance are problematic, have also raised the demand for the integration of such kind of technologies allowing to provide robustness to those systems. The spreading out of energy storage solutions may also serve as a tool to equally guarantee the same access to energy supply and to contribute also to human and social development in critical and isolated areas. Despite taking along risks connected with them, numerous are the objectives being posed for these shared goals.[5]

Nowadays, many are the technologies developed according to the forms energy which can be exploited. Most common types of energy storage technologies currently range from:

- Mechanical storage: hydraulic and/or mechanical systems (e.g. hydro-pumping systems and Compressed-Air Energy Storage (CAES));
- Thermal systems: sensible, latent heat and electrochemical;
- Electrochemical: batteries, electrolyzers;
- Biologic systems: biomass, biofuels;
- Magnetic systems;
- Hydrogen production and storage.

Regardless their potential and preferential applicability and suitability towards renewables-based systems, still most part of the world's resources share is oriented towards the fossil's burning. Oil has confirmed its world leading place for energy consumption with a value of 32.9%, while at the second place, coal is responsible for 30% of primary energy consumption, with a 40% of hard and lignite coal being the world's first power generation source. Along with these sources, natural gas with a share of 24% primary energy demand is expected to increase and it's considered one of the preferential routes towards a cleaner energy sector for the future.[6] Even if the fossil-based sources are experiencing a progressive decline in the past decade, they still own most the highest percentage of share compared to all the other sources altogether.

The urge to operate this Energy Transition at every level have fostered in the past decades the energy debate from a local to an international level to discuss about how to cope with what has been defined by the World Energy Council as the Energy Trilemma [7,8]. Where the “energy trilemma” concept involves energy security, equity and environmental sustainability, namely to “ensure a reliable and accessible energy supply worldwide while guaranteeing global warming targets and improved efficiency infrastructure”.[6]

As a specific category amongst other energy storage solutions, Thermal Energy Storage (TES) technologies allow to store the thermal energy by heating or cooling storage materials. The heat can be either collected from industrial plants or facilities, from Concentrated Solar Power Plants (CSP) and for a wide variety of other waste-heat processes and temperatures providing a sustainable and valid solution.

In more detail, when TES solution are integrated to renewables, the mismatch between demand and production of thermal energy not only leads to increased demand of fuels but also to the increase of the dissipated thermal energy into the environment resulting in wastage. In addition to this, human activities keep on requiring more and more heat, especially in the domestic sector.

TES materials are able to store the surplus of heat produced in order to be reused later on and, according to their thermophysical properties, TES solutions can rely on specific basic thermophysical or chemical principle. TES can therefore be classified into sensible, latent and thermochemical heat storage systems.

**Sensible Energy Storage (STES):** materials adopted in this sector experience an increase of temperature  $\Delta T$  [°C] without changing their physical structure. The amount of heat stored  $Q_{Sensible}$  in this case is directly dependent onto the material’s density  $\rho$  [kg/m<sup>3</sup>], specific heat  $c_p$  [kJ/(kg\*°C)] and temperature drop  $\Delta T$  [°C]. Where  $m$  [kg] is the mass of the sensible material chosen and the specific heat is a temperature-dependent property.

$$Q_{Sensible} = m * \int_{T_{LOW}}^{T_{HIGH}} c_p(T) * dT$$

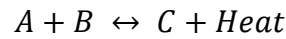
The most used are water with specific heat 4.184 kJ/(kg\*°C) that can be used both as Heat Transfer Fluid (HTF) and storing medium, Molten Salts widely used in current CSP plants and a wide range of Thermal Oils with lower heat capacity over a wider temperature range without phase transition but poor heat transfer properties. Another common solution is adopting naturally available earth materials as fillers (like rocks, sand, concrete blocks...) for thermocline tanks in direct contact with an external HTF.

**Latent Heat Storage (LHTES):** phase changing materials (PCM) are heated up to their melting point storing heat both for sensible contribution but mainly thanks to enthalpy of fusion during their nearly isothermal phase transition. This concept will be deeply addressed in Section 2.

**Thermochemical Energy Storage (TCM):** this heat storing process involving a totally reversible chemical reaction and sorption processes, in particular adsorption and absorption where a sorbent and a sorptive materials are involved in a surface or bulk absorption phenomenon respectively. The distinction amongst these are related to the inter-molecular forces established between the reactants. A whole cycle includes three phases which are schematized in Figure 2 – (right): Charging, Storage and Discharging phases. Once heat is

provided and the temperature is higher than the inversion temperature of the reaction, a dissociation occurs separating the sorbent and the sorbate substances, this is an endothermic process. After that, the two components can be stored in an isolated form at ambient temperature and heat is stored with no thermal losses (Storage step) until they can be mixed again and the reverse exothermic reaction of discharge occurs (Discharge step).[9]

The reference reversible reaction is:



A. de Gracia, L.F. Cabeza / Energy and Buildings 103 (2015) 414–419

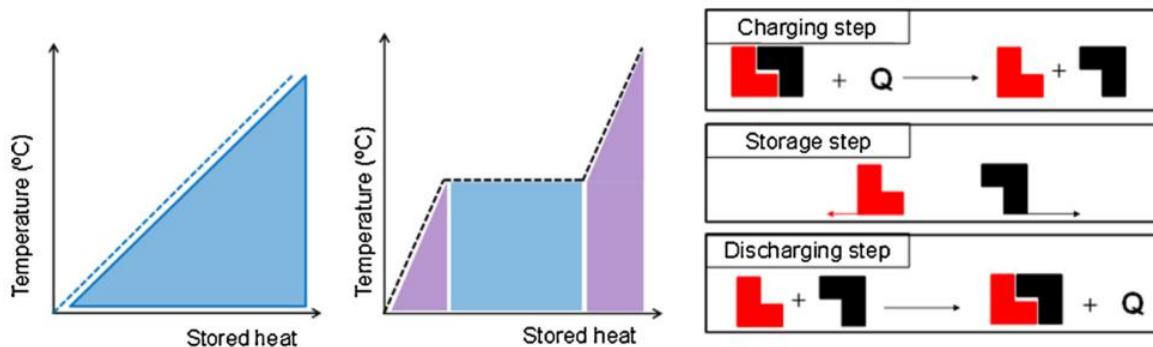


Figure 2 - Thermal Energy Storage principles (de Gracia & Cabeza, 2015)

The choice of a specific technology must correspond to facility/process requirements which it is intended to be integrated with. The definition and distinction of pros and cons guide the selection of such solution according to system design, the size of the thermal power to store, the storing time (whether it's a long or short-term energy storage) or according to compatibility issues of the materials that may come out between the storage materials, the containment materials and the transfer medium whether in direct contact. [10]

In order to start the plan for the realization of a technology, the most important step to undertake to meet these requirements is tightly bind to the selection of the storage material in the first place. Along with the main features of a storage technology, one must direct its research of the optimal material according to the specific application and over its operational time.

It is clearly impossible to choose the perfect storage material with the best performance, the selection must be a an optimum amongst all the thermo-physical properties and performance of the materials, especially for a given admissible temperature range of the material before the latter degrades.

Several are the criteria for preferring a technology amongst the others, several software have also been created lately to help decision makers to make a reasonable choice according to their system requirements.

Table 1 – Summary of the main advantages and disadvantages of Thermal Energy Storage (TES) technologies.

Sensible Heat (STES)	Latent Heat (LHTES)	Thermochemical Heat (TCES)
Days/seasonal storage	Hours/seasonal storage	Hours/days storage
Advantages:	Advantages:	Advantages:
<ul style="list-style-type: none"> <li>- Cheap materials (except for thermal oils);</li> <li>- Widely commercialized;</li> <li>- Non-toxic materials;</li> <li>- Easier system design;</li> <li>- Thermally stable at high temperatures;</li> </ul>	<ul style="list-style-type: none"> <li>- Wide range of costs;</li> <li>- Lower volumes and higher energy densities;</li> <li>- Low thermal conductivity (except for metals);</li> <li>- Low specific heat;</li> <li>- Commercialized only for some temperature and materials;</li> </ul>	<ul style="list-style-type: none"> <li>- Lowest volumes and highest densities (compactness);</li> <li>- Low heat losses;</li> <li>- Long-term storage;</li> </ul>
Disadvantages:	Disadvantages:	Disadvantages:
<ul style="list-style-type: none"> <li>- High volumes;</li> <li>- Higher energy losses;</li> <li>- Higher costs of containment materials;</li> </ul>	<ul style="list-style-type: none"> <li>- Leakage issues;</li> <li>- Thermal and chemical stability;</li> <li>- Subcooling/segregation of some PCMs</li> <li>- Flammability of paraffins</li> </ul>	<ul style="list-style-type: none"> <li>- Possible degradation and corrosion of some materials;</li> <li>- Complex design;</li> <li>- High investment costs;</li> <li>- Research stage;</li> </ul>

## 2.2 Phase Change Materials (PCM) for Latent Heat Thermal Energy Storage (LHTES)

The main goal of this sub-section is to provide a more detailed description on the underlying principle of the PCMs as a starting point to introduce in Section 2.2. where Form-Stable Materials are introduced.

Latent Heat is the amount of enthalpy which is necessary to provide or withdrawn from a system allowing a phase transition of it, substances or composite materials exploiting this source of heat, acting both as a sink and as a source in the reverse process, are the termed Phase Change Materials or PCMs. During a phase transition, a thermodynamic system absorbs and releases a fixed and constant amount of energy, similarly PCMs undergo a reversible process of storing and releasing heat when required during a certain number of cycles depending on the lifetime of the materials involved. PCMs work indeed in a subsequent series of endothermic and exothermic reactions, a complete PCM cycle includes two phases:

- Charging: endothermic process including both the contribution of sensible heat and latent heat leading to the melting phase from solid to liquid (Figure 3).
- Discharging: the process is followed backwards, it is an exothermic one;

A complete charging or discharging process however, does not occur instantaneously and it involves a certain temperature drop. The intermediate melting and freezing phases occur with almost no temperature differences compared to the sensible phases when the energy

stored or released backwards are prevalently performed by the temperature increase/decrease from/to an external source of heat.

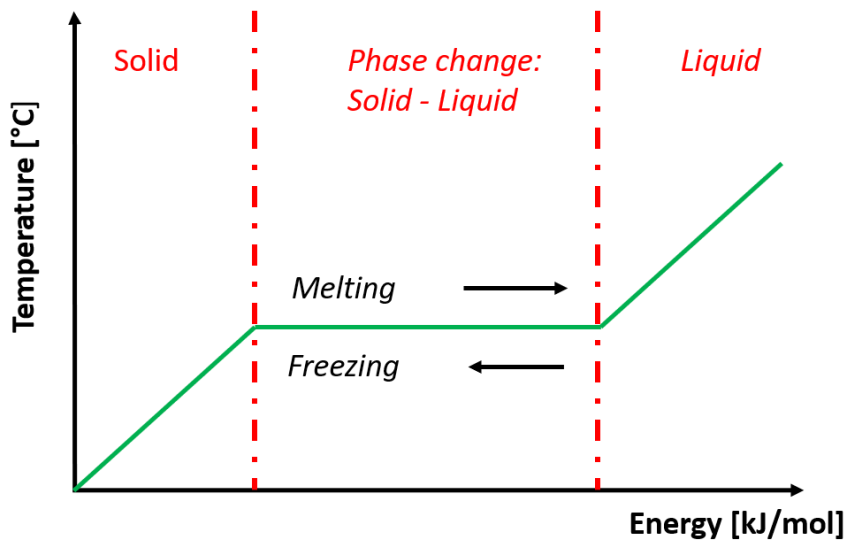


Figure 3 - Phase Change plot for Solid to Liquid phase. It shows the thermal energy to provide/withdraw to/from the system to cause a phase transition.

In particular, during melting, both liquid and solid phases exist and all the energy supplied is not employed to cause an additional temperature increase but to break the chemical bonds between the particles to allow the complete phase change of the substance from solid into the liquid state.

Latent heat has the main feature of having considerably higher values compared to sensible fractions for usual temperature changes. As a consequence, storage systems applying PCMs are able to store a larger amount of heat in the same volumes and operating temperature ranges. Equations show that contributions to the latent heat are the two sensible fractions operating the sensible temperature increase and the latent fraction stored/released at nearly constant melting temperature  $T_m$ .

$$Q_{Sensible} = m * \int_{T_{LOW}}^{T_{HIGH}} c_p(T) * dT$$

$$Q_{Latent} = m * \int_{T_{LOW}}^{T_m} c_p(T) * dT + m * \Delta H_{LAT} + m * \int_{T_m}^{T_{HIGH}} c_p(T) * dT$$

Generally, the phase change of interest for practical applications is the solid-liquid transition which leads, even with lower energy densities, to negligible or controllable volume variations. Several are the criteria for classification of PCMs, the one hereby proposed in Figure 4 is organized according to the materials' chemical nature and to their thermo-physical properties, thus applications, the ones showed refer to the solid-to-liquid PCM category.

According to Figure 4, they can be divided into three main categories and described below.

- Organic;
- Inorganic;
- Eutectic mixtures;

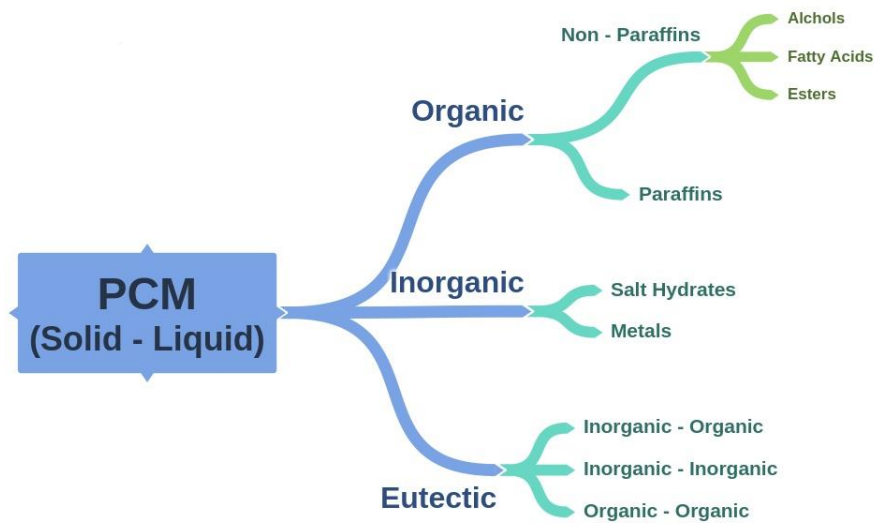


Figure 4 – PCM Basic classification according to the chemical nature of their components.

Organic materials including paraffins and non-paraffins are the most widely used and commercialized PCMs especially for domestic applications. Paraffins materials in particular, have a melting temperature between -18 to around 30°C (in the range of human comfort temperature), non-corrosivity, non-toxicity, good chemical stability so that they are preferably used for space heating/cooling buildings applications. Because of their large availability in the market they are also cheap compared to other types of PCMs. Some specific kinds of paraffin waxes with a different or higher carbon composition allow to gain higher latent heat and melting temperatures expanding the window for the application of such materials. The same happens for fatty acids in the subcategory of the non-paraffins PCM, the latter however undergo a sharper phase change compared to others occurring at higher temperatures. Common drawbacks of organic PCM in general include their very poor thermal conductivity but more specifically, the main limitations about using paraffins are related with flammability and non-negligible volume change (around 10%) on the other hand non-paraffins are corrosive, highly flammable and toxic. Non paraffins however do not experience phase segregation or subcooling and are generally chemically stable. Amongst Non-paraffins sugar alcohols present the highest melting temperatures and latent heats at lower prices but with high chemical instability which leads to more attention to be paid in the design phase.

Inorganics counting molten salts, salt hydrates and metals, have generally highest melting temperatures and latent heat, one of the most important benefit is the high thermal conductivity. These materials however experience a lot of disadvantages connected mainly with the use of salt hydrates specifically. The latter show phase segregation and supercooling issues, corrosion when in contact with metal containers and high thermal instability. On the other side, metals reach the highest thermal conductivity but with low latent heat and low specific heat and, in addition to this, they are also very expensive.

Eutectics are binary or multiple mixtures of organic-organic, inorganic-inorganic or organic-inorganic materials. In general, they do not experience phase segregation issues, present good thermal conductivity and have higher melting temperatures. Even if some researchers claim that thermal properties for eutectic mixtures can be evaluated with some accuracy, salt eutectics for example have specific thermo-physical properties changing compared to the single pure salts composing them, so that they should be experimentally determined. For this reason eutectics represent an alternative PCM because the eutectic composition formation allows to change the thermo-physical properties of the pure salts according to the needed application.[10,11]

Despite the category a PCM belongs to, generally it must meet some technical requirements in order to be adopted for a LHTES system and the choice is totally application-driven. The criteria for the selection of a good PCM include thermodynamic, kinetic and other costs and safety-related requirements.

***Thermodynamic requirements:***

- Melting point in the operating temperature range of the source of heat;
- High enthalpy of fusion;
- High specific heat (to possibly exploit also the sensible heat contribution);
- High thermal conductivity for heat transfer enhancement;
- Congruent phase change (complete and homogeneous solid-liquid phases without segregation issues);
- No irreversible changes of the thermal properties after fusion (thermal stability);
- Small volume changes during phase transition for design issues;
- Cyclic stability (no phase separation issues);

***Kinetic requirements:***

- No or minor supercooling, this is possible when nucleating velocities and crystal grows are sufficiently high. In some cases, this delay of the phase change process even after reaching the melting point is inevitable, common solutions include adding nucleating or thickening agents inside the PCMs. Alternative solutions are related with the adoption of ultrasounds which improve the diffusion of ions, leading to the formation of nucleating cavities and breaking the crystals speeding up melting process.

***Costs & Safety-related requirements:***

- Chemical stability;
- Compatibility with other materials;
- No toxicity of the substance;
- Low flammability;
- Compactness (related with heat capacity:  $\rho \cdot c_p$  [kJ/m<sup>3</sup>°C]);
- Wide availability in the market;
- Low or limited costs;
- Possibility to be easily disposed out;

Generally, in the Thermal Energy Storage sector it doesn't exist a PCM fulfilling all the requirements for a LHTES, so that an optimum must be found between the basic requirements for the selection of a good PCM and the properties characterizing all the PCMs commercialized in the market.

Because of the occurring of the Liquid phase PCMs have commonly been contained inside different configurations of tank-like devices where direct contact with a Heat Transfer Fluid (HTF) is physically avoided and no chemical compatibility issues arise. The layouts widely commercialized and applied for TES applications are cylindrical models, slab containers and shell-and-tube which is the most wide-spread commercially. [12] A summary of the three schemes reviewed is shown in Figure 5.

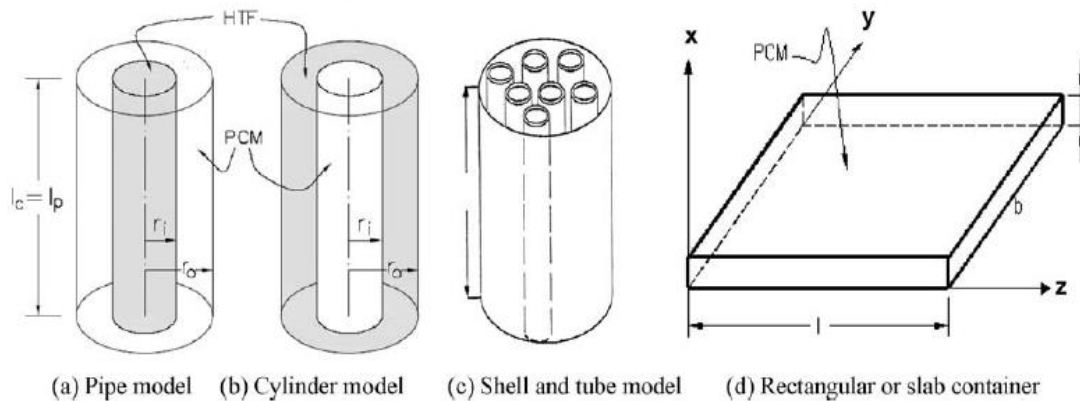


Figure 5 - Containment systems layouts options (F. Agyenim, 2010).

The cylindrical models offer also alternatives on how to circulate the HTF with respect to the PCM material, whether in the inner or the outer tube. In such layouts the heat transfer occurs throughout the wall surfaces separating the PCM from the HTF flow which can flow both in parallel or in counter-current.

### 2.3 Form-Stable solutions for PCMs

As specified in Section 2.1, some of the main issues related to the inclusion of the PCM materials inside devices regards leakage and chemical compatibility when in contact with other containment materials or with the flowing HTF. In addition to these, the need to investigate new containment solutions for industrial purposes that might allow the reduction of materials and consequently the reduction of the costs, has led to finding innovative solutions including encapsulation technologies, whether macro-encapsulation or micro-encapsulation, impregnation methods inside construction materials or shape-stabilized PCMs. These studies have been decisive for the spreading of PCM-based solutions for the domestic/building sector and each of them have proved to be advantageous from the sole holding and physical-separation point of view but on the other hand, while being tested and commercialized, some of them showed some drawbacks.[11]

As a consequence, in the past years, researchers have paid great attention on developing in a more effective and reliable way the aforementioned new containment solutions at different scales. As shown in Figure 6, **Macroencapsulated-PCMs** examples are: encapsulation in plastic bags (Dörken) for salt hydrates and some organics, capsule stripes (PCP and Dörken) for large surface heating, metal containers to be included inside construction bricks,

spherical capsules for packed-bed systems. These solutions are already widely commercialized both in the industrial and domestic sector.

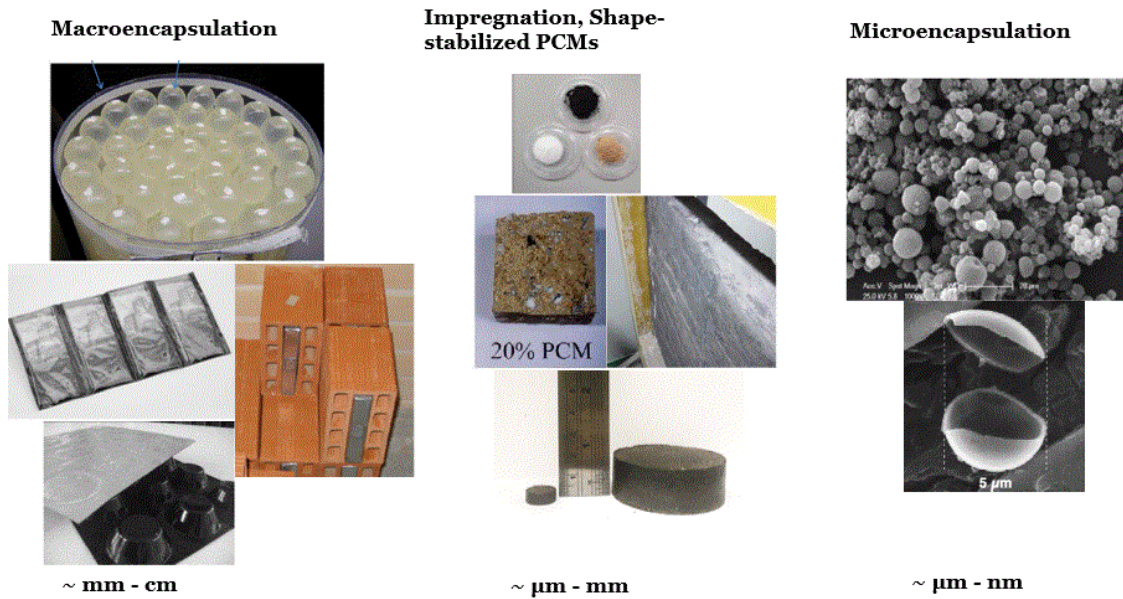


Figure 6 – Currently developed containment solutions for PCMs. Reference pictures from [13][15][91][92]

The size of the macroencapsulated-PCMs range between some mm of diameter of the spherical shells (the choice of the material of the surrounding shells is dependent on the chemical properties of the PCM) to some cm of the metallic containers.

**Microencapsulated-PCMs (MEPCM)** consist on encapsulated PCM particles in solid shells in the range  $1 \mu\text{m} - 1000 \mu\text{m}$  which can be used in powder form or transported inside an HTF. As widely reviewed by Jamekhorshid et al's, MEPCMs can be produced by different methods ranging from physical, physic-chemical and chemical techniques. The most common ones include coating, spray drying, coacervation and different kinds of polymerization. [13] MEPCM is an alternative solution to prevent the PCM's reactivity towards the surrounding materials, allowing higher surface to volume ratios thus enhancing significantly the heat transfer. One of the most important reasons to address the attention towards this relatively new solution is because microencapsulation solves phase separation issues arising when dealing with specific PCMs like salt hydrates. [14] Additional and more common disadvantages accounts for long-term instability due to circulation during pumping and the presence of supercooling, reason why the MEPCMs commercialized are only those non soluble in water, the most commonly PCM used are indeed organic PCMs [15]. Lately, Nanoencapsulated-PCMs (NEPCMs) with nano-scale capsules to be carried by a liquid flow are being investigated because smaller deformations over time have been experimentally observed. NEPCMs and MEPCMs combined with carbon-based structures greatly enhance heat transfer[16]. Another benefit derives from the non-agglomeration issues of the NEPCMs in the HTF compared to the microcapsules of the MEPCMs.

Both kinds of encapsulating methods, along with the choice of appropriate containment materials/techniques according to the PCM properties, ensure chemical and thermal stability

because of the mechanical separation of the PCMs. A summary of the main features characterizing these methods are listed in Table.

As shown in Figure 6, **Form-Stable PCMs (FPCMs)** is another alternative being investigated by researchers to cope with containment solutions thus ensuring a cost-effective and simpler manufacturing procedure.

## *2.4 Form-Stable Phase Change Materials (FPCMs)*

Form-Stable or also called Shape-Stable PCMs (SSPCMs) are composite materials where the key PCM component is combined or embedded inside another material in a mechanically stable structure. A composite material usually shows modified thermo-physical properties compared to the single components constituting it, so that the characterization and the underlying understanding of the behaviour of such materials can be a rather complex and unpredictable issue. To make sure the properties of the composite as a whole are maintained, the structures/particles added should be in sub-millimetre range. This would guarantee that the properties as size and shape-independent as possible.

The key components constituting a typical SSPCMs imply a PCM and a supporting material (SM). In addition to these, according to the thermo-physical properties of the previous materials involved, a thermal enhancement material may be added. As described by Mehling H et al's, components of composites can range from fibres and particles carried directly inside the PCM otherwise an embedding matrix supporting the PCM itself, a representative illustration is shown in Figure 7.

**Supporting or Structuring material (SM):** In a SSPCM composite a skeleton material (also called support matrix) hosts the PCM material holding it throughout the solid state to its transition to the liquid form, similarly to what is shown in Figure 7-(b). The SM allows to achieve all the benefits of the encapsulation related with separation from other materials but reducing its contact resistance. Usually the SM accommodate volume changes of the PCM and it should prevent it from dispersing out from the matrix.

**Thermal enhancement material:** This component is becoming more and more common when dealing with FPCMs in order to cope with one of the main restrictions of adopting PCMs for industrial applications which require frequent and short-term charge and discharge time. Thermal performance enhancement is fundamental due to PCMs' well-known low thermal conductivity (except for metallic PCMs) and it is acquired by dispersing highly conductive particles (e.g. graphite, nanoparticles, nanotubes, nanofibers) inside the whole structure of structuring material plus PCM. This concept is illustrated in Figure 7-(a). Many have tried to include both the supporting and thermal enhancement properties by adopting metals [17,18] [19], graphite foams [20] and other solutions [21][22].

As illustrated in Figure 7-(c), the FPCM idea experienced by this study can be considered a combined solution adopting both the idea of a supporting matrix composed of both pores and channels able to host the PCM and an enhancing material dispersed throughout the composite (represented by the red dots). The extent of the pores/channels of the matrix derive directly from the method and the materials of the supporting material.

The Shape-Stability concept is however still widely debated because of the non-completely controllable cross-linked thermo-physical e micro-structural behaviour of the materials in close contact with each other. Shape-stability concept is thought to be primarily a consequence of the balance between capillary forces of the PCM flowing in the liquid state inside the matrix and the high surface energy of the SM which holds the PCM particles. The probability of the PCM of being leaked from the overall structure is indeed connected to the counterbalance of these forces and on structural features that need to be investigated case by case according to the materials and the fabrication method chosen.

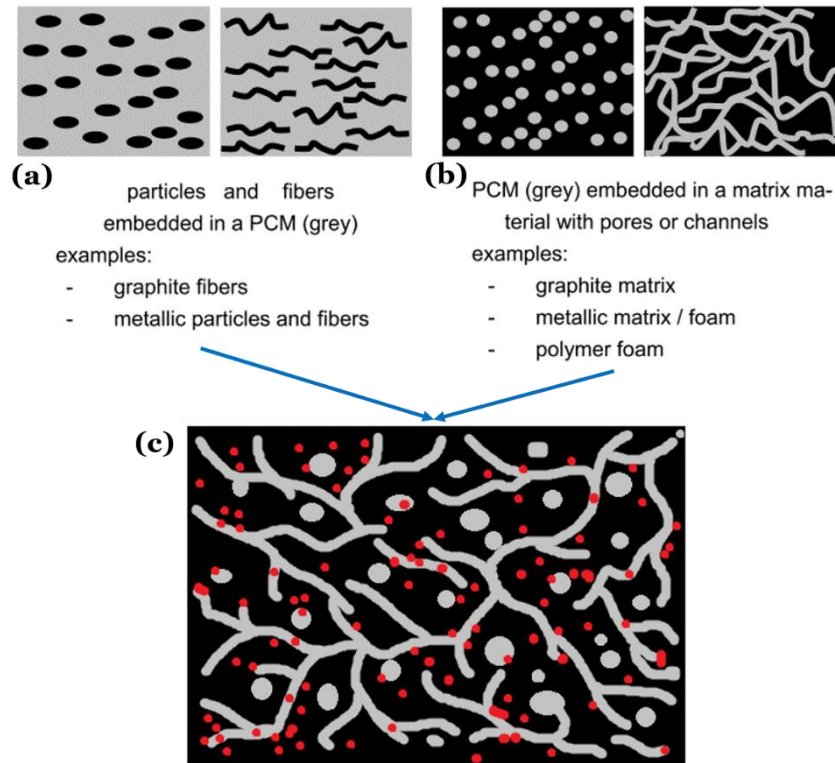


Figure 7 - Possible composites configuration (a) with particles dispersed and carried by the PCM, (b) with PCM infused in a host matrix made of pores or channels (Ref. [15]). (c) Illustrative concept of a composite of FPCM with a host matrix and red particles dispersed.

As mentioned in Section 2.2, SSPCM option is proving a valuable solution for challenge of encapsulating the liquid PCMs and solve long-term shape stability over cycles with controllable volume variations. These challenges have been addressed to solve some of the main scientific blocks of practically apply and commercializing PCMs. One of the main issues connected to the realization of this novel PCM technology is related with the higher energy densities [kJ/kg] compared to sensible storage solutions because the supporting material's higher specific heat allows to exploit in a reasonable way also the sensible heat fraction when heating up to the melting point and above. SSPCMs composites should then be characterized in the most extended possible way because all the thermo-physical properties are temperature-dependent and because when dealing with composites, according to their fabrication methods, those properties are less predictable.

An overview on the types of containing-PCMs solutions discussed above and in Section 2.2 is provided in Table 2 with a summary of the main features which provide a broad view of

the current stage of development of each technology. As detailed in Table 2, FPCM have clearly introduced some advantages compared to their precursors Macroencapsulated-PCMs and, at this stage it may compete with MEPCMs if a straightforward explanation of the Shape-Stability concept is being found.

Even though FPCMs are still at a prototype and lab research level, once reached a mastery control of the most reliable and affordable procedure to produce them, this solution may drive stakeholder's investing plans. In the Leakage section it's indeed stated that the manufacturing strongly dictates the probability for the PCM to be released from the host matrix. Impregnation or infiltration techniques in a pre-fabricated matrix guarantee the formation of a reinforced overall structure, while other compressing techniques employing materials in the powder form strictly depends on other external parameters (e.g. the nature or impurities of the SM, the compressing pressure, the particle size).

Table 2 - Containment options for PCMs summary.

	<b>Macro-Encapsulated PCM</b>	<b>Micro-Encapsulated PCM</b>	<b>Form-Stable PCM</b>
<b>Status</b>	Mature level	Further research needed on some techniques against leakage issues	Ongoing research
<b>Development sector</b>	Industrial/domestic sectors commercialization	Lab research, Industrial sector	Lab research, prototype level
<b>Cost</b>	High cost	Wide range of prices depending onto the microencapsulation technique	Low cost
<b>Supercooling</b>	Yes	No	Not demonstrated
<b>Phase separation</b>	Yes	Only for Salt Hydrated-PCMs	No
<b>Deformation</b>	Yes (in the long-term and for some types only)	No	Controllable volume variations
<b>Leakage</b>	Yes (in the long-term and for some types only)	Yes, at micro-scale (avoided with NEPCMs)	Yes (depending on the SM and on the manufacturing)
<b>Agglomeration</b>	No	Yes	Possible (depending on the manufacturing)
<b>Heat transfer enhancement</b>	Higher only with metal shells or finned-metal/conductive plates	High (further enhanced when combined with nanofluids or NEPCMs)	High (further enhanced when combined with carbon-based nanostructures)

At the current stage several researcher groups working on TES solutions are investigating on FPCMs' characterization trying to increase their knowledge on which manufacturing procedure is more suitable for each specific formulation as well as about how to refine the methods used.

The literature review on the state-of-the-art on FPCMS showed that the most commonly used methods for producing SSPCMs are:

- Vacuum impregnation (or absorption, infiltration) mainly for organic PCMs but also tried on some acids [23–35];
- Mixing & Cold compression (generally for powder form-PCMs) [22,36–38];
- Hot compression;
- Direct impregnation [39];
- Mixing and stirring of mixtures;

Collective reviews on some of the materials considered have been provided by Peizhao et al's, with a comprehensive description on preparation, characterization and application of clay-based mineral materials with high absorbability including kaolin, diatomite, sepiolite, montmorillonite, perlite, SiO<sub>2</sub>, attapulgite, vermiculite and fly ash. [40]

The choice of the technique to adopt is not exempt from some technological constraints related with the employment of specific materials. For instance, acid mixtures of PCMs are more prone to be impregnated, infiltrated or absorbed into a SM, powder-like materials on the other hand are more likely to be compressed. For this reason and according to the system application requirements, the selection of the materials involved is considered the first necessary step for the development of such technologies to overcome the prototype status and enter the market.

## 2.5 *Form-Stable PCMs Screening Maps*

Principle dictating the selection of the materials for FPCMs include as a first criteria, their chemical stability of the skeleton materials above the melting point of the PCM to avoid any decomposition, good wettability toward the liquid PCM to avoid leakage and good dispersibility of the thermal enhancement particles into the liquid PCM. Meeting all the selection criteria is a straightforward task as different class of PCMs (e.g. organic, inorganic, salt hydrates, etc) necessitate specialized skeleton and enhancing materials. As a result, a few FSPCM formulations have been proposed in the literature and mainly only with organic PCMs.

A literature review of around 50 peer-reviewed publications has been considered to build a sufficiently representative collection of FPCMs. Articles have been searched in Scopus and Science Direct as well as other Science databases by means of the keywords shape-stable PCM, form-stable PCM, composite PCM, phase change materials and thermal energy storage between 2012 and 2018.

The performance indicators extrapolated which are useful to set up a database of FPCMs are latent heat and melting point, thermal conductivity, thermal and structural stability over test cycles. All the FPCM have then been grouped into categories according to the nature of supporting material adopted in the formulations. Screening maps (shown in Figures 8-9) as a result of properties gathered from this database have been built to visually place from a

performance as well as an economical point of view the various supporting material-based formulations. The final purpose from this screening procedure is to drive the selection of the formulation to be assessed as a suitable FPCM to apply for the reference LHTES.

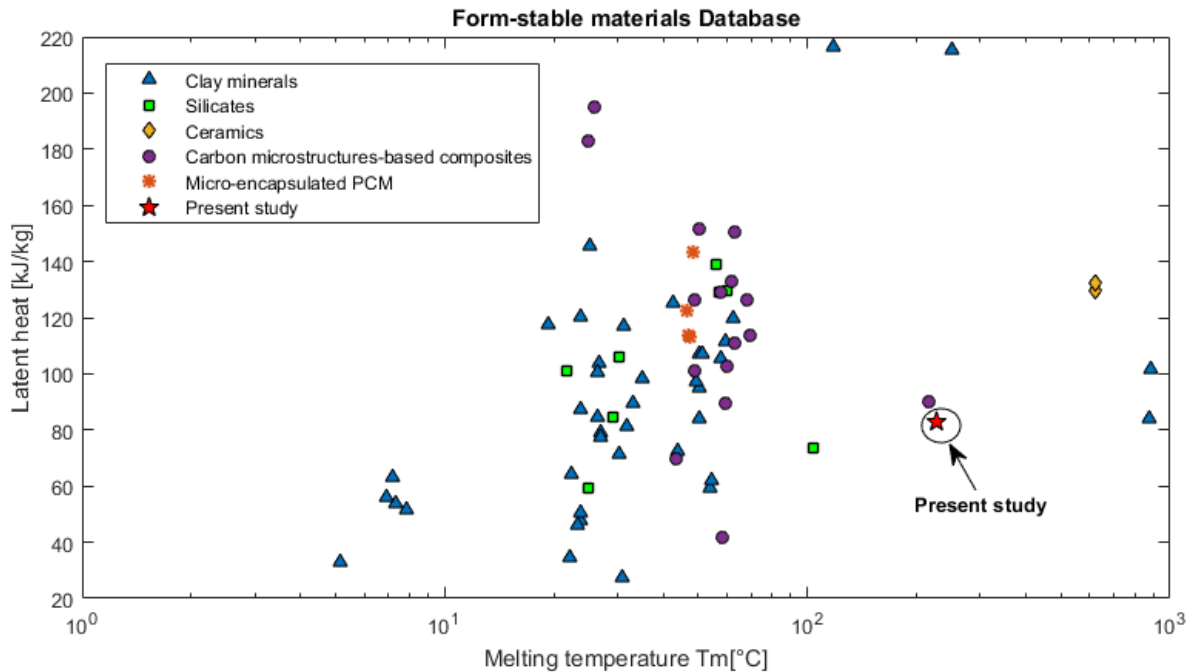


Figure 8 - Screening map based onto FPCMs state-of-the-art from 2012-2018.

It emerges clearly that studies on SSPCMs mostly have focused on materials with melting temperature in the range 20- 70°C – a clear indicator of SSPCM using organic materials (paraffins, fatty acids etc) as PCMs. Higher temperature SSPCMs are far less investigated [41][38][42].

The Solar salt which has been selected as PCM is a eutectic of  $\text{NaNO}_3$  and  $\text{KNO}_3$ , supported by Vermiculite and graphite as thermal performance enhancer. From a chemical point of view Vermiculite and Graphite show no chemical decomposition in this temperature range, additionally they do not cause fire or explosion hazard and they are non-toxic, so that they can be easily handled safely and applied for a wide variety of applications.

The adoption of the vermiculite ensures the overall shape-stability of the composites. It has been selected because of its high surface area due to its highly-porous structure, and high absorbability. Benefits, like other ceramic materials account for high specific heat coefficient allowing to exploit the sensible heat fraction whereas, on the other hand it shows low thermal conductivity.

Furthermore, most of the studies addresses how to formulate SSPCM, but it emerged that there is a lack of understanding of the SSPCM microstructure and especially a lack of experimentally-derived properties to build a complete characterization and comparison of the formulations.

The same lack of data is connected with the prices associated to the SSPCMs which have been estimated by peer-reviewed articles where available or open web-sources.

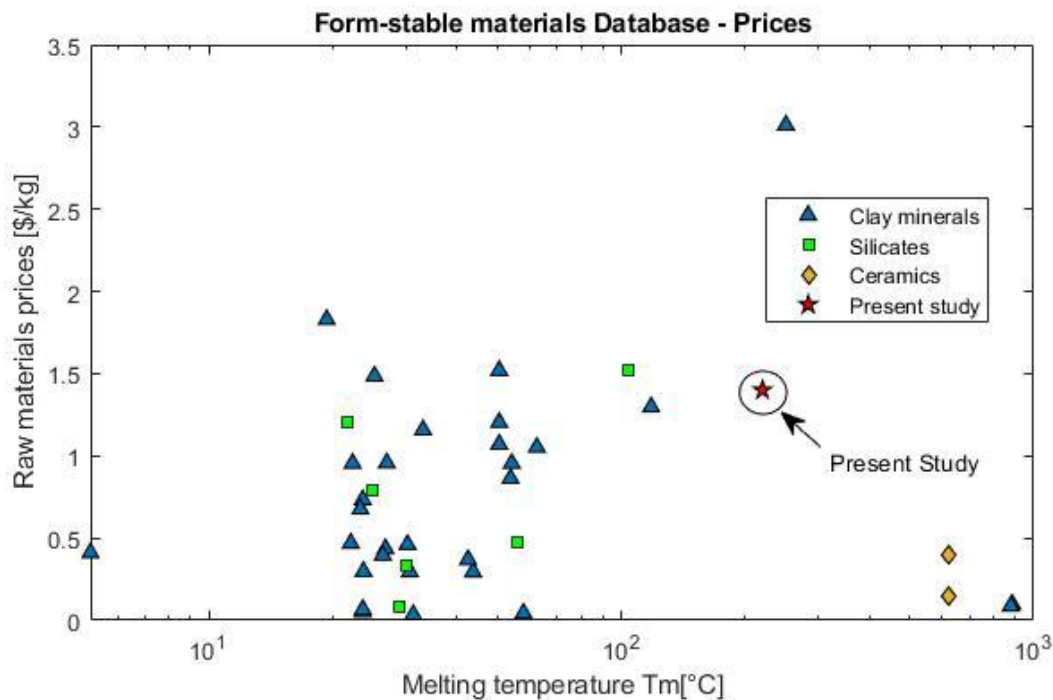


Figure 9 - Screening map on prices on materials forming FPCMs collected on web databases.

### 3 Experimental methods

In order to increase the knowledge on SSPCMs along with providing an extended experimental characterization of materials, the number of techniques proposed for this study is an attempt for filling the gaps in literature on the topic of form-stability. A summary of the experimental methods adopted for the characterization of the proposed formulations of SSPCMs is shown in Figure 10 and provides a guideline for all the experimental methods and results outlined in both Sections 3 and 4.

**Helium Pycnometer (HP) and Calibre measurements.** AccuPyc III plus was used for effective actual density measurements while Calibre was used to obtain bulk density measurements.

**Dilatometry Analysis (DIL).** Optical Dilatometer SDT Q600 V5.0 Build 63 has been used to evaluate thermal expansion coefficient  $\alpha_v$  [1/°C] and change in length  $\Delta L$  in the micro and sub-micro scale as a volume expansion parameter.

**Scanning electron microscopy (SEM) and Energy dispersive X-ray spectroscopy (EDX).** Hitachi TM3030 microscope equipped with energy dispersive X-ray spectroscopy (EDX) was used;

**Differential Scanning calorimetry (DSC).** SSPCM composites were tested by using a differential scanning calorimeter from Mettler-Toledo (DSC2+).

**Laser flash analysis.** The thermal diffusivity  $\alpha$  [mm<sup>2</sup>/s] was measured using a laser flash apparatus (LFA 447 from Netzsch).

**Micro-computed tomography (micro-CT).** 3D non-destructive reconstruction of SSPCM geometry and topology was obtained via micro-CT scans performed using Bruker Skyscan 2211 with an X-ray source in the range 20-190kV and images format up to 4k x 4k x 2k pixels. Quantitative parameters were computed through a combination of CTAN software and in-house Matlab codes.

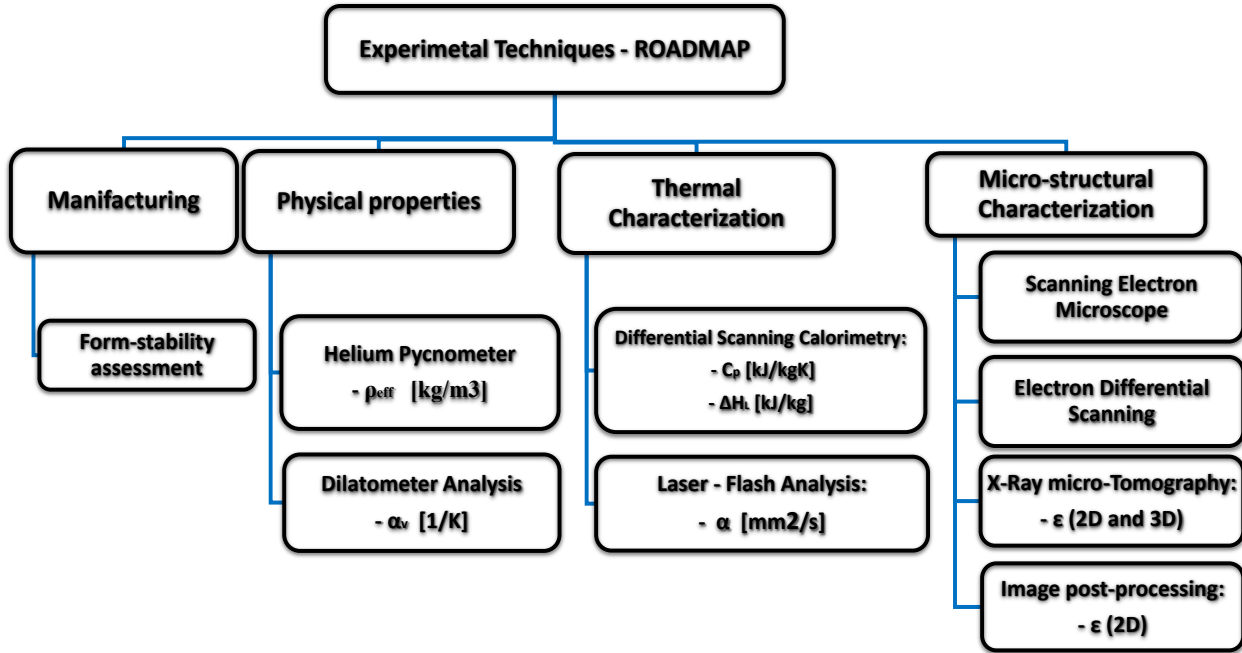


Figure 10 - Experimental procedure - Roadmap

After the selection of the specific formulation of FPCM for the case-study, the following roadmap has been drawn providing an intuitive overview onto the experimental steps that have been undertaken to characterize both from a thermal performance point of view and a structural one on the FPCM formulations analysed. This diagram is also a summary of the resulting thermo-physical quantities that have been collected from each technique. On one hand for some properties like density  $\rho$  [kg/m<sup>3</sup>], thermal diffusivity  $\alpha$  [mm<sup>2</sup>/s] from LFA, latent heat  $\Delta H_L$  [kJ/kg] and specific heat  $c_p$  [kJ/(kg\*°C)] from DSC, numerical results have literally been collected, some others allowed a semi-quantitative or qualitative analysis. The latter is the case of SEM/EDX and the Leaking Test results obtained after the heat treatment during the manufacturing process.

All the results are valuable contributions to validate the reliability of the fabrication process and to support the FPCM as a valuable TES alternative for a macro-scale industrial application. Every technique or equipment adopted has been briefly outlined in Section 3 as for its basic functioning principle while in Section 4 the actual results have been collected and widely discussed.

### 3.1 Differential Scanning Calorimetry (DSC)

This technique is one of the most widely used in the field of materials characterization, it is the main tool when investigating the thermal behaviour of a material or composite. The principle underlying this method is related with the analysis of the heat variation between two samples kept at the same temperature inside a furnace. One sample is called reference sample and it's usually an empty crucible while the other one is a crucible filled with the actual sample material to be tested, both crucibles are placed inside a furnace which is heated up or cooled down according to the program set for the test. Once the temperature program is set, the temperature of the two samples change and their temperature variation is detected by a sensor which is in direct contact and connected to a thermocouple. When heated for instance, the empty reference pan heats up faster than the sample pan, so that a temperature difference is registered. As shown in Figure 12, the two output signals proceed parallelly according when a constant heating rate [ $^{\circ}\text{C}/\text{min}$ ] is set until at a certain time  $t_1$  the sample goes through a reaction experiencing a temperature variation. According to the duration of the occurring reaction, the signal may show peaks according to the kind of phenomenon occurring. When a phase transition happens, a difference of enthalpy occurs between the pans providing information of the enthalpy of transition, the latent heat.

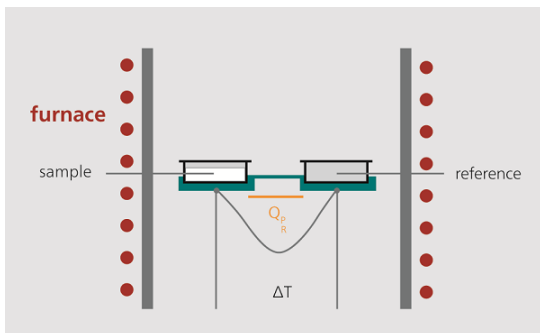


Figure 12 - Basic principle of DSC functioning (Ref. NETZSCH open web-source).

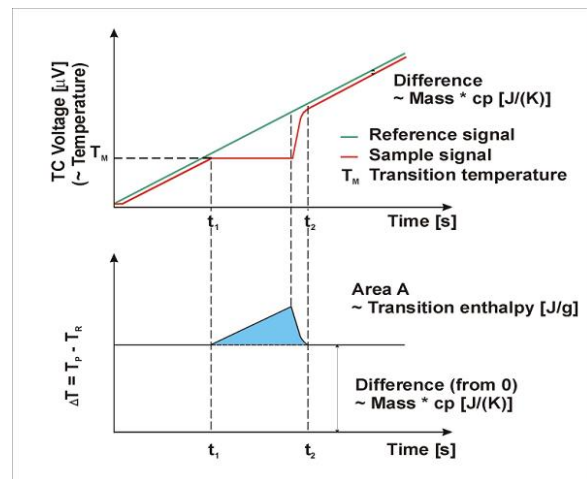


Figure 11 - Signal variation detected by DSC when a reaction occurs. (Ref. NETZSCH open web-source)

In order to obtain accurate and reliable results the choice of the same crucible between the sample and the reference is fundamental. Different materials and capacity are available, an example is shown in Figure 15, where a Pt 30  $\mu\text{l}$  is depicted while on Figure 13 two 40  $\mu\text{l}$  Al crucibles are placed inside the furnace. Choosing the right crucible is also important to avoid unwanted reactions with the materials tested and to obtain a sharp and well-defined signal.



Figure 14 - Furnace detail of DSC.



Figure 13 - Pt crucible.

The equipment adopted for this analysis is the Mettler-Toledo (DSC2+). The preparation included mixing of the powder-like components of the composites under investigation and placed inside a Pt crucible and weighted them. Each test has been run 3-4 times and also the pure components have been tested to check compatibility with literature reported values and to guarantee the reliability of the composites results.

### 3.2 Laser Flash Apparatus (LFA)

Laser Flash Analysis is an important method to acquire a more complete thermal characterization of the thermal properties of materials. In general, thermal diffusivity, as well as other thermo-physical properties, cannot be calculated mathematically especially in the case of composite materials because they are highly temperature-dependent. Despite their known formulation, some thermal properties of composites do not change proportionally to their composition, as a consequence the evaluation of such quantities is a fundamental step to foresee the behaviour of the material over temperature in a device-scale perspective.

The final task of this analysis is the evaluation of the thermal conductivity, which depends on material density, thermal diffusivity and specific heat, Laser Flash Apparatus provides only their thermal diffusivity of the sample.

The equipment considered for this analysis is the Laser Flash Apparatus (LFA) 447 from Netzsch. This method is particularly efficient when dealing with low-thickness solid samples and its functioning principle recalls studies conducted by Parker et al's in 1961. Different methods have been developed until that by means of solving transient or steady-state equations however, these methods proved to be ineffective at higher temperatures [43], thus the necessity to find an alternative and more reliable technology applicable in a wider temperature range.

When placed on the top carrier inside a tube-shaped furnace and safely closed inside, the sample is hit by a laser flash-pulse from its bottom surface to the top layer and it's suddenly heated up. After this first shot, a temperature increase occurs inside the furnace so that the material can be tested over a temperature program characterized by shots at specific pre-set temperatures. A detector placed on the top side of the sample detects the temperature change

over time every time the sample is shot. The main assumptions that allow the application of this method are connected to the homogeneity of the density of the material, homogeneity of the shot energy onto the sample and the laser pulse must be of high intensity and short duration. The more the conditions of the specimen are far from these main assumptions, the higher the probability of having higher inaccurate results.

The low-thickness of the sample is meant (generally between 1-2 mm) is necessary for the assumption of one-dimensional heat transfer and the system must be adiabatic towards the environment. Additionally, the sample must not be transparent (reflecting visible light) and it must have a good absorption rate of the heat pulse.

A typical signal obtained from the measurements is shown in Figure 16-(b), where the increase of the signal reflects an increase in the thermal diffusivity of the sample. The measurement is given by the result of the mathematical equation, valid only for adiabatic conditions.

$$a = 0.1388 * \frac{\text{thickness}^2}{t^{0.5}}$$

Where  $a$  is the thermal diffusivity,  $t^{0.5}$  is the time at half of the signal height and the thickness refers to the width of the specimen considered.

The calculation of the thermal conductivity  $\lambda$  [W/(mK)] is a result of Equation:

$$\lambda(T) = a(T) * c_p(T) * \rho(T)$$

Where  $\rho$  is the density,  $c_p$  the specific heat capacity,  $a$  as the thermal diffusivity.

LFA allows, by means of comparing with another well-known material signal, to calculate also the specific heat ( $c_p$ ) of sample. This can be determined using the approximation of the signal height  $\Delta T_{\max}$  compared to the signal height of a reference material.

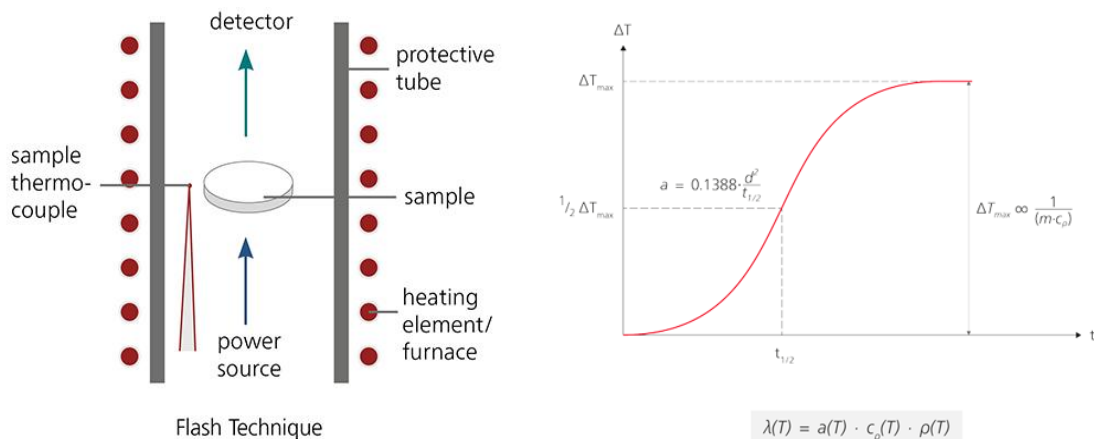


Figure 15 - LFA functioning scheme (left), example of resulting signal (right) collected from NETZSCH website.

These properties have been evaluated by the implementation of calculations model and also a pulse correction. The application of a method is connected to the materials of the samples and the maximum temperature reached. For instance, at higher temperatures and longer shot times, a non-

purely conductive model must be selected. In this specific case-study the Cowan model has been applied to check the response of the manufactured tablets.

### 3.3 Helium Pycnometer (HP)

The instrument used for testing density is the AccuPyc II 1340 Pycnometer.

Helium (or gas) pycnometer is a laboratory machine able to measure the volume of both solid irregular or regular shaped objects with or without internal porous structure. When the mass of the sample is given as input, the equipment provides the effective density measurement. The basic functioning principle is based on gas displacement principle and Boyle's law of gases applied on a two calibrated chambers system connected by a valve as shown in Figure 16.

$V_{CELL}$  and  $V_{EXP}$  are initially at ambient pressure  $P_a$  and ambient temperature  $T_a$  while the valve is closed. Inside the Cell Volume ( $V_{CELL}$ ) a sample with a volume  $V_{SAMP}$  is placed and then the Cell Volume is charged to a higher pressure  $P_1$ . The reference balance equation is:

$$P_1 * (V_{CELL} - V_{SAMP}) = n_c * R * T_a$$

When opened the valve the increase of volume at disposal for the expanding gas lowers the pressure to an intermediate value  $P_2$ , so that the balance equation becomes:

$$P_2 * (V_{CELL} - V_{SAMP} + V_{EXP}) = n_c * R * T_a + n_E * R * T_a$$

The final working equation to estimate the volume of the sample is then:

$$V_{SAMP} = V_{CELL} - \frac{V_{EXP}}{\frac{P_1 - P_a}{P_2 - P_a} - 1}$$

$$\rho_{SAMP} = \frac{mass}{V_{SAMP}}$$

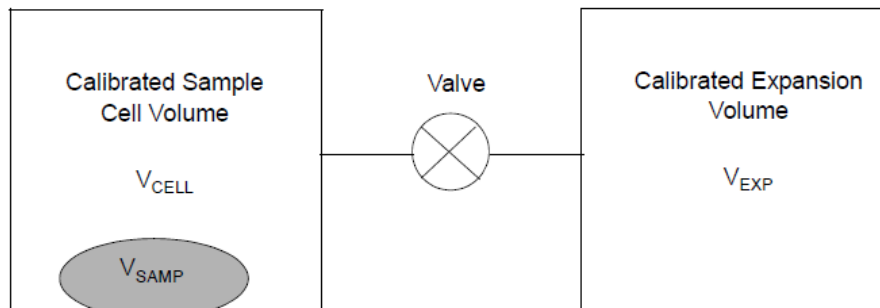


Figure 16 - Helium Pycnometer scheme - AccuPyc User manual.

There are although different measures of density that sometimes may lead to real conceptual mistakes. On one hand there is the bulk (or envelope) density while on the other hand there is the effective (actual, real, apparent or skeletal) density. The one measured by means of the Helium Pycnometer is the effective density and provides an estimation of the actual mass of the sample divided by its volume without accounting for the pore space. This density is the one usually compared with the theoretical density and, for a porous material, it's higher than the bulk one. Bulk density on the other hand, is the measure of density related to the sample's bulk volume taking into account also the volume of the pores. It provides usually an underestimation of the actual volume but it may be useful to evaluate properties like porosity and thermal conductivity of composites.

### 3.4 Dilatometry Analysis

Dilatometer analysis or dilatometry is a method allowing to characterize a material or a composite from a dimensional point of view in function of the temperature and/or time by setting a temperature program the sample has to be tested throughout. The machine used is the Dilatometer SDT Q600 V5.0 Build 63 which can be used both for heating and cooling testing. The equipment is mainly constituted by a furnace where the sample (sizes around some mm) is placed on top of an alumina plate. It is fundamental for the output of the test that the sample is placed into the furnace with a precise parallelism between its two ends and the limits shown onto a display reporting the maximum limits for the specimen displacements. This precaution is necessary to determine automatically the initial length of the specimen and to allow the LED source to emit a planar beam through the available area on the disc furnace where the sample has been placed. The functioning principle described is shown in Figure 17.

Generally, the temperature program must reflect the process one would like to test the composite for, whether is an industrial process or the material's behaviour in its operating setting. In this specific case the composite has been tested in the range 25°C to the materials' degradation temperature around 300°C. The choice of this temperature range is meant to analyse and to provide additional proof along with the density measurements to support the manufacturing procedure, in this specific case precise measurements allow to further investigate onto the sintering process adopted for the fabrication of the FPCM tablets.

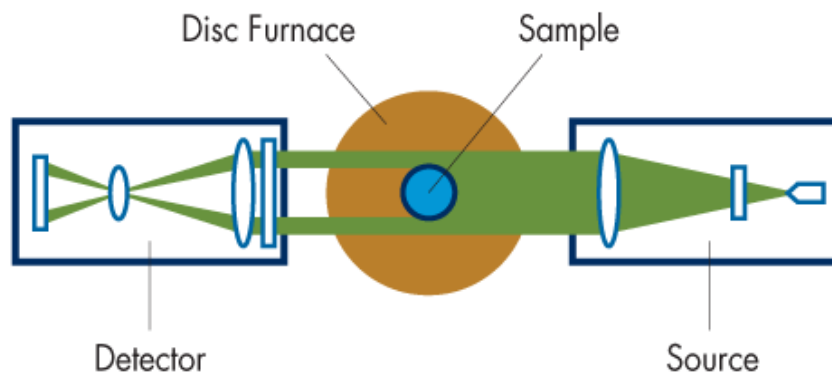


Figure 17 - Optical dilatometer functioning principle. (Ref. TA Instruments open web source)

Main outputs from this technique are the coefficient of thermal expansion  $\alpha_v$ , the change in length of the composite  $\Delta L$  and its percentual change of length. It expresses the degree of volume expansion, thus the volumetric changes occurring inside the composite with respect to an initial size. The thermal expansion coefficient is calculated according to equation:

$$\alpha_v = \frac{1}{L_0} * \left( \frac{\Delta L}{\Delta T} \right)$$

Where  $L_0$  is the starting length measure,  $\Delta T$  the temperature variation experienced during the test and  $\Delta L$  the change in length taking into account the difference between each incremental dimensional change at each time step.

### 3.5 Scanning Electron Microscope (SEM) and Electron Differential Scanning (EDX)

Scanning Electron Microscope is a non-destructive and multi-characterization method providing rapid and high-resolution images resulting from the analysis of the electron beam-solid sample surface interaction. Resolutions acquired are in the range of sub-micronscale with magnifications form 20x to roughly 50,000x (in the nm range) allowing to tackle features beyond the optical microscope resolutions. A summary of the characteristics visible with SEM compared to other microscope techniques is shown in Figure 19 and described by Callister et al's. [44]

Energy Dispersive X-Ray Analyser on the other hand is a complementary technique adopted for elemental identification and semi-quantitative compositional analysis.

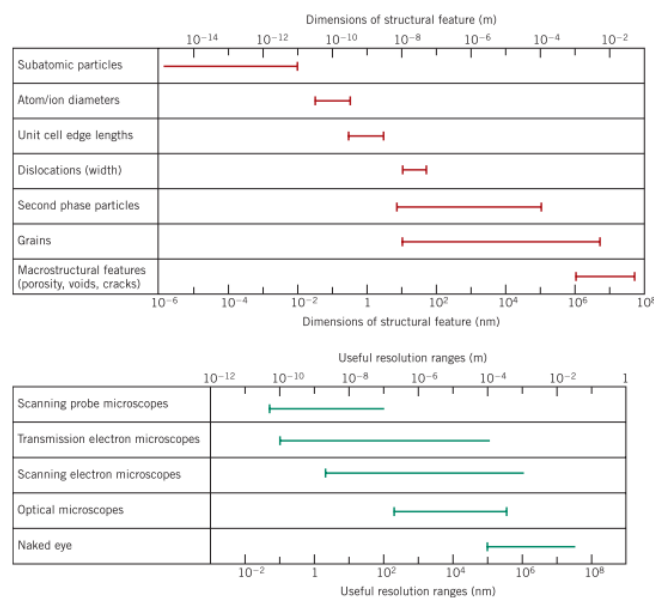


Figure 18 - Summary of features detected by different microscope techniques reviewed in Materials Science and Engineering.

#### Basic functioning principle

The basic functioning principle of a SEM consists on a high-energy electron beam shot by an electron gun which interacts with the atoms of the surface layer of the solid sample, of whom it reveals information about the morphology and topology of its constituting materials.

The resulting signals from the accelerated beam-sample interaction consist on secondary electrons, diffracted backscattered electrons, backscattered electrons, photons, visible light and heat. All of them provide useful, and more or less detailed, insights on the morphological/textural characteristics of a solid and multi-component sample. The most valuable source of signals for the analysis of FPCMs composites are secondary electrons (SE) and backscattered electrons (BSE) which are used to obtain the digital images. Digital images results from special detectors detecting atoms excited from the beam. Specifically, the SE collected are in charge of showing the actual morphology while BSE are those who

track the contrasts of the composition of multiphase specimens. Another additional source of information is provided by the X-ray generated by inelastic electrons collisions in the outer orbitals of atoms of the surface of the sample at a few nm distance. Each excited electron returning its lower energy state yields a characteristic X-ray of a fixed wavelength. Its wavelength value is a result of the difference of the energy levels of different orbitals occupied by the electron from the excited state on his way back to the inner orbitals. Energy Dispersive X-Ray Analysis collects X-rays produced by each element interaction to produce an elemental map to spot chemical composition of the samples. These are just a few of the electron sources which can be collected from electron-sample collisions, others including photons of visible light and Auger electrons are used for other techniques which are beyond of this discussion. Figures 19-20 provide an illustrative explanation of the process of scattering and back-scattering of the electrons.

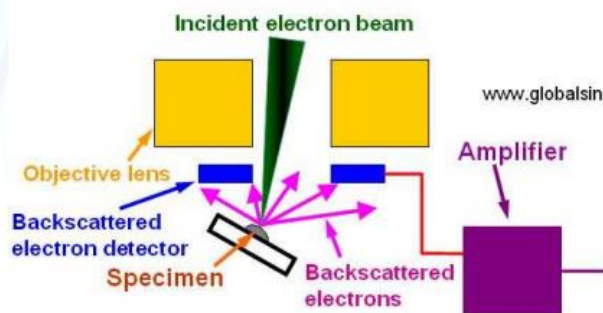


Figure 19 - SEM functioning scheme and components involved. (Ref. [www.globalsino.com/EM/](http://www.globalsino.com/EM/))

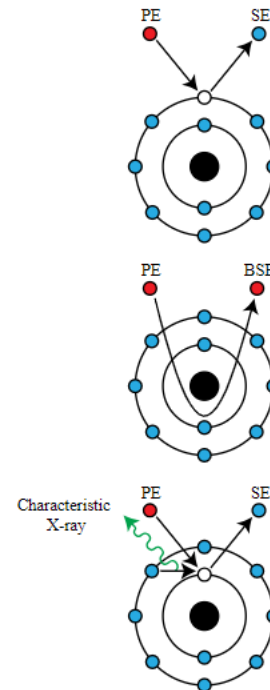


Figure 20 - Electrons mechanisms for SEM/EDX. By Rob Hurt [CC BY-SA 4.0 (<https://creativecommons.org/licenses/by-sa/4.0/>)], from Wikimedia Commons

## Preparation procedure

SEM/EDX Analysis requires minimal preparation for the samples and it depends on the chemical nature of their composition. The samples must be some cm size to fit inside the vacuum chamber and usually for non-conductive samples a coating is applied. For non-perfectly layered surfaces the samples must be polished in order to have a flat surface and to the beam to invest the surface perpendicularly. In this case study the presence of highly conductive graphite requires no coating and samples have been polished and placed on a stage inside the vacuum chamber. Examples of how the samples are placed inside the equipment and example of different magnification of the images obtained in Figures 21-22. Hitachi TM3030 microscope equipped with energy dispersive X-ray spectroscopy (EDX) has been used. A 5 kV accelerating voltage has been employed for the micrographs whereas the EDX analysis was performed at 15 kV.

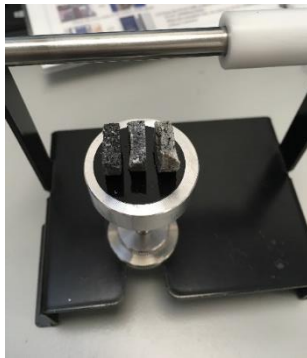


Figure 21 - Example of samples considered for the SEM Analysis

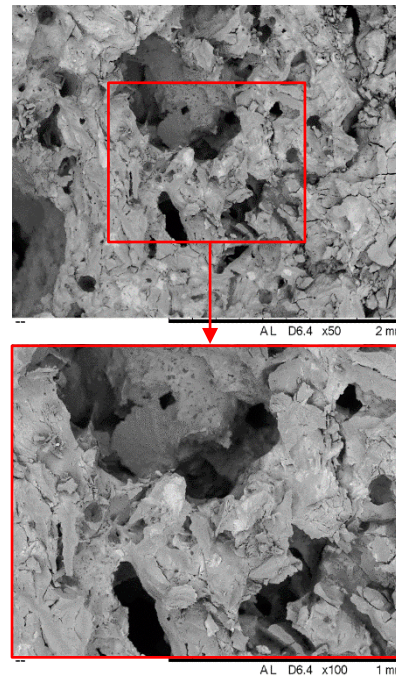


Figure 22 -- Example of different magnification results from the surface of one of the samples analysed for this specific case study.

## Post-processing

Digital images that are the result of scanning/acquisition technologies are usually affected to several types of noise sources. Indeed, filtering techniques are useful to remove noise and other kind of artefacts by applying to pixels some neighbouring operations, where the value of each pixel is averaged/weighted by the values of the surrounding pixels according to different filtering algorithms.

In particular, SEM and EDX imaging scanning are exposed to noise effects which are critical at high acquisition rates. Several studies in literature have highlighted different such kind of noise sources according to the features of the equipment devices involved from the scanning to the final acquisition process and have set up methodologies on how to tackle, quantify and possibly remove or reduce them. They have been distinguished into primary and secondary emission sources (due to backscattered emission effect) and on other components of the detection system. Additional and unavoidable sources of noise are represented by electronics accounting for the signal conversion to the end-user graphical interface. Generally, the noise effects produced by primary and secondary emissions are a consequence of the statistically random fluctuations introduced by the beam of electrons which can be modelled statistically by a Poisson distribution. On top of that, some scholars claim that noise introduced by secondary detecting and conversion systems, like additional fluctuations introduced by photomultipliers and photocathode, are less impacting and can be modelled according to a Gaussian law. Besides, considering that the overall final image is the direct final consequence of the signal conversion, many studies have evaluated the noise-to-signal ratio (NSR) as a parameter to evaluate the quality of the image starting from the final image output. [45] [46]

Despite the in-depth analysis conducted in literature, in most of the cases it is still difficult to distinguish in a precise way the specific origins of the artefacts in a SEM/EDX image, these are in fact also strictly connected not only on the conditions applied but also to the specimen and how the electron beam shots it. Post-processing techniques are, as a matter of fact, necessary in order to have a clear understanding of how the components of a multi-phase sample are distributed in a semi-quantitative way. After a trial-and-error approach, the pictures for the present study have been filtered with a Gaussian filter and showed in Figure 23.

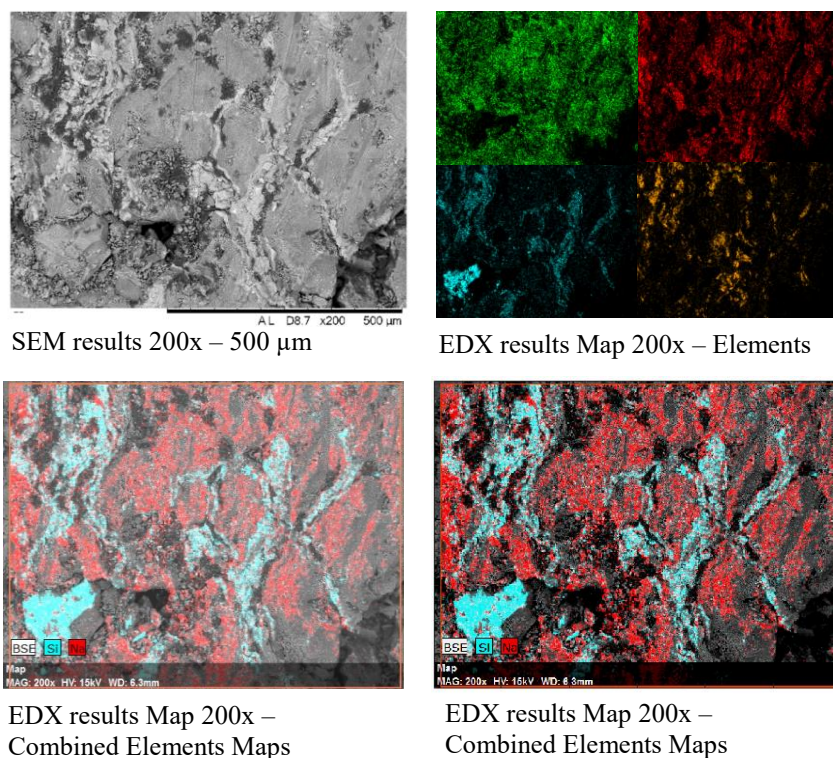


Figure 23 - EDX elemental mapping before and after post-processing.

### 3.6 X-Ray micro-Tomography (XRT)

Another fundamental technique adopted to complete the structural analysis of the specimens has been the high-resolution X-Ray micro-Tomography. The equipment used is the multiscale X-ray tomograph SkyScan-2211 which allows a 3D non-destructive analysis of the samples and of their internal reconstruction in the range between >200mm to sub-micron level. The system used is composed of an X-Ray source and two X-ray detectors one for large or highly dense objects and another for smaller specimens. The X-ray tomography is a widely used technique for non-invasive analysis in the medical field but also for other industrial purposes.

As shown in Figure 24 (left), the functioning principle is based onto cone beam reconstruction where a cone-shaped beam is emitted by an X-Ray source onto a sample placed in the middle of the trajectory from the source to the 2D detector.

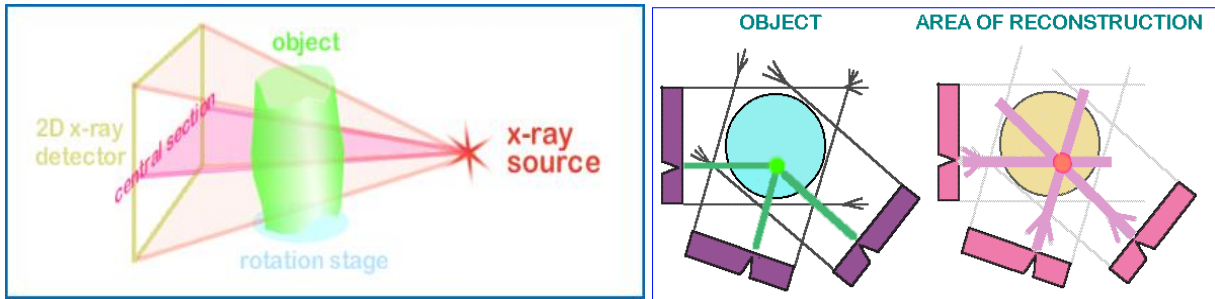


Figure 24 - Functioning principle of X-Ray Tomograph (left), Reconstruction technique of the digital images from the XRT (right).

Ever since the 3D specimen is invested by the beam the detector collects shadows out of it producing the first two-dimensional reconstruction. Every point in the shadow image of the object produced can be considered as carrying information about the absorption of the 3D object which is in the trajectory of the partial X-Ray beam. Each point of the 2D representation is allocated into the computer memory as a pixel corresponding to the possible displacement of the object, the following reconstruction of the same object must be in the same field of view. Thanks to the rotation of the stage holding the sample several 2D reconstructions are produced and, as far as the shadows are collected from different rotation angles, the actual localization of the absorption point of the beam is registered. During this process, and according to the rotation speed and steps, the projection and reconstruction area decreases to a single object point, this operation is called “back-projection”. The increasing number of shadow projections collected from different views produces a more precise localization of the absorption point and the more is possible to obtain higher quality images. An example of different views collected starting from one-dimensional reconstruction is shown in Figure 25.

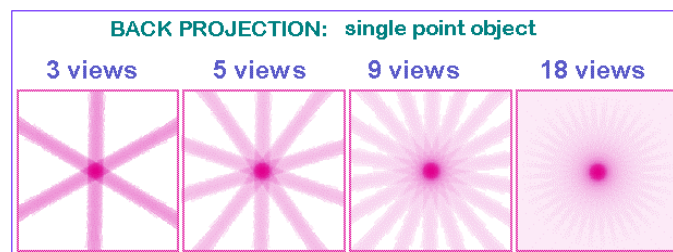


Figure 25 - Detail on single point object reconstruction.

Once the acquisition phase ends, the actual final reconstruction of the digital image can be started. Several algorithms are used in this phase from the raw data collected for each cross-sectional slice, where the raw data is a matrix of numbers of absorption values. This technique however doesn't count only the acquisition phase conducted with the actual Tomograph but also complementary software should be used to complete the analysis and to provide a quantitative evaluation of the structure of the specimen. A summary of the main steps which have been followed is listed into the diagram in Figure 26.

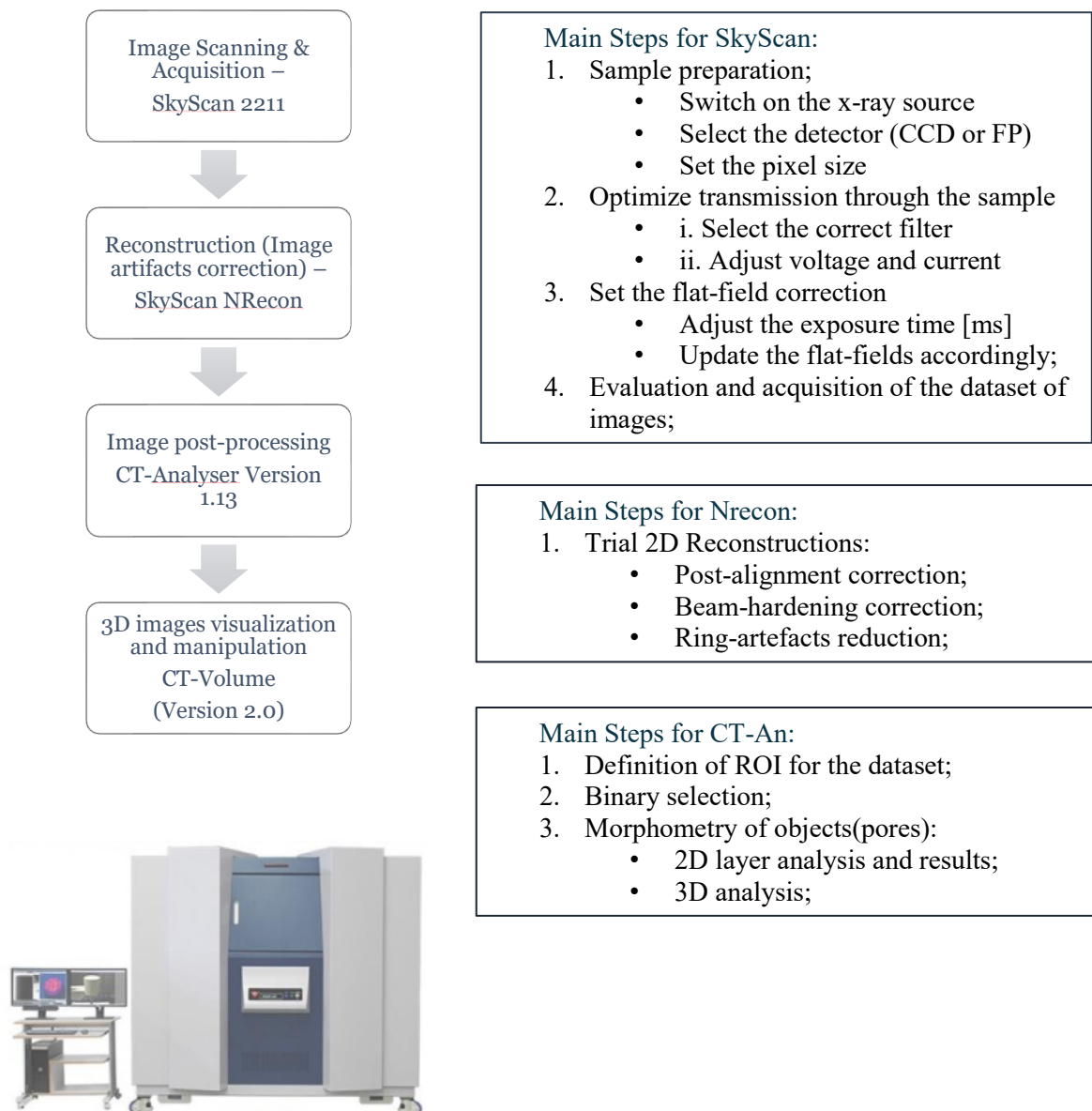


Figure 26 - Flow diagram of the chronological main steps followed to complete the X-Ray analysis.

As a reference in Table 3 are listed the conditions for the scanning of this specific sample composition. Conditions for subsequent steps for the reconstruction and elaboration of the images have not been provided because strictly dependent on the acquisition quality obtained during the scanning phase and the density and structural features of the specific sample.

Table 3 - Acquisition conditions for guideline to future works dealing with similar high-dense composites

---

**[Acquisition] properties:**

---

Source Voltage (kV) = 100  
Source Current ( $\mu\text{A}$ )= 200  
Source focus mode =Micro focus  
Number of Rows = 1536  
Number of Columns = 1920  
Image Rotation =0.0790  
Exposure (ms) = 100  
Image Pixel Size ( $\mu\text{m}$ ) = 9.95  
Scaled Image Pixel Size ( $\mu\text{m}$ ) = 9.95  
Object to Source (mm)=38.125  
Inclination in lifting( $\mu\text{m}/\text{mm}$ ) =0.919  
Vertical Object Position (mm) =26.000  
Filter=No filter  
Depth (bits)=16  
Rotation Step ( $^\circ$ ) =0.200  
Use 360 Rotation =YES  
Type of Scan =Flat-Panel  
Estimated scan time =00h:39min

---

### 3.7 Digital Image post-processing for micro-structural investigation

Image post-processing methods include filtering techniques on images (like those applied to EDX maps) as well as pixel-based neighbouring algorithms allowing a connection with physical microstructural properties of both grayscale or binary images. Guidelines providing an insight on specific arithmetic, logical and morphological operations on digital imaging techniques have been widely detailed and referenced in [47] and [5].

#### Inputs:

- Grayscale image;
- User selection of a Region of Interest (ROI);
- Resolution of the image (9.95  $\mu\text{m}/\text{pixel}$ );
- Diameter of the sample;

#### Outputs:

- Areal porosity, tortuosity of pore objects and average tortuosity;
- Objects properties like: axis lengths, perimeters, areas, equivalent diameter and coordinates;

- Pore size distribution;
- Tortuosity distribution of pore objects;

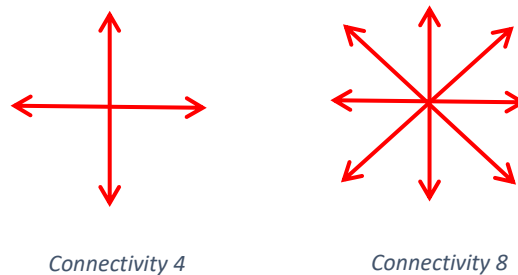
List of the basic steps performed in Matlab environment:

1. Read the grayscale images obtained from the XRT scanning and reconstruction software.
2. Evaluate the application of additional filtering on the grayscale images (sometimes is not a recommended solution, it may overestimate porosity).
3. Choice of a thresholding method, usually it's used the global Otsu method. Additional information on segmenting procedures are detailed in [47] [48,49] .

The effectiveness of segmenting methods is usually connected to the quality of the acquisition of the images. In this specific case the thresholding has been set manually by a tune-and-check approach on the final output images.

4. Morphological operations on the segmented image have been applied: small speckles have been removed and then opening operation has been performed.

Specifically, white connected objects with fewer than 10 pixels have been removed under the assumption that they are too small to be considered actual pores or alternatively that they can be a result of defects obtained with the signal-to-digital image conversion. Each pixel may be deleted with a fixed connectivity, this means that it can be discarded if it's connected to another element with a pre-set connectivity 4 or 8 in a 2D surface.



Opening morphological operation includes an erosion and subsequent dilation operation on pixels by using a structuring rounded element of a fixed radius.

1	1	1	0	1	1
0	1	1	0	0	0
0	1	1	1	1	0
1	1	1	1	0	1
0	0	1	1	0	0
1	0	0	1	1	0

After setting a structuring element, the central pixel is evaluated according to its neighbouring pixels, dilation produces as output the maximum in the neighbouring pixels while erosion the minimum. From a binary image the output will be still a binary image with 1 or 0 as pixels.

Erosion:

0	1	1
0	0	0
1	1	0

Dilation:

0	1	1
0	1	0
1	1	0

5. Selection of a Region of Interest according to the shape of the layer sections considered (whether cross or coronal section layers).
6. Creation of a mask from the ROI selection, this is performed with a true/false operation on the pixels inside/outside the ROI area respectively. The creation of a mask allows to separate the main porous matrix area from the pores and the background. When the mask is applied on the source binarized image it can isolate the objects (that are the pores) for the porosity analysis. Reference of this operation is shown in Figure 27 (A)-(B).

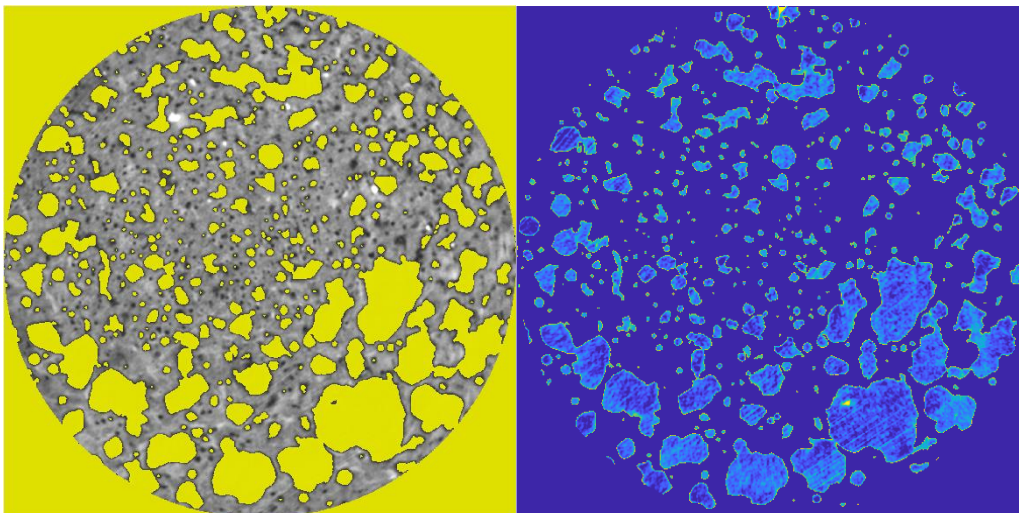


Figure 27- [A ],[B]: (A) Mask obtained from ROI, (B) Application of the mask in the source image to highlight only the pore objects.

7. The Objects analysis is based onto topology features of the white pixel objects (which physically correspond to pores). Several properties of the objects have been analysed and collected into a structure.  
The objects are identified as areas of white pixels as a consequence of a flood-fill algorithm that keeps/not the colour of each following pixel according to the colour of the previous one until a boundary pixel with a different colour is reached.

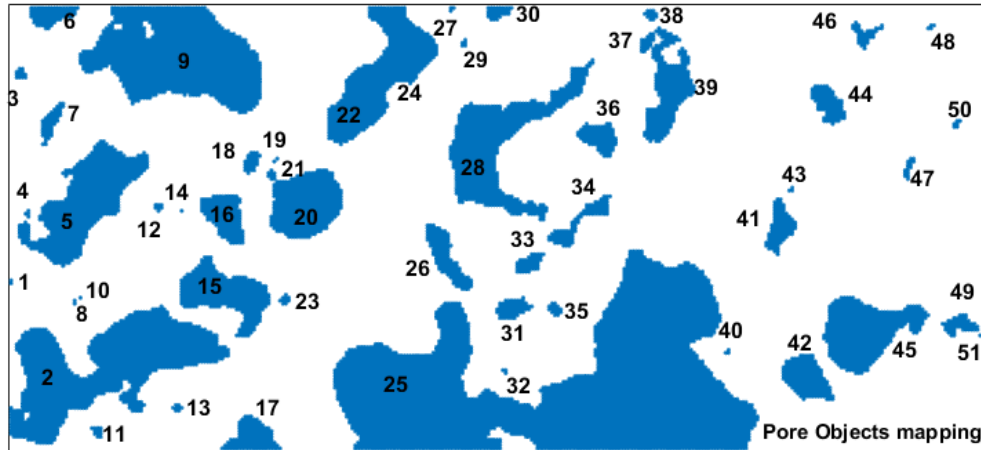


Figure 28 - Pore object analysis example on a reduce ROI selection.

8. Areal porosity has been evaluated from the total area of white pixels over the total ROI area while for the pore size distribution the equivalent pore diameter of each object has been considered.
9. A Skeletonization (or thinning) procedure has been applied to the pore objects. It is an iterative pixel contour deletion method performed until a final one-pixel-width skeleton composed of several segments is reached. The final task here has been to individuate the connected segments to obtain properties of each them. In order to have a clearer and more in-depth knowledge of how these thinning algorithms work, the reader is referred to [50].

The main purpose for this category of algorithms is to perform neighbouring pixel operations while maintaining the basic connectivity of the image patterns.

The main connection between these pixel-based operations and the physical properties of the samples is based on the assumption that pores are actual micro-structured pathways able to hold and transport the melting salt. Such algorithms allow to simplify the micro-structural study without altering the image patterns. An example of this procedure on a reduced square ROI is shown in Figure 29. From this procedure segments properties have been obtained.

10. Tortuosity and tortuosity distribution have been calculated from the skeletonized image. For each  $i$ -th segment, tortuosity has been evaluated by evaluating the pathlength of each segment and the distance between its endpoints. The final tortuosity is evaluated as the average tortuosity on all the segments.

$$\tau = \frac{path_{length}_i}{distance_i}$$

Where the distance of each  $i$ -th segment is computed as the Euclidean distance between endpoints of the segments. Endpoints can be calculated only on a skeletonized patterned image. An example of output image related to the skeletonization of a highly porous sample is shown in Figure 29.

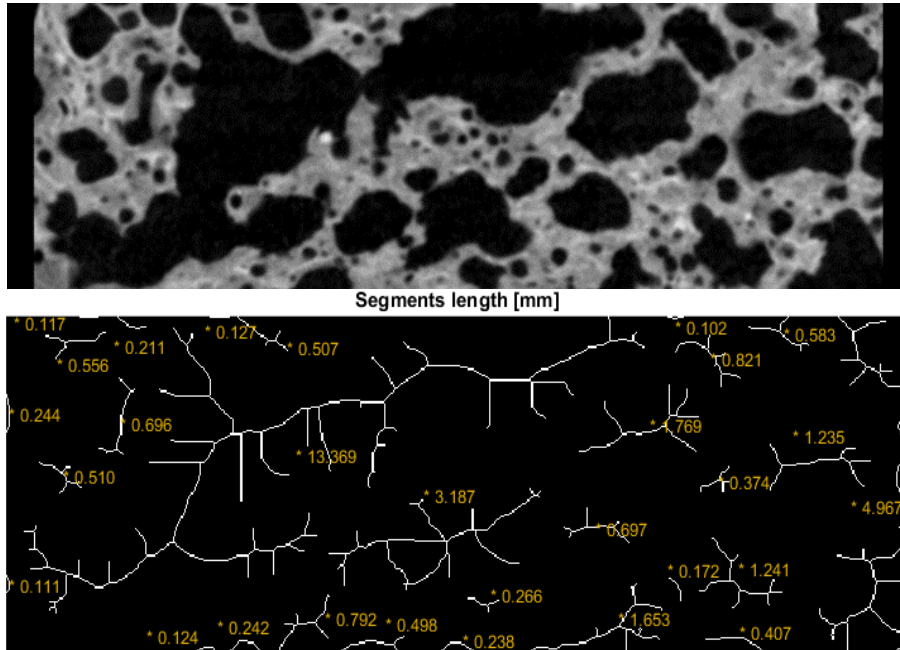


Figure 29 - Skeletonization procedure from a source image of a coronal section layer.

## 4 Experimental results

### 4.1 Materials experimental selection and characterization

This Section will deal with a more detailed experimental investigation and discussion of the results obtained by all the techniques outlined in Section 3.

Criteria for the selection of the components and the definition of the final formulations range from chemical, thermo-physical, to economic specifications. The main requirement for the choice of the FPCM presented is the high energy density reached in a medium-high temperature range, the formulations operate in the range 25-300°C referred to heating cycles.

The Solar Salt which has been selected as PCM is a eutectic of NaNO<sub>3</sub> and KNO<sub>3</sub>, supported by Vermiculite host material and Graphite as thermal performance enhancer. One of the main criteria for the selection of such formulation is connected to chemical compatibility, all the components show no chemical decomposition in this temperature range, additionally they do not cause fire or explosion hazard and they are non-toxic, so that they can be easily handled safely and applied for a wide variety of applications.

As widely reported in the State-of-the art analysed form shape-stabilized PCMs, the adoption of the Vermiculite, as many other clays/phyllosilicates, is the main contributor the overall shape-stability of the composites. [33,39,51–54] The main reason for selecting such kind of structuring or supporting materials is connected to their high free surface area and absorbability, in the specific case of salts it has good interfacial energy so that, Vermiculite is prone to be wetted by the Solar Salt. Benefits, like other ceramic materials account for high specific heat capacity allowing to exploit high amount of heat from the sensible heat fraction due to temperature change. One drawback is connected with their low thermal conductivity, in order to solve this graphite has been selected to take part to the shape-stabilized porous structure as a thermal conductivity enhancer. Compared to many other studies adopting graphite in his more porous expanded form or in foam-like structure [22,25,55], in this case-study graphite has been dispersed and mixed with the other components to form the overall structured matrix.

Lastly but not of least importance, the main driver for the investigation of such formulations is the cost-effectiveness of the materials involved whose prices range in a wide spectrum because they are widely available in the market but most of all the low expenditure for the fabrication process which make them suitable for large-scale applications.

### 4.2 Fabrication of the pellets

The eutectic mixture of Potassium Nitrate KNO<sub>3</sub> (purity >98%) and Sodium Nitrate NaNO<sub>3</sub> (purity >98%) in 40:60 wt% has been considered as the PCM material. The Vermiculite has been adopted as supporting material (SM) and graphite (Cg) (particle sizes 95% < 53µm) have been added in different mass contents to track thermal performance enhancement.

Table 4 and Table 5 show the composition of Vermiculite and Graphite adopted for the formulations.

Table 4 – Vermiculite composition

Composition	SiO <sub>2</sub> %	MgO %	Al <sub>2</sub> O <sub>3</sub> %	Fe <sub>2</sub> O <sub>3</sub> %	K <sub>2</sub> O %	CaO %	TiO <sub>2</sub> %
Vermiculite	46.0	27.5	9.8	9.0	2.8	2.5	1

Table 5 – Graphite composition

Composition	C %	S %	N %	Ash %	Volatile %	Moisture%
Graphite	98.6	0.05	0.05	0.8	0.3	0.3

### Manufacturing procedure:

The fabrication procedure adopted to deal with FPCM or SSPCM consists into three different steps: Mixing, Tableting and Controlled cooling. Every stage of the manufacturing of the final tablets has been refined with a trial-and-error learning procedure according to the previous experience in this field of research.

Since the main purpose of the experimental part deals with gaining a deep understanding of the shape-stability concept, the first experimental outcomes have been those resulting from the sintering stage, which consists in a Leakage test. After pushing to temperatures higher than the melting point, the pellets have been tested to track leakage issues and to have a better clue on which are the parameters that can be changed in order to refine or increase the quality of the fabricating procedure thus assessing the most form-stable composite formulation. All the steps are shown in Figure 31.

### Mixing and Tableting

The first stage consists in a mixing procedure of the components of the formulations initially in powder form. In the study, the final samples fully characterized have been fabricated with a Vermiculite particle size of 3 mm, particle sizes of KNO<sub>3</sub> and NaNO<sub>3</sub> and Graphite are in the range ~ $\mu$ m - ~nm. All the materials used to produce the final tablets have been purchased from suppliers in the market for industrial applications. The tableting of the 13 mm diameter and 1 g weight pellets has undergone through uni-axial cold-compression conducted by means of compressing machine at 20 MPa with a preload of 5.6 N held for 1 minute.

Every step of the manufacturing process may impact in an enormous way when dealing with SSPCM, parameters like compressing pressures, increase/decrease of the components, particle sizes and the nature of the subsequent sintering process may totally change the outcomes of the Leakage tests leading to the loss of PCM from the holding matrix thus not guaranteeing the stability of the tablet. Additional complications might arise if dealing with non-thermally and non-chemically stable composite materials causing uncontrollable and unpredictable behaviour towards shape-stability at higher temperatures. In this case, all the materials involved are thermally stable in their operating range and chemically inert amongst them even at higher temperatures under their degradation temperatures.

The final six formulations presented in this section and characterized are the result of the most refined conditions after striking the balance amongst all the listed possible set of parameters.

## Sintering and controlled cooling

The compressed tablets have been placed into petri plates and covered with an alumina plate on top to avoid direct radiation effects and non-homogeneous sintering. Three thermocouples have been placed inside the furnace in contact with the sample, on the bottom in direct contact with the petri plate and one free in the furnace respectively. The application of external thermocouples additionally to the control system of the furnace allowed to make sure that the samples reached the target temperatures of 220°C and 300°C and to have an insight on the functioning of the furnace considering possible delay due to its initial inertia. An example of the temperature tracking to visualize this effect is shown in Figure 30.

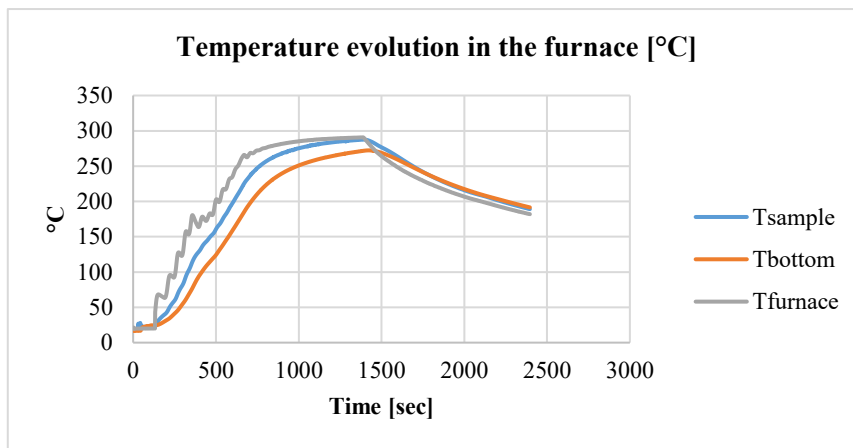


Figure 30 - Thermocouple tracking inside the furnace during sintering process of the tablets.

This process is just an example of the fabricating processes adopted in literature to produce FPCM samples, many others like impregnation method of a SM matrix have widely proved to be valid options however, the sintering process at a temperature slightly higher than the Solar Salt melting temperature is surely one of the most economically convenient solutions.

The sintering process has been conducted in a furnace by setting a default heating program:

- Heating from 25 °C to 220°C with a 10°C/min heating rate;
- Isothermal step at 220°C for 10 min;
- Heating from 220-300 °C with a 5°C/min heating rate;
- Isothermal step at 300°C for 1 hour;
- Controlled slow cooling down of the pellets inside the furnace.

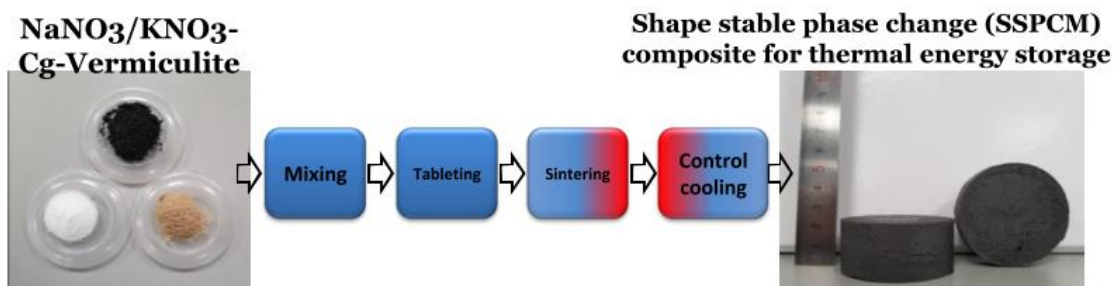


Figure 31 - Manufacturing steps for the SSPCMs tablets.

The starting step is higher than the second one to win the starting inertia and to speed up the heating of the furnace. The choice of the target temperatures is connected to the melting point of the PCM inside the SSPCM, in the following steps temperature has been pushed over the PCM's melting point and held for an interval of time in order to complete the sintering process of the pellets and afterwards to test the leakage of all the samples.

The characterization has been set up starting from six different formulations with 3 mm of Vermiculite particle size to test as a starting point whether they face leakage issues or not. The driving concept revolves around analysing the impact that different contents of PCM solar salt (high and low contents) has on the overall shaped and sintered samples while evaluating different graphite contents, from low, medium to high. Meanwhile, increasing the loading of graphite in the formulations allows to track progressively the extent of the enhancement of thermal properties and to detect if graphite plays a relevant role also from a structural point of view when combined with Vermiculite. A summary of the final formulations is shown in Table 6. Specifically, the 55% wt of Solar Salt states as for Low and 75% for High PCM content respectively. Similarly, Graphite content (Cg) ranges between 1% (Low), 5% (Medium) and 10% (High). Table 6 shows also the results of the Leakage tests, for replicability issues each test and has been repeated around five times.

*Table 6 – Summary of the formulations and results of the leaking test after the heat treatment of the pellets.*

Formulations	Eutectic content wt%	Graphite wt%	Vermiculite wt%	Leaking Test
S501	55 %	1 %	44 %	Yes (Minor)
S505	55 %	5 %	40 %	Yes (Minor)
S510	55 %	10 %	35 %	Yes (Minor)
S701	75 %	1 %	24 %	Yes
S705	75 %	5 %	20 %	Yes (Minor)
S710	75 %	10 %	15 %	No

From this preliminary test towards shape-stability evaluation, starting hints suggested that samples S501, S505 and S510 that the high content of Vermiculite with a lower PCM-content composites is likely to support and sustain the PCM inside the host matrix. On the other hand, although in samples S701, S705 and S710 the increasing content of graphite seems to foster the overall supporting capacity of the matrix, this last subset has shown to be more prone to leaking issues due to the pellet's high PCM content. Repeated tests in the same conditions have however showed the same results suggesting that a correlation might exist between the graphite loading and the shape-stability.

Figures 32-33 provide a top and bottom view of the tablets produced after sintering to visually show the leaking effect of the salt from the host matrix.

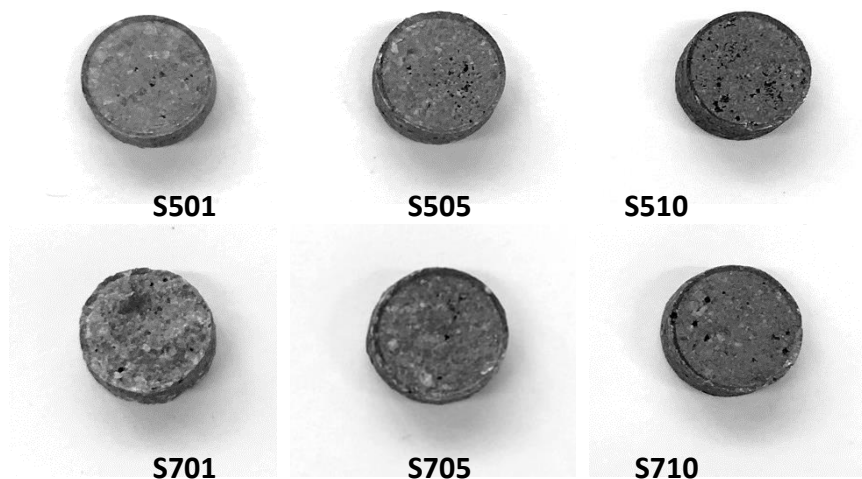


*Figure 332 - Top surface view of manufactured pellets according to different formulations.*



*Figure 323 - Bottom view surface layer of the sintered samples.*

### **Sintering insights**

The sintering process plays a fundamental role in the formation of the microstructures in the composite. According to Zhiwei et al's after the compression of the pellets, the sintered composite is the result of contemporary and competing processes of rearrangement along with densification and swelling due to the presence of ceramics and carbon-based materials respectively. [38]

These processes may occur at different rates according to starting dimension, orientation, non-uniform distribution and impurities of the particles involved and most of all to the compressing conditions considered. Sintering as well as sample heating and cooling at subsequent cycles, result in differences in the porosity, free surface area, actual density and volume but also in shape and in the components distribution and morphology.

This may suggest that, sintering and subsequent cooling down at room temperature occurring before re-cycling (at lower temperatures) may create a definitive and reinforced final internal matrix with respect to other fabrication processes.

#### 4.2.1 Effect of fabricating pressures and particle sizes

The selection of all the manufacturing conditions and parameters to obtain replicable thus reliable outcomes is a result of a large set of fabricated pellets (around 150 pellets ) and variable parameters. Most important, the investigation of variable fabrication conditions has the final goal of addressing the underlying principles about shape-stabilized PCMs and how the different components constituting the composites behave to enhance or overturn such tendency of containing the salt in a compact matrix. The impacting parameters which affect the form-stability, by mixing and compressing and subsequent heat treatment include:

- Fabricating pressures (for uni-axial cold compression);
- Particle sizes of the supporting material;
- Effect of graphite in the formulations;
- Effect of the eutectic salt in the formulations;
- Effect of the salts' particle size;

As a starting point, in order to address such issue, the logical process adopted, shown in Figure 34, consisted in testing two larger sets of pure salt with increasing Vermiculite particle sizes and increasing fabricating pressures. In order to simplify the test conditions, the pure Sodium Nitrate ( $\text{NaNO}_3$ ), present in 60% wt in the eutectic mixture has been considered (the testing of pure salts is more predictable and properties are well-known). The first set included two slots of experiments (Figure 35-36), including formulations with and without graphite and with a pure salt content of 50%. Not too high salt loading should guarantee that the nitrate is held inside the host matrix. In a second stage, once highlighted the ideal compressing pressure, the loading of salt has been increased.

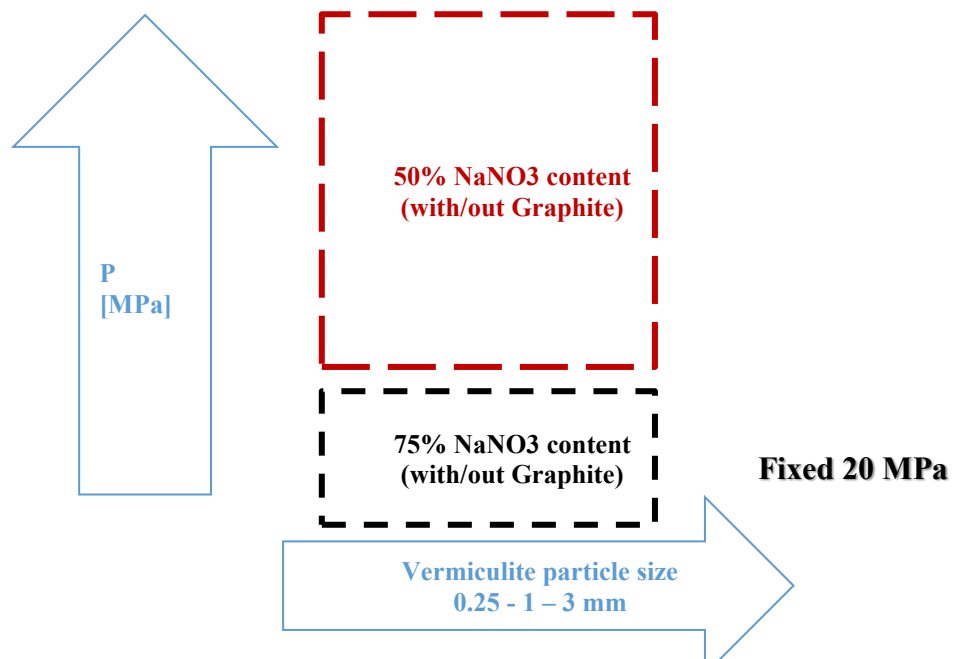


Figure 34 - Procedure adopted to test the most suitable manufacturing conditions for the FPCMs formulations.

**50% Pure NaNO<sub>3</sub> samples – No Graphite – Top view**



*Figure 36 - Effect of increasing pressures and increasing particle sizes on non-graphitic pure salt pellets.*

**50% Pure NaNO<sub>3</sub> samples - 10% Graphite – Top view**

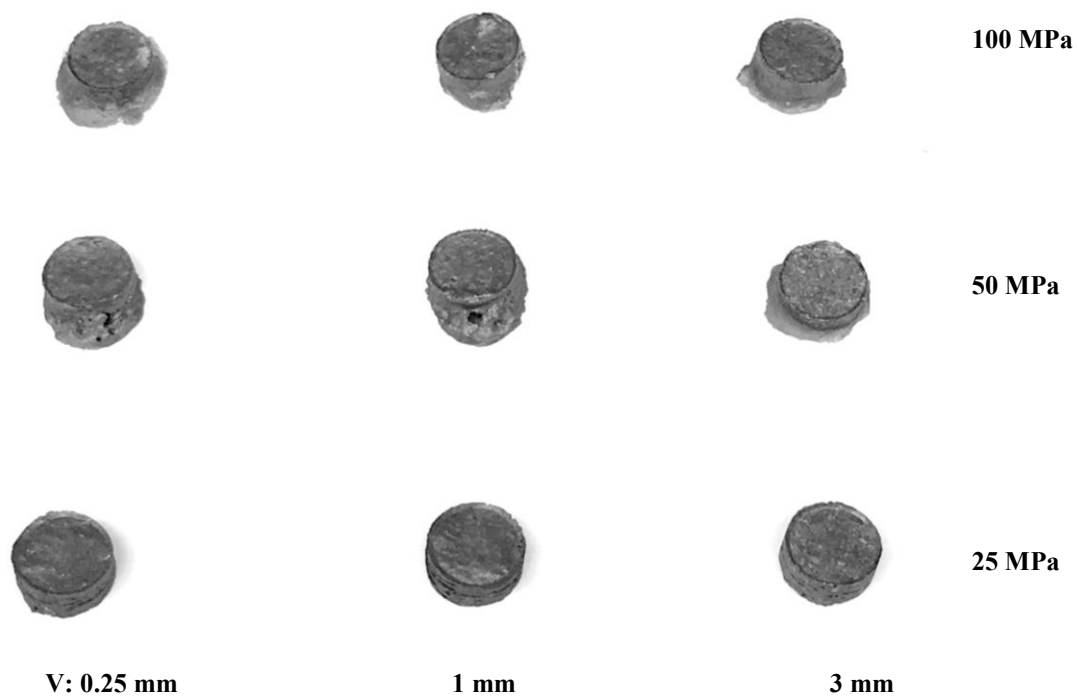


*Figure 35 - Effect of increasing pressures and increasing particle sizes on graphitic pure salt pellets.*

The temperature program of the heat treatment was changed according to the melting point of the pure NaNO<sub>3</sub> which is around 308°C:

- 10 °C/min heating rate from ambient temperature to 328°C;
- 5°C/min from 328°C to 350 °C;
- Hold 1 hour at 350 °C to allow the sintering.

Results from Figure 35 showed that the increasing fabricating pressure on non-graphitic pellets, shows a more significant leakage interesting also the upper surface of the tablets, in fact higher pressures do not accommodate the natural volume expansion of the salt. This leakage effect can be tracked with the increasing pressures and lower particle sizes (especially with 0.25 mm of Vermiculite). Consequently, low pressure tablets are more shape stable in general, with some minor leakage detected in higher particle size (this may be due to higher porosity). Overall, these tests conducted between two and three times for each pellet, suggest that Vermiculite has a higher absorbent potential towards the salt for its high wettability creating a more shape-stabilised structure, but it can also easily release the PCM. Once added the graphite in 10% wt inside the formulations, most of the tablets swelled and deformed greatly due to the lower Vermiculite content along with higher pressures as shown in Figure 36. The underlying reason for swelling and leaking is however due to the low interfacial energies of the graphite particles [41] which glide on the salt surface in the liquid phase surrounding it. Apparent size stability is detected with lower pressures and higher particle size (3 mm of the Vermiculite), this may suggest that higher particles may increase the probability of creation of microstructures (which allow the flowing of the melting salt and holds it in the solid phase) counteracting the potential of the higher total free surface area of the smaller Vermiculite particles.

In conclusion, tests reflect that a certain amount of volume expansion space is necessary to let the salt flow in the matrix and to allow a more controlled graphite swelling. In order to structurally hold the salt while ensuring a minimum porosity for volume variations, when dealing with Vermiculite-based composites, lower pressures should be considered.

In a second stage, by fixing the compressing pressure at 20 MPa and pushing the salt content up to 75% wt, formulations with and without graphite and different particle sizes have been tested, results are shown in Figure 37. According to this last set of samples, leakage is detected in every pellet without graphite tested, this shows that too high content of salt leads inevitably to leakage compared to 50% content. Moreover, small deformation due to the salt expansion is shown in no graphite pellets while minor leakage is detected in samples with low particle size with graphite leading to the formulation with 75% pure salt, 20 MPa and 3 mm Vermiculite particle size to be the best conditions tested.

Other important expedients to keep in mind is the well-mixing to allow a complete and more homogeneous sintering and avoid cracking due to areas without the blending effect of the salt and, in addition to this, for this study and according to these conditions, grinding the salt particles increases the leakage probability by enhancing the liquid salt to flow throughout the matrix because it is better mixed. Lastly, covering the petri plates with alumina crucible allows to reduce the direct irradiation which creates enhance deformation effects on the surface layer of the pellets as shown in Figure 38. In conclusion, in order to acquire high salt and graphite loadings (for performance targets) while keeping form-stability it's necessary to strike the balance among all the fabrication conditions and other components' related features.



*Top view*



*Bottom view*

*Figure 37 – 75% Pure NaNO<sub>3</sub> at 20 MPa and different particle sizes.*

### *4.3 Density and porosity measurements*

As mentioned in Section 3 and 4.2 the sintering process dealt with the manufacturing of the six starting formulations' tablets, is not exactly a sintering process as usually performed for ceramics and in the metallurgy field, the latter require temperature way higher than 300°C which is the maximum temperature allowable in this specific case to avoid degradation of the main constituent (Solar Salt) and to avoid excessive deformation of the pellets. One of the main properties which may provide hints of the underlying mechanisms involved when sintering is the density measurement of the pellets which has been conducted both by calibre and weight measurements and Helium Pycnometer by AccuPyc II 1340 Pycnometer. The first measurements allowed the calculation of the bulk density while the latter was used to measure the effective density.

Density measurements are important because they also provide a guide for the formulation procedure and reflects the quality of the manufactured products. While on the one hand the density measurements of a solid and rigid sample is a straightforward task, measuring density of composites with irregular size should be more carefully addressed. The latter can in fact include cracks, pores tortuous passageways and may lead in some cases to inaccurate results. This can be partly avoided by measuring the effective density through the pycnometer which can also be referred as real, apparent or skeletal density and it is obtained by excluding pores or any void space inside the bulk composite. The one adopted for the samples of this specific case study is a non-destructive method with a gas being purged through the specimen, this provides the most accurate evaluation when dealing with porous composites. Measurements have been conducted for the whole set of the six samples and are shown in Figures 39-40. Results from Figures 39-40 have been conducted by measuring each composite twice and evaluating its relative error. Both the subset of samples showed the same behaviour when pressed by means of the compressing machine at 20 MPa before any heat treatment, this effect is clearly due to the consequent reduction of void space amongst the powdered materials. When comparing the two subsets of formulations, the 55%-PCM set shows higher density values due the higher Vermiculite contents, the 3 mm particle size contribute to the formation of slightly bigger pellets because of the high void volume occupied by the casual arrangement of the Vermiculite particles across the skeleton. On the other hand, a different trend is detected after the sintering process between the two subsets where higher compaction is registered for samples with higher content of Vermiculite in the 55%-PCM samples while for the 75%-PCM samples corresponds to the lower Vermiculite content ones. These results may be a result of the decrease in volume of interconnected pores and a subsequent increase of the interparticle contact areas among Vermiculite particles which have high surface energies.

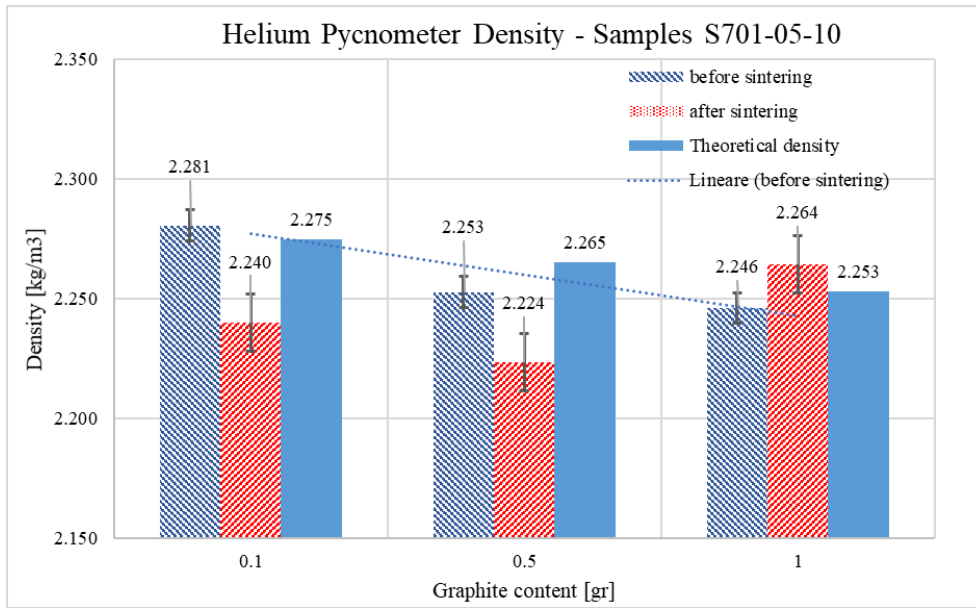


Figure 38 - Effective density measurements of Samples S701-05-10 (75% Solar Salt, 1%/5%/10% Graphite content).

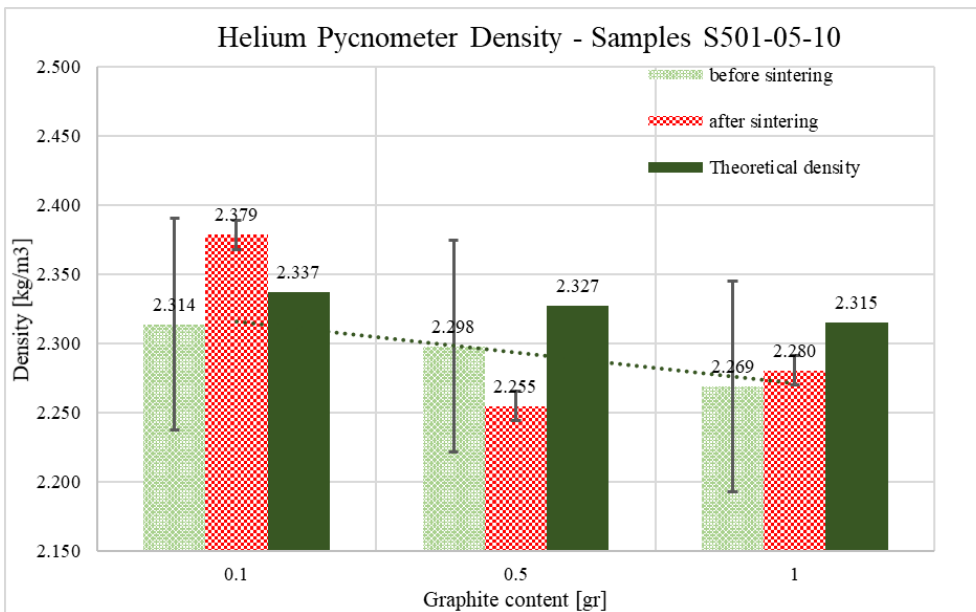


Figure 39 - Effective density measurements of Samples S501-05-10 (55% Solar Salt, 1%/5%/10% Graphite content).

In order to have a preliminary estimation of the porosity of the green pellets, and to have an idea about how pore formation affects the composites bulk volume, the measurement of the bulk density is fundamental as shown in Equation and Figures 39-40. As previously mentioned, the bulk density is a measure of the volume density when including the pore volume.

$$\varepsilon = 1 - \frac{\rho_{bulk}}{\rho_{actual}}$$

## S701/S05/S10 - Porosity measurements

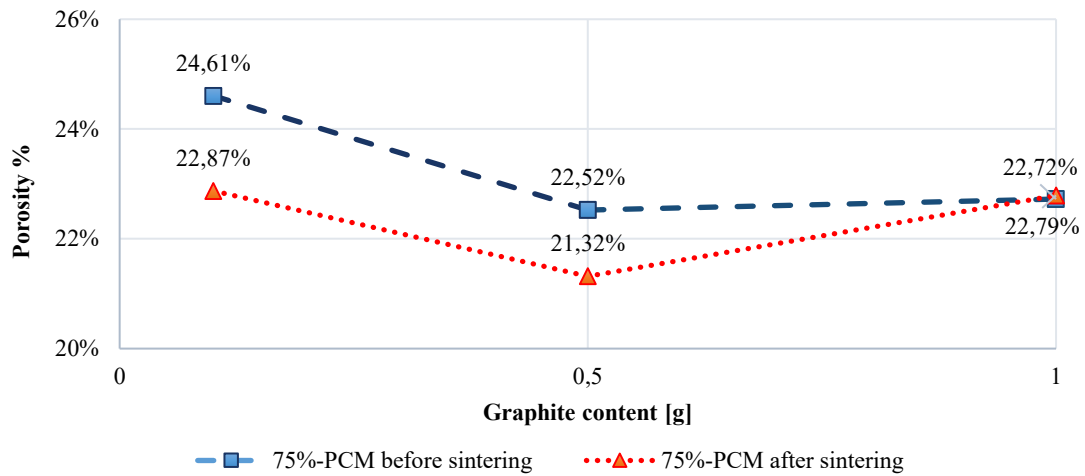


Figure 40 - Porosity measurements taking into account the bulk densities obtained by calibre and weight measurements of 1 gr pellets. Samples considered: S701/07/10 with 75% Solar Salt and variable Graphite content.

Figure 41 clearly clarifies the theory of the compaction effect promoted by the melted and solidified PCM inside the porous host matrix which reduces the porosity between the before and after sintering stages. However, porosity values range around 20 – 25% for all the samples (as also shown in Figure 42) denoting a minimum necessary porosity specific for these formulations and at the compressing pressure and times applied during the cold compression phase. The same trend described for Figure 41 for the 75%-PCM set, is also shown for 55%-PCM samples in Figure 42. In both cases a turning point is shown when the Graphite content increases, this can be a consequence of the competing surface energies of Vermiculite and Graphite towards the Solar Salt, so that the Graphite (which has poor absorbability of the Salt) increases the swelling effect of Graphite widely explained and supported by SEM tests in Section 4.6.1.

## S501/S05/S10 - Porosity Measurements

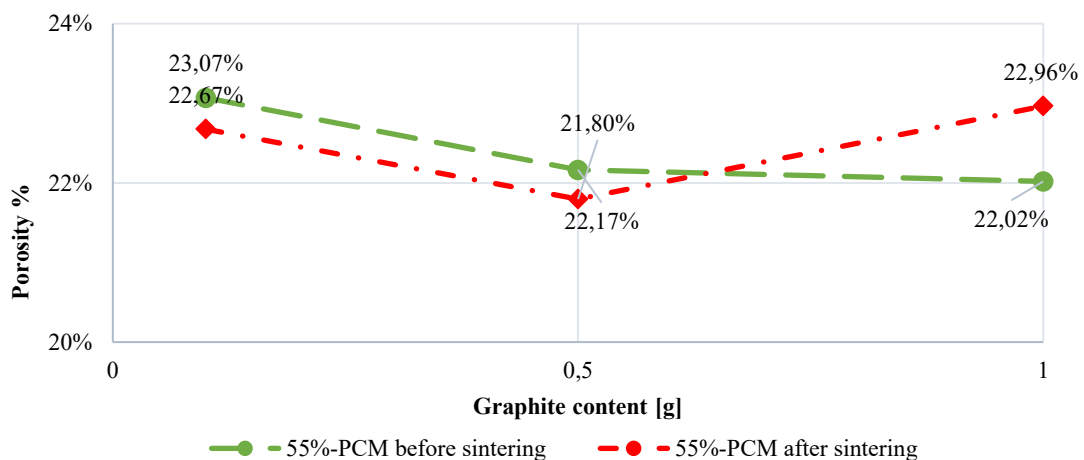


Figure 41 - Porosity measurements taking into account the bulk densities obtained by calibre and weight measurements of 1 gr pellets. Samples considered: S501/07/10 with 55% Solar Salt and variable Graphite content.

For highly porous composites like the manufactured green pellets this specific kind of sintering (occurring at lower temperatures) is the result of pore rearrangement and the compacting effect of the Solar Salt in the liquid phase. The theory behind these highly dense matrix structures is explained by Figure 43, where the effect sintering is a multi-stage process developing along with temperature increases. The powder-like particles during the heat treatment start to densify and to form necks and interconnected passageways to reach a compact structure as shown in Stage III. The only missing point that distinguishes this particular sintering process pushed to 300°C with respect to the actual sintering of ceramics shown in Figure 43 (up to >1000°C) is the final stage where the isolation of pores occurs due to the grain growth and diffusion phenomena occurring at higher temperatures.

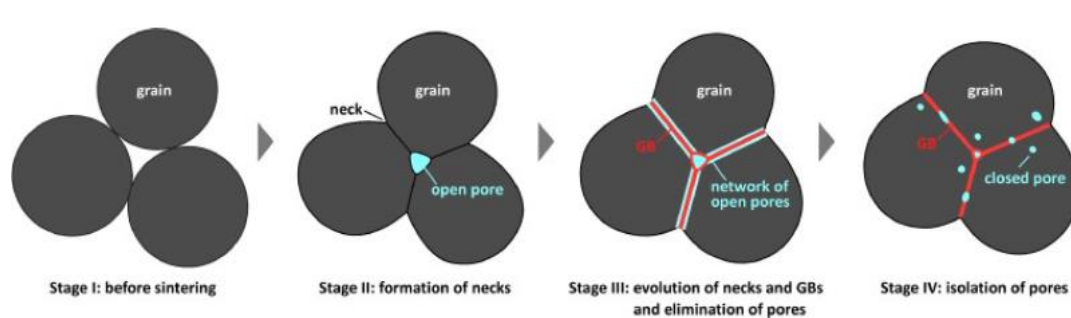


Figure 42 - Sintering stages of ceramics. (Khalil Abdelrazek Khalil (2012). *Advanced Sintering of Nano-Ceramic Materials, Ceramic Materials – Progress in Modern Ceramics*, Prof. Feng Shi (Ed.), ISBN: 978-953-51-0476-6, InTech)

#### 4.4 Thermal characterization of the formulations

The thermal analysis of the study includes the Differential Scanning Calorimetry (DSC) with the final task of collecting latent heat results and thermal heat capacities, and the Laser Flash Analysis (LFA) to obtain the thermal conductivity values, each one for the specific formulations.

##### 4.4.1 DSC results

The thermal characterization has been conducted by means of Differential Scanning Calorimetry by Mettler Toledo equipped with Star(E) II Plus software and run for the whole set of studied formulations S501, S505, S510, S701, S705 S710. As a starting point, pure materials have been tested, both the NaNO<sub>3</sub> and KNO<sub>3</sub> as well as the Solar Salt (60%NaNO<sub>3</sub> and 40%KNO<sub>3</sub>) in order to track the thermal property variations once the eutectic is formed. While the Solar Salt has been tested in the range between 25°C to 300°C, the Pure Salts have been tested for higher temperatures from 250°C to 400°C because 400°C is their degradation temperature and their melting transition occurs at higher temperatures compared to the eutectic mixture. In order to compare their results, the salts used for the formulations of the SSPCMs have been compared to higher quality-salts by Sigma Aldrich that are usually used for lab-scale experiments. Results have been proved to match with a variable error but they are consistent with values reported in literature shown in Table 7.

Table 7 - DSC tests on pure salts and Solar Salt.

DSC test	T <sub>m</sub> [°C]	ΔH <sub>m</sub> [kJ/kg]	T <sub>m</sub> [°C] (Reference)	ΔH <sub>m</sub> [kJ/kg]
NaNO <sub>3</sub> (Sigma Aldrich)	305.84±0.29	176.19±0.35	304.8 [56]	
NaNO <sub>3</sub> (other supplier)	305.92±0.21	169.02±1.01	306 [57][58]	182
KNO <sub>3</sub> (Sigma Aldrich)	331.25±0.11	92.59±0.19	336.35 [56]	
KNO <sub>3</sub> (other supplier)	326.75±0.13	92.16±0.54	334 [57]	100
Solar Salt	224.84±1.54	113.20±4.16	223.2 223	142.2 [59] 106 [60]

Specific heat measurements are also of fundamental importance when characterizing SSPMs. As already mentioned in Section 2.3, one of the main advantages of manufacturing these composites is to exploit the high sensible fraction due to the temperature increase and their relatively high specific heat and density. Specific heat capacity measurements have been performed by comparing with the signals of the heat flows between the well-known specific heat of sapphire material and the actual sample with the same temperature program. The equation applied by the instrument to estimate the specific heat is given by:

$$C_{ps} = \frac{H}{h} * \left( \frac{m_{ref}}{m_s} \right) * C_{pref}$$

Where H is the difference of the heat flow signal of the sample with respect to the reference empty pan and h is the difference between the sapphire sample and the same reference pan.

An example of the specific heat curve obtained by means of the Sapphire method is shown in Figure 43, where the specific heat peak corresponds to the melting phase, this is a high temperature-dependent property, this is why when evaluating the actual values for the specific case of the solid and liquid phase, the specific values corresponding to the peak should not be considered, in fact constant values for the solid and liquid temperature intervals are considered. A specific heat curves of the pure salts have also been tested giving consistent values when comparing the Sigma Aldrich to the other supplier products. For the thermal analysis of the formulations produced and explained in Section 4.2, the same program for the Solar Salts has been chosen. The program steps included:

- Isothermal step for 10 min at 25 °C;
- Heating step at 10 °C/min heating rate from 25 °C to 300°C
- Isothermal step for 10 min at 300 °C;

Due to multiple tests on the selected formulations and after varying test conditions the experiments have been optimized by using Pt crucibles which is inert with the salts to obtain a well-defined and sharp signal as well as other preparation steps have been refined. Mixing and grinding of the nitrates to reach the final same particle size allowed to facilitate the eutectic formation. Advancements compared to previous tests showed that the exact eutectic formation is fundamental to avoid double peaking in the DSC signals for the latent heat values and may suggest a more uniform dispersion of the salts from a composite point of view, allowing a full and more uniform exploitation of all the enthalpy of melting of the Solar Salt.

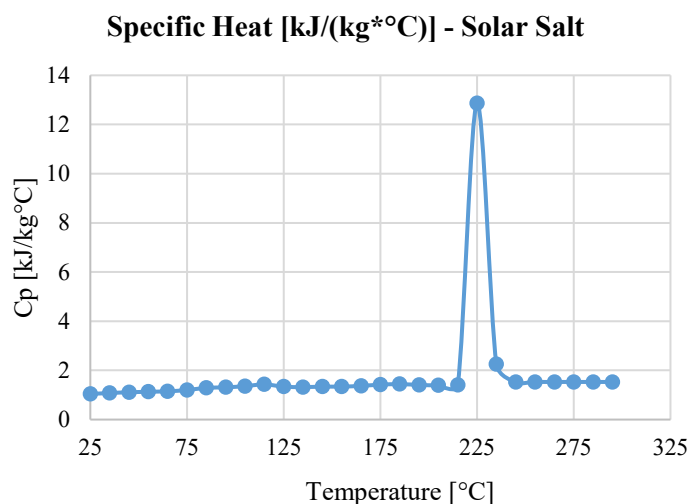


Figure 43 - Cp curve for Solar Salt measured by Mettler Toledo DSC by applying the Sapphire reference method.

Final results in Figure 44 show that the curves obtained show negative sign, this is due to the conventional positive value assigned when a process is exothermic. In this case in fact, the melting process is an endothermic one.

As expected, the higher latent heat has been registered for samples with 75% of (NaNO<sub>3</sub>, KNO<sub>3</sub>) eutectic content. The melting temperature remains in the range 220-230°C for the whole formulations set while latent heat values show a conservative behaviour according to the PCM contents in the formulations. According to DSC results sample with 55% content of the eutectic (namely S501, S505 and S510) show lower latent heat values, thus a lower overall energy density. Moreover, the latent heat values showed in the bar tab in Figure 45 are not affected by Graphite content, so that the curve trend changes slightly only because of the different contents of Vermiculite (and its high specific heat), this effect however does not affect the melting enthalpy values.

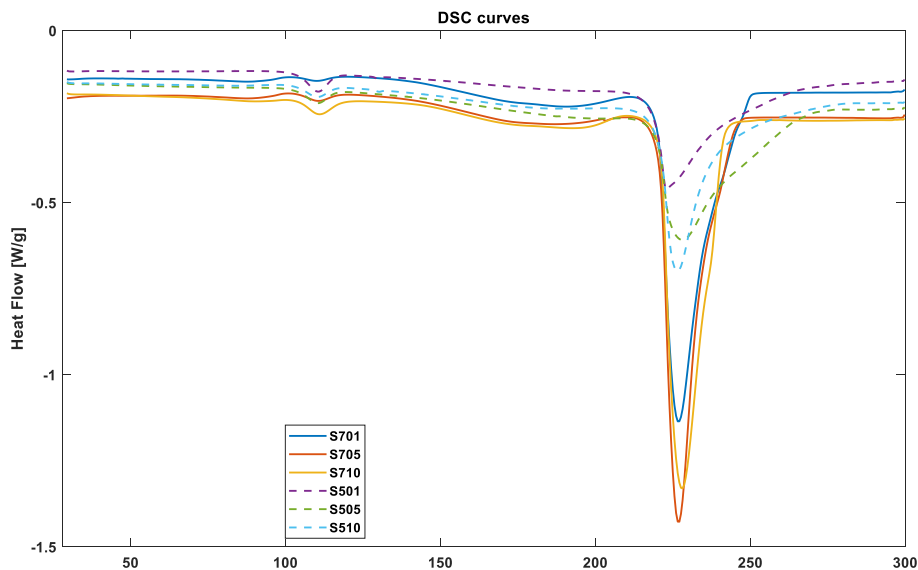


Figure 44 – DSC results for all the formulations tested. The plot references to the 55%-PCM and the 75%-PCM formulations.

In order to support the different results obtained for 55% and 75% Solar Salt content, a specific heat measurement was conducted by means of sapphire evaluation method through DSC. The resulting values shown in Table 8 have been evaluated by averaging the specific heat in the temperature range 100-200 °C while for the cp,liq has been evaluated in the range 250-300 °C. Results on energy densities from table 8 showed that thanks to the sharp melting interval occurring at a medium to high temperature along with the high energy density stored confirm the high potential of SSPCMs' formulations as possible TES solution for high energy storage requirements.

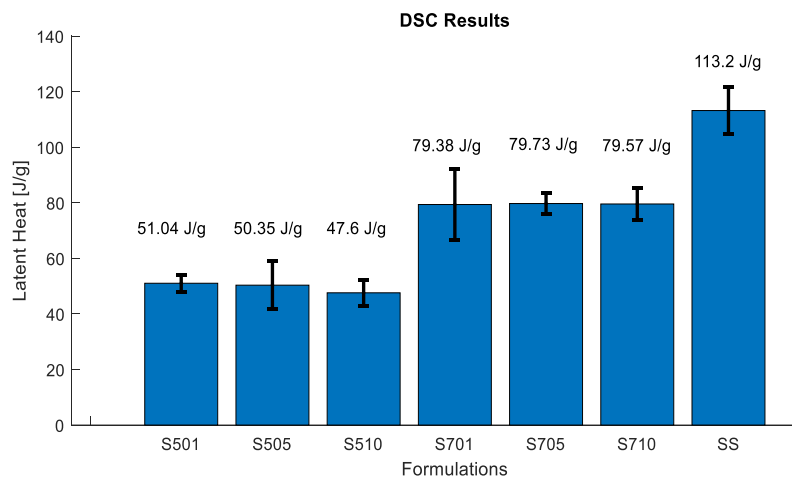


Figure 45 - Bar plot summarizing the latent heat values of different formulations compared with the Solar Salt one.

Table 8 - DSC summary results.

Formulations	T <sub>m</sub> [°C]	ΔH <sub>m</sub>	C <sub>p,s</sub>	C <sub>p,l</sub>	E <sub>d</sub>
		[kJ/kg]	[kJ/kg*°C]	[kJ/kg*°C]	[kJ/kg]
S501	223.24	51.04	1.03	1.27	217.36
S505	228.18	50.35	1.30	1.5	255.17
S510	226.3	47.6	1.29	1.55	254.17
S701	226.86	79.38	1.13	1.39	261.81
S705	225.83	79.73	1.43	1.68	307.18
S710	227.38	79.57	1.48	1.59	306.97

#### 4.4.2 LFA results

After the thermal evaluation of the six formulations by means of the DSC, as a route to the final evaluation and characterization of the optimal formulation, has been completed by means of thermal diffusivity measurements.

Even though the main purpose of the study is to find the optimal formulation with the highest energy density possible, as a tool to evaluate the overall thermal performance of all the formulations, both the set of samples with 55% and 75% of PCM content respectively have been tested with Laser Flash Analyser. Moreover, LFA allowed not only the complete thermal characterization of the considered formulations, but also proved to be a fundamental tool in showing graphite potential in thermal conductivity enhancement inside the pellets.

The tests have been conducted by manufacturing new 0.6 gr x 13 mm diameter pellets at 20 MPa pressure held for 1 minute. The final samples obtained after sintering had a thickness in the 1-2 mm range. The pellets have been adjusted on a sample carrier inside a tube-shaped furnace and shot by a short-duration light pulse. The smaller thickness of these pellets compared to the previous ones, justifies the assumptions of a uniform temperature distribution inside the sample (the internal resistance of the sample is smaller compared to the one towards the external) so that the heat transfer by conduction has more impact compared to the convection effect. However, as Parker et al's analysed, two non-neglecting contributions are produced during the tests consisting in heat losses occurring on the surface and thermal contact (interfacial) resistance between the light pulse and the specimen[43]. In order to reduce these effects both the choice of an appropriate mathematical model to apply is necessary as well as to improve absorption of heat and light a graphite spray thin layer has been applied on the whole surface of the sample. The Cowan method has been adopted in order to take into account also convection and radiation effects (non-neglecting phenomena at relatively high temperatures) which occur in proximity to the surface of the sample.

The thermal diffusivity has been tested at different temperatures from around 25°C, 100°C, 180°C, 250°C and 300°C and three shots have been applied for each temperature. The average results of the shots for each temperature for the whole set of samples are shown in Figures 46-47. Regardless the sample's PCM content, Figures 46-47 show the same behaviour throughout the set of 55% PCM as well as in the one with 75% PCM content, the thermal diffusivity values clearly decrease from the solid to the liquid state where the values tend to stabilize. A small difference in behaviour is tracked in sample S701 showing a slight increase in the thermal diffusivity value with respect to the usual trend of the other samples. After the LFA test sample S701 showed significant deformation (in some tests also cracking) along with leakage confirming the results showed from the heat treatment while manufacturing the pellets. As a consequence, results after the melting point at 220°C show not be taken into account because non-reliable due to breaking of one of the main

assumptions of homogeneity of the properties of the specimens, these results have been however showed for sake of completeness. However, the most important outcome of this analysis consists on a thermal diffusivity enhancement which can be tracked with the graphite content increase.

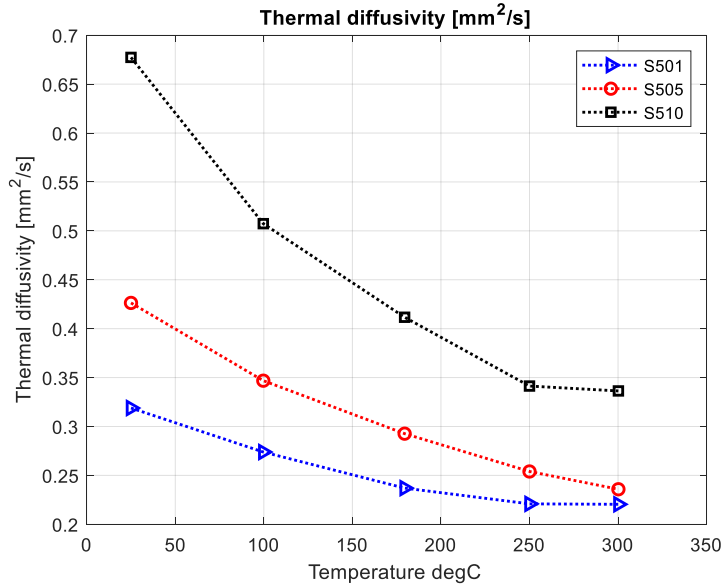


Figure 46 - Ref samples: S501-05-10 – 55% PCM content - Thermal diffusivity trend.

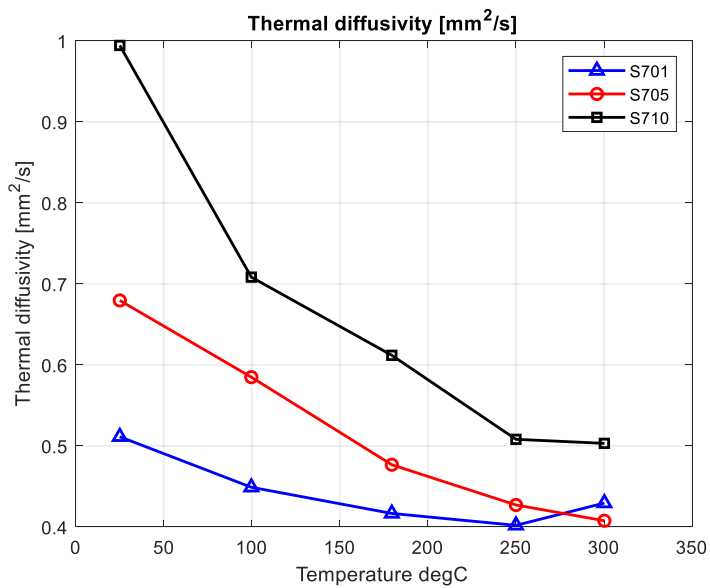


Figure 47 – S701-05-10 - 75% -PCM content - Thermal diffusivity trend.

The shifting towards higher values of the thermal diffusivity of the 75%-set compared to the 55% -set is mainly due to the dependency of the diffusivity to the density and specific heat values (and the thermal conductivity viceversa).

In order to evaluate the thermal conductivity of the samples the equation is applied:

$$\lambda(T) = a(T) * c_p(T) * \rho(T)$$

For a better visualization and conceptualization, results of the thermal conductivities have been shown by choosing an intermediate temperature in the range 25-300°C, specifically at 100°C. Figures 48-49 report the average values of thermal conductivity by considering the error bars referred to the standard deviation of the measurements amongst the 3 pulse shots performed for each temperature step.

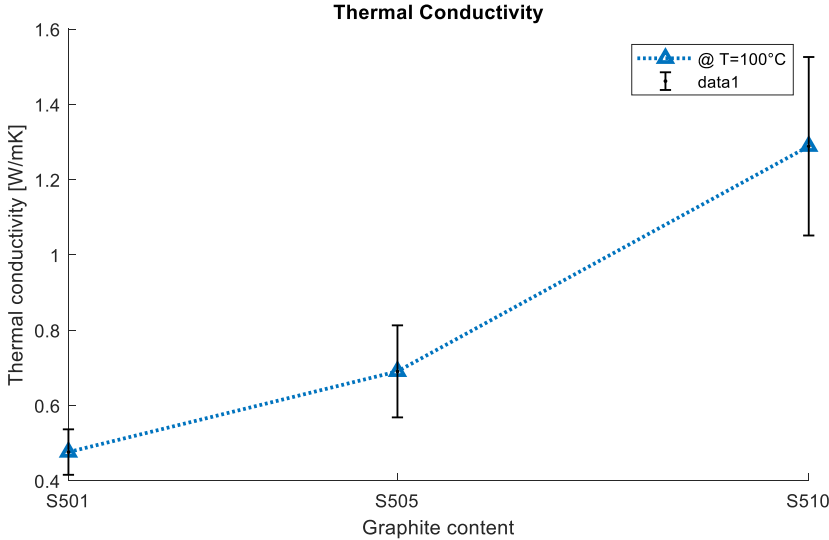


Figure 48 - Thermal conductivity values at 100°C for samples with 55% PCM content and increasing graphite content.

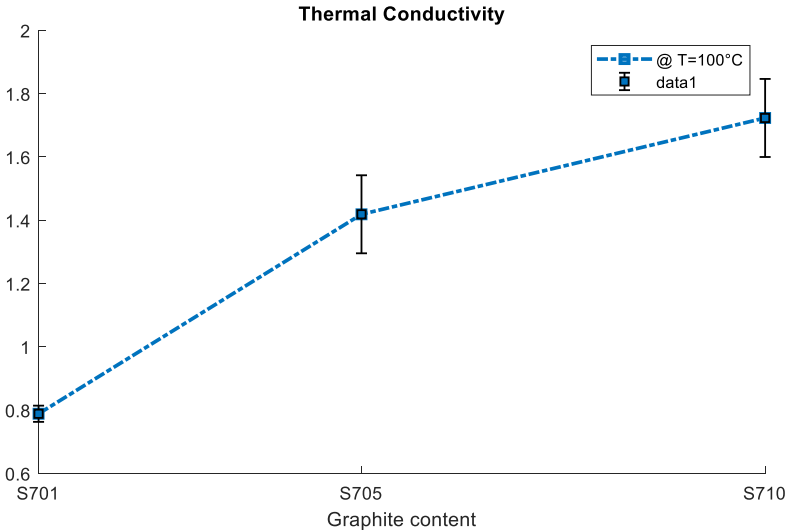


Figure 49 - Thermal conductivity values at 100°C for samples with 75% PCM content and increasing graphite content.

Thermal conductivity has shown significant increase in both set of samples proving that manufacturing composite pellets with carbon-based particles, whether in powder or other nano-structures, fosters thermal diffusion properties. At intermediate temperatures of 100°C thermal conductivity of graphite-dense composites (S510 and S710) showed an increase of

more than twice the values of nearly-zero graphite content samples (1% of graphite for S501 and S701).

As already mentioned in Section 2.1 and as widely recognised in literature, one of the renowned drawbacks of PCMs is connected to their low thermal conductivity. In Table 9 some values of the materials used for formulations and manufacturing of the SSPCM tables have been collected from literature. By comparing experimental results and referenced results from literature it is evident that the thermal conductivity of the formulations studied do not depend on Vermiculite which has the lowest value reported but depends mainly on the Graphite to PCM ratio. Additionally, samples S501 and S701 with nearly-zero graphite (only 1%) at 100°C cover a range of 0.42-0.82 W/(m\*°C) for thermal conductivities values, which are slightly higher than the Solar Salt reported in literature.

*Table 9 - Thermal conductivity of composite materials from peer-reviewed papers.*

<b>Materials</b>	<b>Thermal conductivity [W/(m*°C)]</b>	<b>References:</b>
Solar Salt	0.45±0.067	(Serrano-ópez, Fradera, & Cuesta-López, 2013)[61]
(60%NaNO <sub>3</sub> :40%KNO <sub>3</sub> )	0.52	(WU, LI, LU, Wang, & MA, 2017)[62]
Vermiculite	0.04-0.12	(Suvorov & Skurikhin, 2003)[63]
Graphite	25-470	(Formula, Covered, & Leaders, 2014)[64]

Thermal conductivity enhancement by means of carbon-based particles or microstructures is one of the most debated issues when dealing with composites at a micro-scale perspective but is one of the key parameter which can lead to overwhelmingly increased thermal performance at a device-scale. Even though Graphite contribution has nothing to do with latent heat potential of the SSPCM (the PCM is the only contributor to that), it has a great impact on gaining higher heat transfer rates allowing charging/discharging processes to reach the equilibrium temperature in less time. Thermal enhancement through the addition of carbon-based components/fibres/nanoparticles or Expanded Graphite/foams have been widely recognized in the composites experimental research [20,21,38,65–68].

In particular different studies proved high proportionality between the increase in volume fraction of carbon particles and thermal conductivity increase, where in some cases a linear relationship has been demonstrated [66] while according to some other studies the method through graphite particles have been integrated into the composites is relevant. Nomura et al's for instance conducted a study on a composite material made of Erythritol as PCM (thermal conductivity 0.73 W/m\*°C) mixed with carbon fibres as filler with the function of heat transfer enhancer material. This study highlights the importance of the creation of percolating Carbon Fiber network for the thermal performance of the composite by comparing in a detailed way two different kinds of fabrication methods of the samples. The first adopted is the traditional melting-dispersion MD, while the second is the hot-press HP method. In the MD method the carbon fillers are mixed into liquid form PCM (at 150 °C), while the latter is essentially a compression in solid phase of both PCM and carbon fibres. Results showed that thermal conductivity increased almost linearly with MD method while it showed an exponential behaviour with the HP method. In addition to this, a massive increase in the effective conductivity occurred onto the perpendicular plane the pressing direction reflecting its natural anisotropy. EDS and SEM methods showed indeed

different morphological structures for the two different fabrication methods and both showed, in different extent, the formation of random percolating pathways whose formation is fostered by HP method and high packing of PCM even at lower carbon fibres content. (Nomura, 2015) Exponential increase with graphite flakes for cold-compression techniques has been also tracked by Yunxiu et al's (Ca(NO<sub>3</sub>)<sub>2</sub>-NaNO<sub>3</sub>/expanded graphite composite).

As for different parameters assessed during the manufacturing procedure, different particle sizes of some materials in composites present different thermal conductivity values as for the changing and variability of the orientation and according to the nature of the substance considered. LFA analysis with the same test conditions mentioned previously, has been conducted also for different particle size of the Vermiculite for the S710 formulation (Figures 50-51).

According to the results obtained it is again proved the higher impact of 3 mm Vermiculite towards thermal conductivity enhancement while very little diffusivity values are detected for lower particle sizes. This may be connected to the higher probability of 3 mm Vermiculite to enhance creation of microstructures favouring the enhancement in the compression direction. Most of the studies conducted on variable size or shape are connected to the graphite, so that to track such anisotropic change in properties also the x-y direction should be tested with the LFA [66]. A turning point is however detected on 1 mm particle size suggesting that, once the PCM overcomes the melting point and is in its liquid phase, more compaction may further increase the thermal diffusivity. For what 0.25 mm size are concerned, the evenly mixed dispersion of graphite and Vermiculite is less likely to lead to enhancing microstructures.

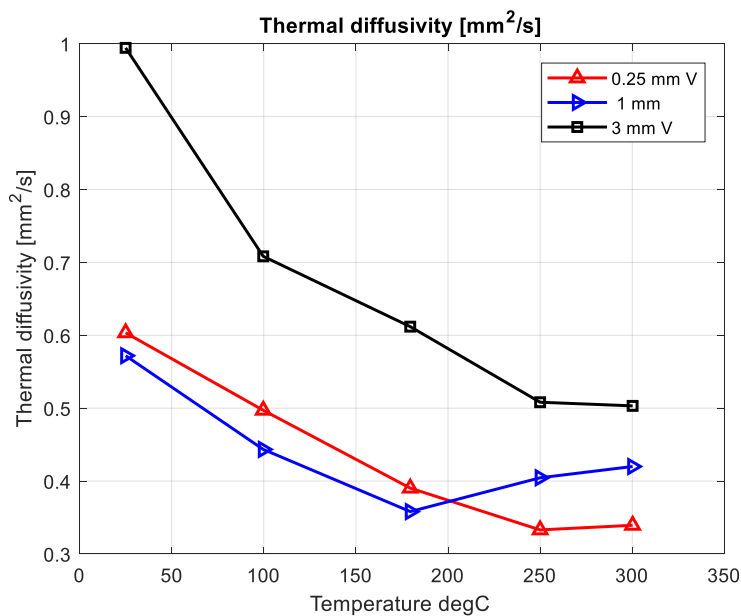


Figure 50 - Thermal diffusivity of Reference formulation S710 with different Vermiculite particle sizes.

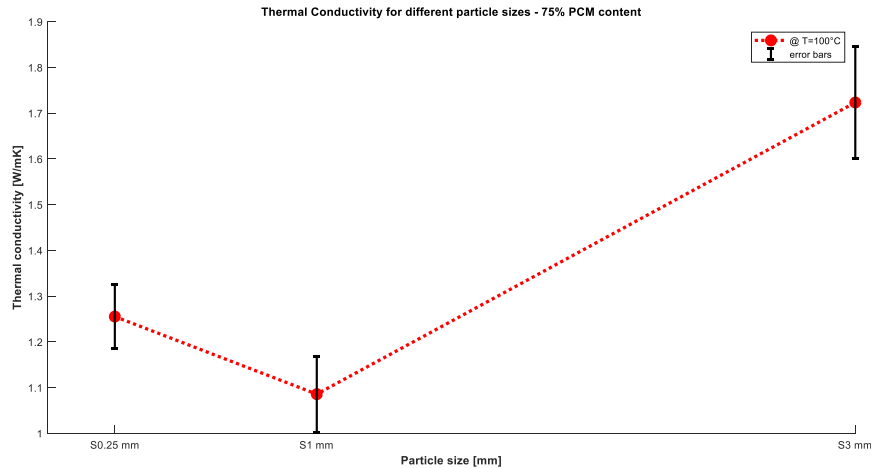


Figure 51 - Thermal diffusivity of Reference formulation S710 with different Vermiculite particle sizes @ 100°C.

#### 4.5 Dilatometry Analysis

As explained in Section 3.4, optical dilatometry consists on an experimental method allowing to determine the thermal expansion coefficient of a material or a composite by measuring its size variations when exposed to temperature change. In the specific case of the manufactured 13 mm diameter pellets, a LED source emits a parallel beam collecting information about the change in length of the diameter when the sample is invested by the beam. The tests have been conducted for the set of samples S701, S705 and S710 with the highest PCM contents (75% Solar Salt in the matrix). The selection of this subset is connected to practical testing timing issues but mainly because the samples chosen present higher thermal potential due to their higher latent heat thus energy densities. The subset will be considered the final set for the investigation of the micro-structural analysis.

The temperature program test to apply to the whole sub-set chosen, has been decided basing onto the range of the FPCM's composites maximum allowable temperature from ambient temperature. Specifically, the temperature test chosen is shown in Figure 52, on Figure 53 instead is an example of the test parameters involved in the analysis in a time-dependence scale to provide a clue on the response of the specimens' signals to the temperature program, in this case sample S701 has been taken as an example. For what the temperature program is concerned, the heating rate has been changed in the range of melting transition temperature at 220°C in order to tackle any additional micro-changes in volume variation. For all the tests conducted the cooling phase is beyond this analysis, so that it has not been taken into account for the discussion of the results. From Figure 53 is clearly shown a correspondence and a turning point (which is not so evident in temperature-dependent results) between the time-dependent length variation and the thermal expansion coefficient occurring from 40 min on. The temperature corresponding to 40 min corresponds to temperatures around 300°C suggesting that there is a change in behaviour after the melting point at 300°C.

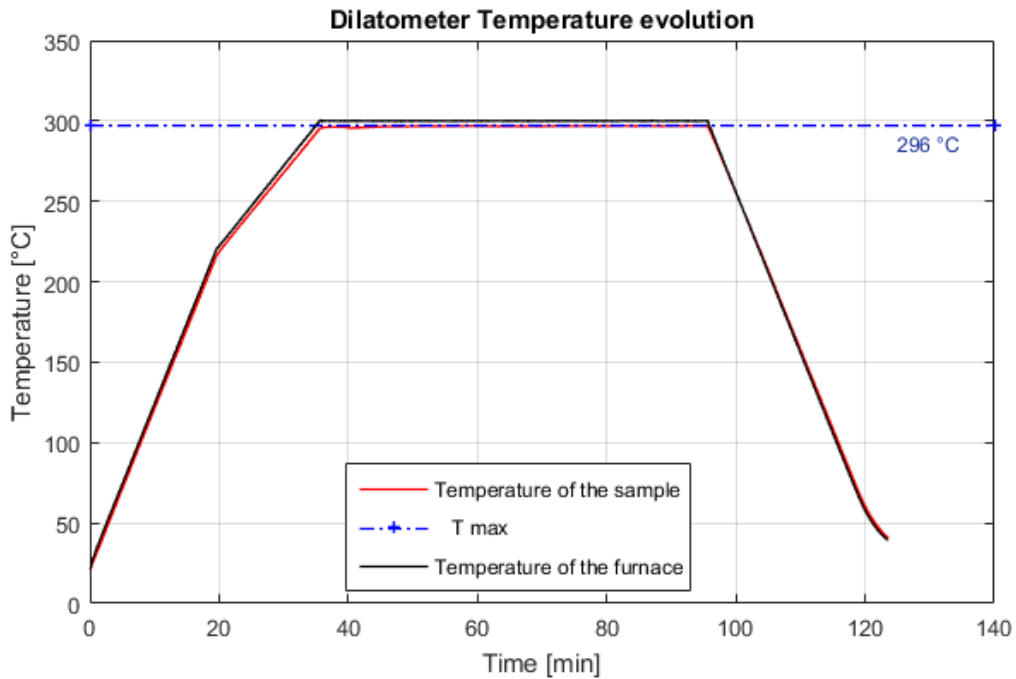


Figure 52 - Dilatometer Temperature test applied for the sample dilatometry tests.

Figure 53 also allows to track the miming behaviour of the change in length with respect to the temperature program, a slight shift of the signal is detected, this may be just due to the initial inertia of the furnace experiencing the temperature variation leading to a slight delay on the heating of the sample.

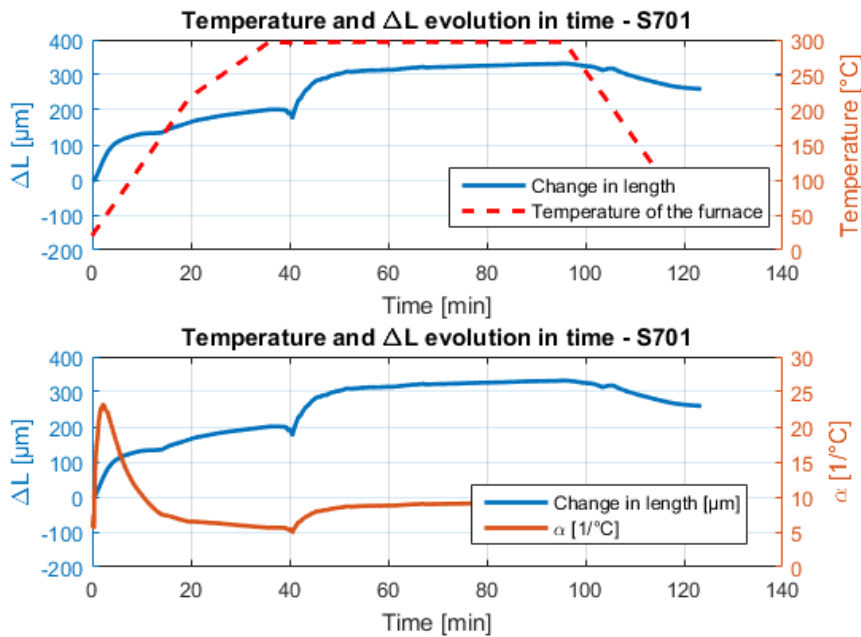


Figure 53 - Reference example of test on sample S701 to show time-dependent response of the specimens to the temperature test.

Temperature-dependent results from these tests have been post-processed on Matlab and are shown in Figures 54-56. In these plots the sole heating phase is shown, and comparison in the scale of variation of the three samples considered is possible.

As results show, sample S701 which has the highest content of Vermiculite experiences a higher and faster volume change which is detectable since from 40°C. This behaviour is also detected in sample S705 but decreases as the Vermiculite content decreases throughout the set of samples. In Figure 56 in fact, sample S710 shows a slower and more linear increase of the length variation of the diameter of the pellets. However, the final change in length reached around 300°C for all the samples is anyway in the range 150-200 µm. These evidences may suggest that while the higher content of Vermiculite enhances the volume changes, the higher graphite content might, on the other side, contrast this effect. For what the thermal coefficient results are concerned, Figures show, in the same way of the change in length, a proportional decrease of the thermal coefficient with the decrease of Vermiculite content in the samples. While on sample S710 (15% Vermiculite) the thermal coefficient stays stable in the range 0-50 x10<sup>-6</sup> [1/°C], sample S705 (20% Vermiculite) but especially sample S701 (24% Vermiculite) experience a sudden increase of such coefficient reported in the first 50°C temperature increase.

Eventually the dilatometry analysis allows to provide additional insights of what the heat treatment obtained by the sintering of the pellets already but only visually showed. The sample S701 had already reported to be more prone to swelling compared to the more shape-stable S710. In all the samples, the main thermal coefficient change is tracked in the first heating step up to 50°C with a peak registered for S710 around 240 x 10<sup>-6</sup> [1/°C] but stabilizing afterwards when reaching 300°C suggesting that overall the all composites formulations allow a controllable and contained volume expansion, this clue is fundamental whether the pellets should be scaled up and thought in a device scale application. This consideration provides added value to the fabrication procedure (sintering) adopted for the more shape-stable pellets (those with formulations in between S705 and S710 when also leakage issues are more controlled).

Limitations on this testing method when analysing temperature-dependent properties variation, consist on the evaluation of a single direction ( diameter dimension) due to the parallel investing beam of the LED source but not on the height point of view, the main assumption which has been considered for this method is that the thermal behaviour and properties are isotropic, but of course this is just a simplifying hypothesis when dealing with smaller specimens (maximum mm scale) which has to be taken carefully into account when manufacturing bigger pellets.

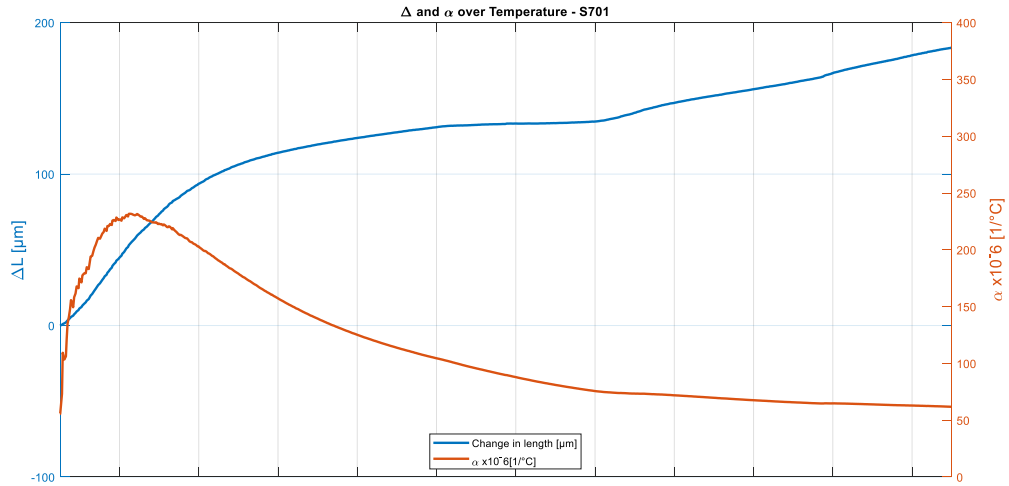


Figure 54 - Dilatometry Test - Temperature-dependent results of sample S705 (75% Solar Salt, 5% Graphite, 24% Vermiculite).

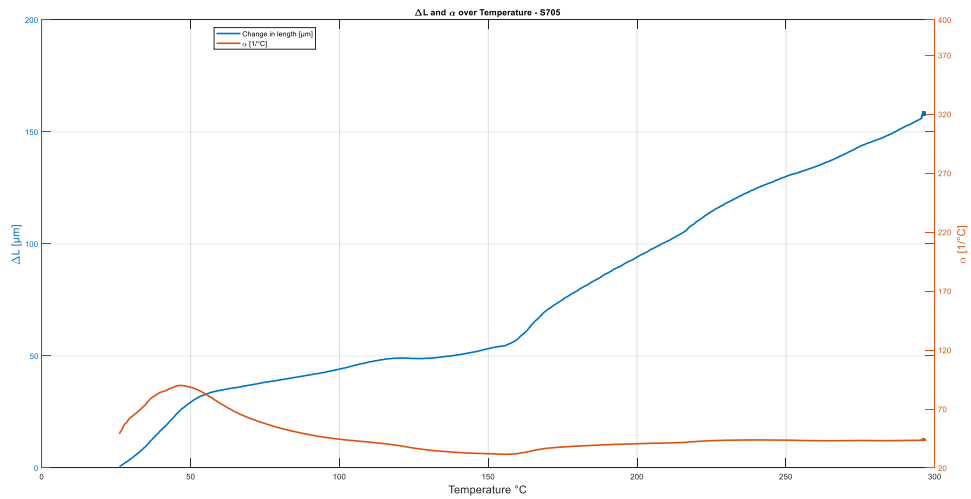


Figure 55 - Dilatometry Test - Temperature-dependent results of sample S705 (75% Solar Salt, 1% Graphite, 15% Vermiculite).

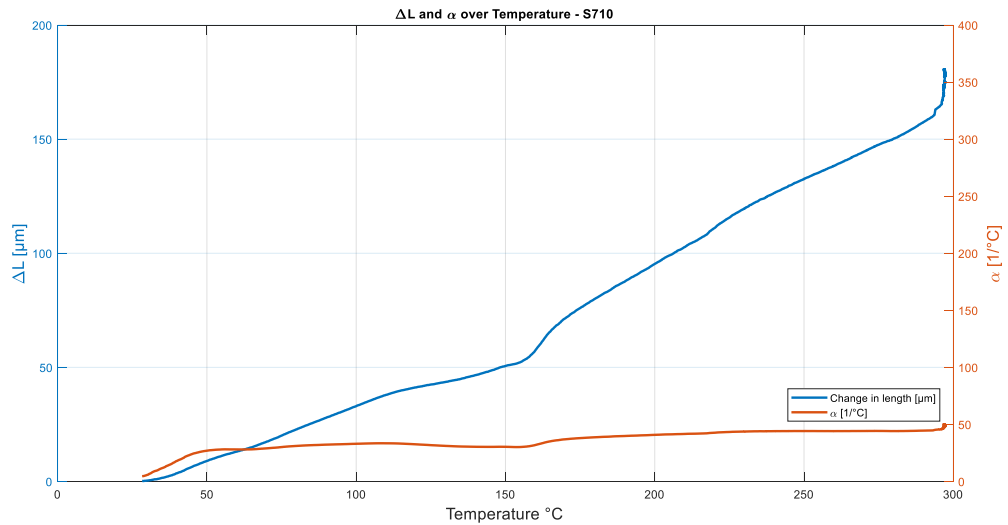


Figure 56 - Dilatometry Test - Temperature-dependent results of sample S710 (75% Solar Salt, 10% Graphite, 20% Vermiculite).

## 4.6 Complementary micro-structural analysis

The investigation of SSPCM microstructure to track the relationships between structure properties, thermo-physical properties and overall performance of the material has been carried out by multi-method approach by employing complementary Scanning Electron Microscope (SEM) and Energy-dispersive X-ray spectroscopy (EDX) in a multi-scale approach for semi-quantitative two-dimensional analysis of structure and elemental composition. An independent micro-structural cross-analysis developed by means of X-Ray micro-tomography and parallel digital image post-processing allowed to further quantitatively characterize the specimens.

### 4.6.1 SEM/EDX results for morphology assessment

As explained in Section 3.4, SEM/EDX analysis captures scattered and back-scattered electrons (SE and BSE respectively) resulting from the interactions between an accelerated-electron beam and the surface excited electrons of the atoms constituting the sample analysed.

The samples considered for the morphological and topological analysis are the final set of 75%-PCM content samples, namely S701, S705 and S710. The samples have been analysed with different magnification to visualize the differences up to a nano-scale.

From a first look at 40x zooming micrographs in Figure 57-(a),(b) and (c) the samples show that their morphological features change progressively according to the increase of the graphite content. Sample S701 shows a more-cracked micro-structure with apparently no presence of graphite, it is only 1% and dispersed into the matrix and difficult to track. On the other hand, samples S705 and S710 show darker and lighter regions correspondent to graphite and vermiculite regions all over the surface scanned. Moreover, the increased graphite content shows a more evident vein-patterned structure correspondent to the multi-phase Vermiculite-Salt-Carbon topology. A detail of S710 is shown in Figure 57-(e) highlighting the vein and stripes texture of the higher graphite content sample. Despite some polishing residuals detectable in Figure 57-((a)-(c)), 40x magnification micrographs show an apparent similar porosity for the whole set of samples. At this stage of the analysis, quantification of such property is not possible by means of SEM/EDX, further experimental techniques are required for this purpose.

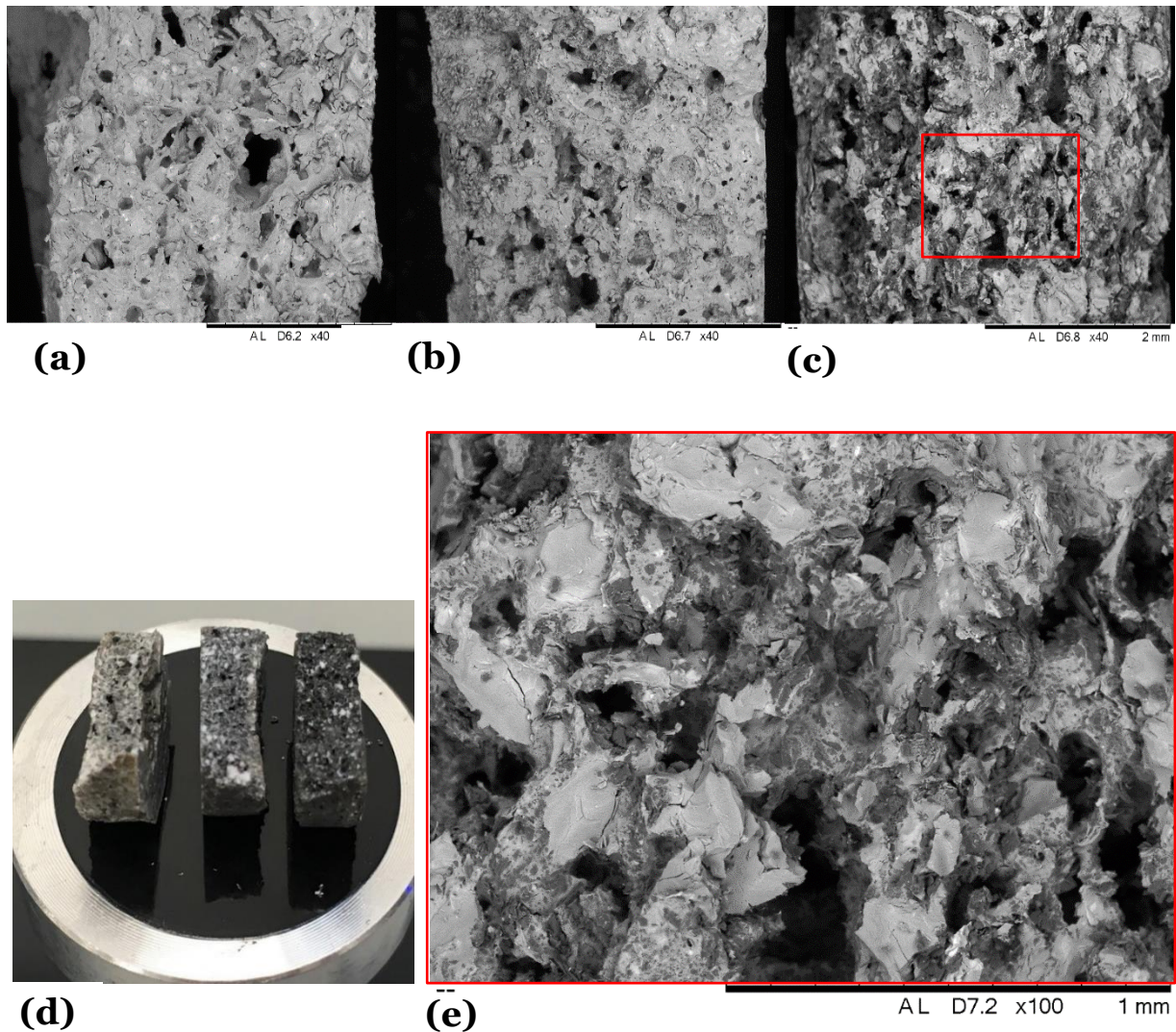


Figure 57 - SEM micrographs of: (a) S701, (b) S705, (c) S710 at 40x zoom. (d) Samples positioned on the stage, before polishing. (e) Detail of S710 100x zoom.

The most significant results which allow a more detailed visualization of the morphology of such specimens are those of the SEM micrographs in Figure 58-((a)-(c)) relative to S701, S705 and S710 samples as well as from the EDX mapping (Figure 58-((e)-(j))) where the distributions of potassium (K), sodium (Na), carbon (C) and silicon (Si) are depicted. The images were taken along a vertical cross section of SSPCM tablets (Figure 58-(d)) and the analysis was limited to SSPCMs with 75% of Solar Salt content. A closer look at the SEM micrographs of Fig. 58 shows that defects, such as cracks and voids progressively disappear as the graphite content increases within the SSPCM material. Stripes of Vermiculite (high content of Si) are clearly present in S710, surrounding and supporting the PCM (salts) in the composite, this is proved by the corresponding EDX maps. Similarly, but to a less extent, patches of C<sub>g</sub> aligned in strip-like structures gather in the proximity of Vermiculite, providing further structural support to the Solar Salt in the composite. On the contrary, S701 and S705 present distinct clusters of salt and vermiculite, which appears to promote the formation of cracks and leakage of PCM. This also suggest that the Solar Salt has a good compatibility and dispersibility toward the vermiculite matrix, being spread throughout the

two-dimensional surface. The liquid PCM flows preferentially toward the smaller grains and space of the vermiculite. Meanwhile, capillary forces between liquid Solar Salt and porous vermiculite contributes to the rearrangement and compactification of the SSPCM, preventing leakage [38,41].

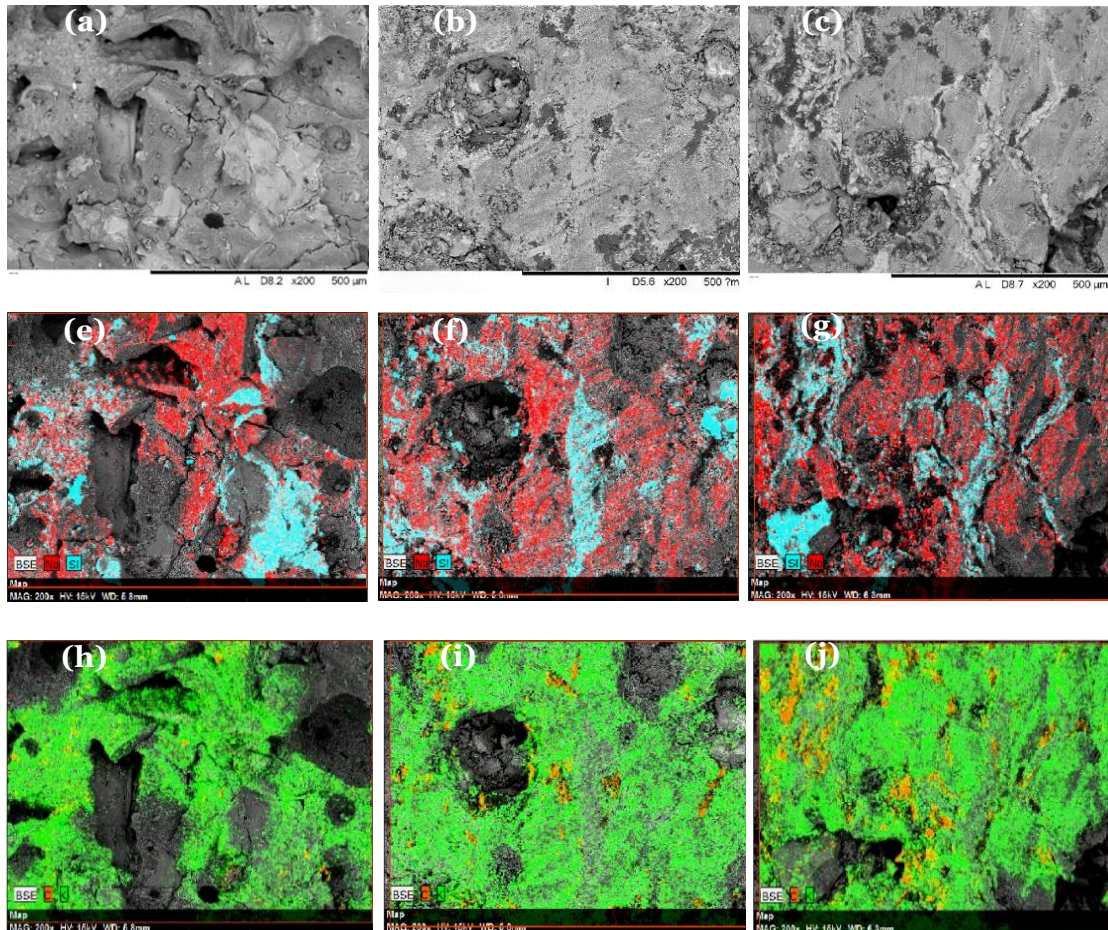


Figure 58 – 200x magnification of: (a) SEM, (e), (h) EDX for sample S701; (b) SEM, (f), (i) EDX for sample S705; (c) SEM, (g), (j) EDX for sample S710;

Ge et al's explained the occurring phenomenon as a consequence of the competing existing mechanisms of swelling and densification processes taking place because of graphite and vermiculite respectively. The two processes occurring independently are shown in Figures 59-(b)-(a) and directly connect with the nature of the method adopted for the manufacturing of the pellets. Powder-like elements mix and are compacted in the same way in the direction of pressing, the heat treatment then pushes to a multiphase state above the melting point where a rearrangement occurs. The final rearranged structure is an internal re-distribution of the elements constituting the formulation with a preferential organization of carbon-particles on the outer surface of the molten salt because of their poor wettability and a densification of the salt-supporting material structure. This is due to the ceramics' high wettability, thus high surface energies which keep the salt trapped inside ( as shown in Figure 57-(d)) providing local rigidity to the structure in a final reinforced overall structure. [38]

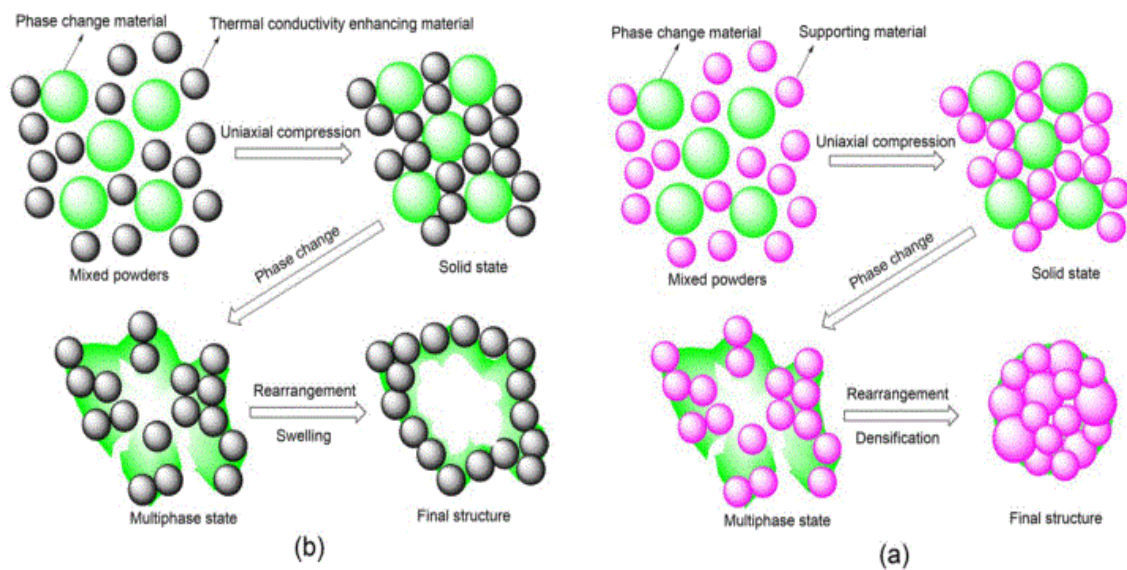


Figure 59 - Swelling of Graphite, densification of Vermiculite [38].

In conclusion, the SEM not only provides a deeper understanding of the actual topology and morphology of the materials constituting the composites obtained after the first heat treatment, but it gives a fundamental credit to the manufacturing procedure explained in Section 3, especially for what the sintering process is concerned. The heat treatment plays in fact the most important role in the fabrication of a shape-stable compressed structure of originally powder-like materials as well as for creating the minimum porosity which allows an even dispersion of the liquid PCM during cycles and a controllable volume variation. The densified skeletonized structure is indeed a result of the bending effect of solidified salt. It is evident that this multi-porous multi-phase microstructure could prevent PCM from leaking, clues suggests that also graphite may take actively part in the holding ability of the created microstructures. The presence of carbon-based component with low wettability which surrounds the salt may increase the PCM probability to be trapped inside pocket-like vermiculite-graphite structures not facilitating the salt leakage (as shown in Figures 57-(d) and 58-(c),(g),(j)). In support to this theory Figure 60 shows the reconstruction of the elemental spectrum of each component according to (Na, K, C and Si) for a 300x magnification of samples S710 which has 10% content of Graphite. The spectra have been obtained from the post-processing of the values of the energy values of the X-Rays collected by the detector in terms of wavelengths of each single element over a line width of roughly 500  $\mu\text{m}$ . From the reconstruction is evident that the spectrum of the Carbonium, being a highly-conductive element, corresponds to higher energy levels for its backscattered electrons over the total energy of the BE. This higher intensity is visible in more localized spots compared to Na and K which are more evenly distributed.

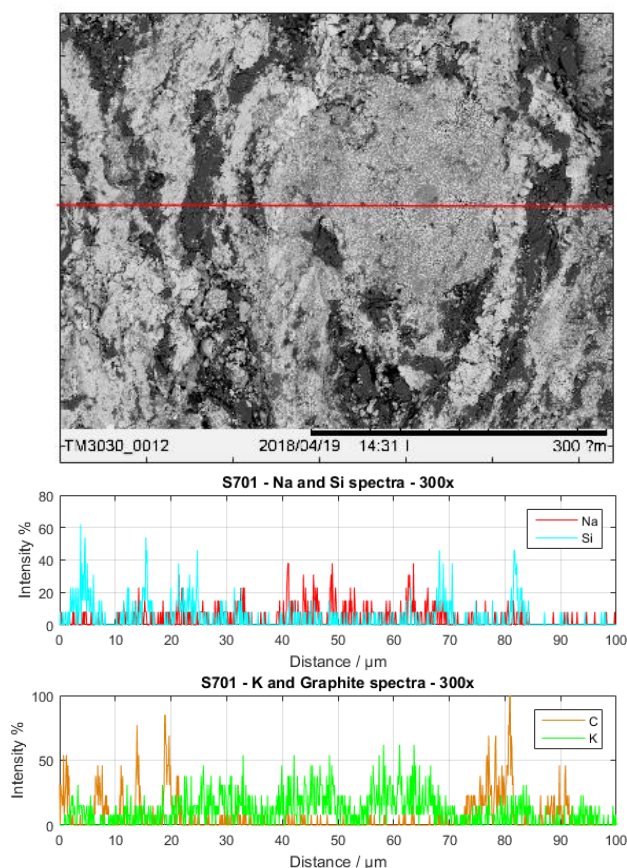


Figure 60 - Spectra reconstruction based on elemental composition of a 300x magnification of sample S701.

#### 4.6.2 X-Ray computed micro-Tomography results and Volume reconstruction

In order to deeply investigate the structural properties of the sintered pellets and to evaluate which are the most impacting parameters connected to leakage, a microstructural analysis has been conducted taking advantage of X-Ray micro-tomography and Digital Imaging techniques to comparatively estimate those properties throughout a set of samples. As for the SEM/EDX techniques, the subset of samples S701, S705 and S710 has been considered because of their highest PCM content (75% Solar Salt), thus higher energy densities.

Despite the poor shape-stability of sample S701 resulted from the failure of the leaking test, and its non-negligible irregular thermal expansion, it has also been tested with XRT to make a full comparison with the other better performing pellets (S705 and S710) as a relevant tool to discuss the differences within.

The complementary adoption of the X-Ray scanning, reconstruction and post-analysis software have not only allowed to quantify micro-structural properties but also to obtain a volume reconstruction and to tackle the structural evolution layer by layer with the aid of a Volume of Interest (VOI) selection. The VOI is a reduced 3D domain allowing to include into the study only the relevant areas or to eliminate defects resulting from the acquisition phase or excessive irregularities which may lead to a non-representative volume or overestimated values of porosities (e.g. a VOI including only a large pore area). Parameters

of interest which can be extracted from the post-processing analysis of the digital images are 2D areal porosity, 3D open and closed porosity, pore size distributions and many other information about the pores displaced throughout the sample area. The post-processing allows also a volume rendering from the dataset, an example for sample S701 is provided in Figure 61, where the evolution of the most emblematic failing sample from bottom to top layer is presented. These pictures provide an insight of what happens in a highly porous PCM-based and non-shape-stable composite after sintering when leakage occurs. To have a visual proof of the comparison among the samples, two different layers for each sample are shown in Figures 62: (a)-(f), one corresponding to the upper layers and the other slice corresponding to the bottom layers.

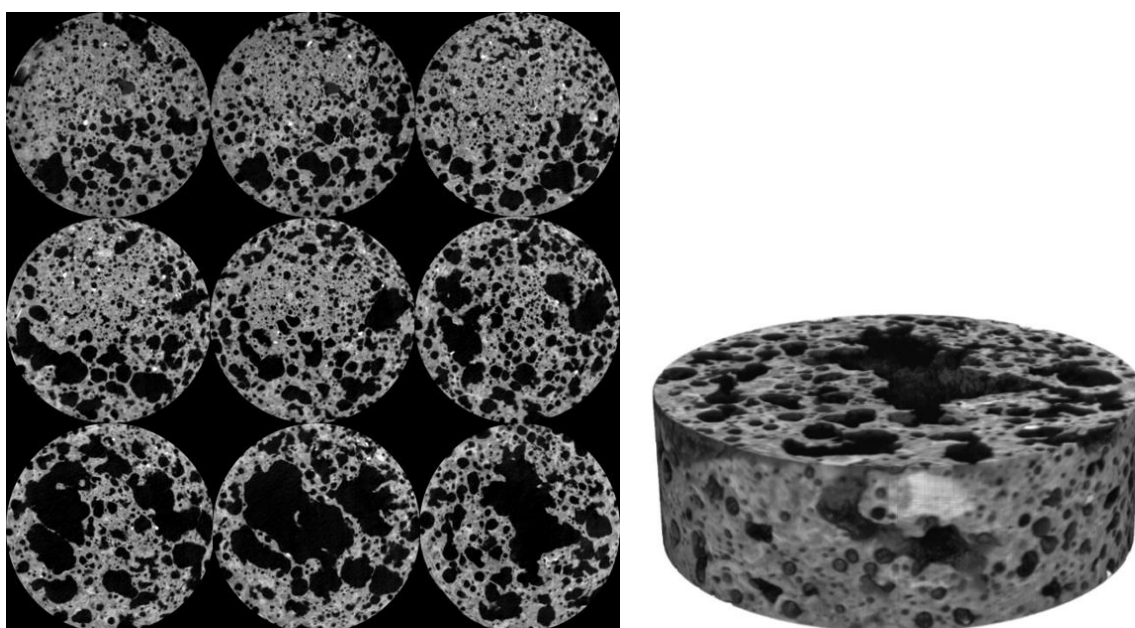


*Figure 61 - Volume reconstruction (right) of the source dataset (left) of sample S701. The dataset is not complete but represent the evolution of the 2D slices from bottom to top layers of the sample referenced.*

While from Figures 62-(a),(d), referring to the failing sample S701, there is a great difference in the distribution and entity of pore structures between a bottom and an upper layer, for samples S705 and S710 instead the porosity is more evenly distributed with no apparent distinction between one slice and the other. Figures 62 provide starting hints on how the leaking mechanism and the moulding effect of salt might have contributed to the creation of a porous matrix structure. The main advantage of the micro-tomography method relies on the possibility to obtain 3D results by collecting information in the sub-millimetre range which are representative of the whole sintered sample, however, it is highly dependent on the quality of the acquisition of the images and the selection of a proper and representative (VOI). Moreover, the quantitative analysis is based onto mathematical operations on binary digital images, so that also the choice of the most suitable thresholding method for segmentation of the output greyscale images is fundamental. Several tests run with different threshold limits may present a change in the calculated porosity of around 8-10% while a different VOI selection may lead to changes more than 20% in porosity registered from different tests for the same sample and in the same testing conditions. 3D results shown in

Table 10 are the final more relevant achievements obtained through this non-destructive technique.

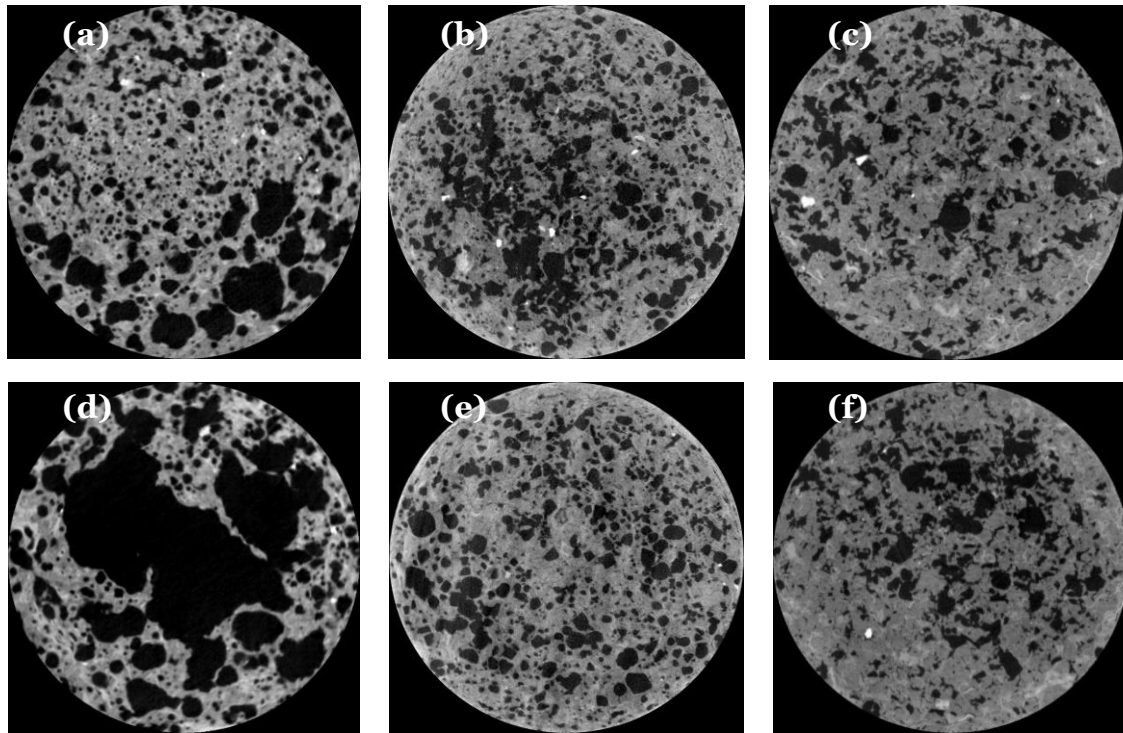


Figure 62 -- X-Ray micro-tomography digital images, (a) S701 at 1.31 mm height; (b) S705 at 2.04 mm; (c) S710 at 1.61 mm; (d) S701 at 4.75 mm; (e) S705 at 4.17 mm; (f) S710 at 2.78 mm.

Table 10 - Partial and most significant set of three-dimensional results obtained by the tomograph and post-processing softwares.

<b>3D XRT Results:</b>	<b>S701</b>	<b>S705</b>	<b>S710</b>	<b>U.M.</b>
Lower grey threshold	90	76	57	
Upper grey threshold	255	255	255	
Total VOI volume	119.00	343.54	216.30	mm <sup>3</sup>
Object volume	71.90	235.47	166.99	mm <sup>3</sup>
Percent object volume	60.50	68.54	77.20	%
Number of objects	30	3725	4643	
Number of closed pores	1331	5907	6726	
Closed porosity %	2.56	4.67	0.76	%
Open porosity (percent)	37.90	28.10	22.21	%
Total volume of pore space	46.90	108.07	49.31	mm <sup>3</sup>
Total porosity (percent)	39.50	31.46	22.80	%

As expected, the higher porosity is registered for sample S701 where the melting salt, being leaked from the host matrix, is collected at the bottom of the pellets leaving a large void space in the central area, this theory is visually confirmed by Figures 61 and 62-(a)-(d). In Table 10 is also shown the reference threshold limits used for the segmentation after the

acquisition phase, different limits for thresholding have been tested with a trial and error approach are a consequence of different acquisition qualities obtained after every test. For the three-dimensional analysis, a quantitative sense of the representativeness of the results as for the specific VOI selection is given by the Percent object volume corresponding to the ratio of volume considered and the amount of skeletal structure of that specific portion selected (which is considered as the object volume). The innovation and benefit of such technique in the three-dimensional setting is the capability of distinguishing the closed and open porosity values and their contribution to the total porosity.

Overall, from Table 10 is evident that the failing sample S701 have higher porosity compared to the more shape-stabilized S705 and S710, this stands for voids created as a consequence of the leaked salt from the matrix and may suggest the existence of a correlation between porosity and leakage of the PCM due to fluid-mechanical issues, higher amounts of voids as pockets or interconnected passageways clearly foster leakage. Porosity values are anyway in the range 30-20 %, not far from what has been calculated from measured density data from the Helium pycnometer detailed in Section 4.3. Discrepancies mainly related to the porosity of S701 are connected with the irregular structure of this pellet created after sintering, when the pellet has greatly deformed and leaked. The leakage is believed then to be a direct consequence of the internal presence of interconnected pathways.

On the other hand, as for the two-dimensional analysis, the most significant results connected to the porosity evaluation, are the porosity distributions along the sample width VOI selection, these are shown in Figures 63-65 where the sample-holder has a height equal to 7 mm. As for the distributions, the porosity considered is the open porosity due to its higher impact from the three-dimensional point of view. Total porosity values are collected from the 2D-image dataset and plotted to make a comparison within the three formulations of the set and to have an idea of the average porosity value and irregularity present throughout the sample width.

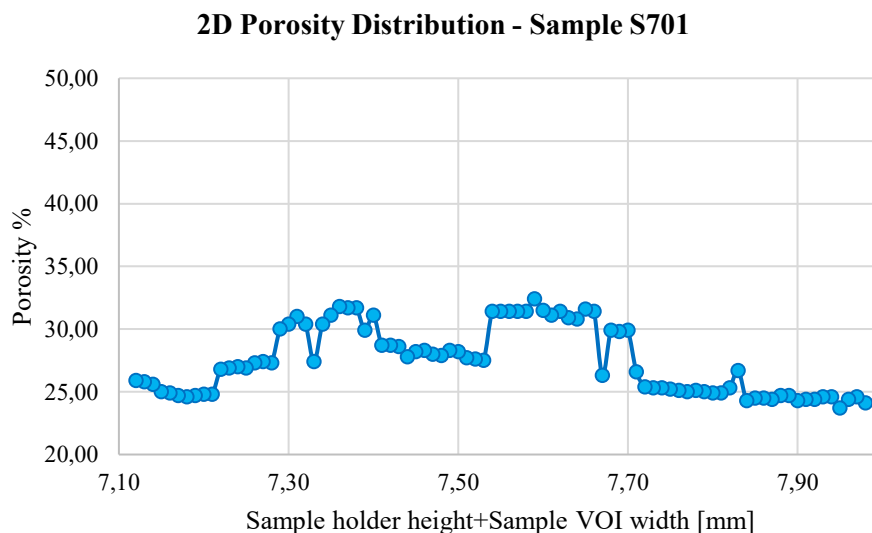


Figure 63 - Sample S701 porosity distribution across the sample width selected through the VOI.

### 2D Porosity Distribution - Sample S705

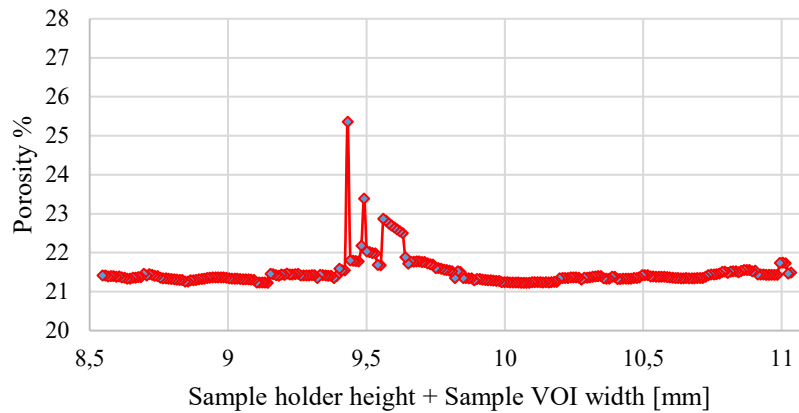


Figure 64 - Sample S705 porosity distribution across the VOI sample width selected through the VOI.

### 2D Porosity Distribution - Sample S710

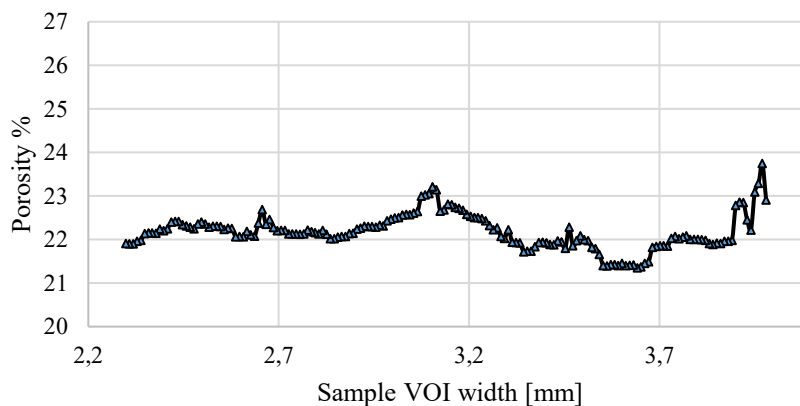


Figure 65 - Sample S710 porosity distribution across the VOI sample width selected through the VOI.

Despite the different VOI selection, Figures 63-65 corresponding to the more shape-stable samples, show a similar average porosity trend fluctuating around 22% with values not higher than 25%, only a small irregularity is detected around half of the sample width for sample S705. On the contrary, sample S701 presents a porosity distribution on a different scale with higher porosity values in the range 24-33%. However, when compared to total 3D porosities, the presented distributions are not totally representative of the total porosity of the samples. For this reason and to calculate in a more straightforward way the total porosity by means of external tools, another complementary technique has been developed to test and verify the results showed in this section.

### 4.6.3 Digital Image post-processing results

This section will deal with a comparative structural analysis which may be useful to be compared directly to some of the two-dimensional results of the tomograph and in some extent to have a feeling of the representativeness of those results with respect to the 3D ones obtained with the XRT.

The idea of developing such imaging techniques on Matlab has started from the need of producing more controllable results to possibly reproduce and validate the results provided from the microtomography. Main logical steps of the developed routine are listed in a comprehensive way in Section 3.

Amongst the large set of data produced, for a better visualization, a qualitative description and representative results obtained from the procedure proposed takes into account only some reference slices of a defined Region of Interest (ROI) for every pellet. According to the procedure adopted, an in-depth object by object analysis for the estimation of the porosity has been produced and lastly the study has been completed by a tortuosity evaluation on the coronal sections of the X-Ray scanned images of the specific samples. The decision of analysing also some reference coronal sections can be considered as an alternative way to address a three-dimensional study and possibly track the presence of pathways inside the pellet matrix. Preliminary results from in Table 11 show that, despite the higher number of pores in well-performing samples S705 and S710, higher values of porosity are reached for the S701 layers suggesting that there might be a correlation among leakage and porosity values, whose results are supported by the detection of higher total area and average equivalent radius  $R_{ave}$  of pores in S701 compared to the other pellets. Results similarly match with both porosimetry by means of the Pycnometer and 2D and 3D results from the XRT analysis.

It must be underlined that results in Table 11 are only some representative slice samples, as shown from the tomograph, the porosity is irregularly distributed throughout the VOI width, as a consequence, a pore radius distribution may provide more detailed insights of the features of these pores and are shown in Figures 66-68. However, despite being non-totally representative, Table 11 provides details on the average radius of the pores tackled in each single slice and the total and maximum pore areas, which have higher values for S701 and lower for S710.

*Table 11 - Summary of some 2D slices results from Digital image post-processing developed on Matlab.*

Sample	Height [mm]	$N_{pores}$	$\epsilon_{2D}$ %	$R_{ave}$ [mm]	$A_{TOT, pores}$ [mm <sup>2</sup> ]	$A_{pore,max}$ [mm <sup>2</sup> ]	Av. Stretch %
S701	1.31	599	39.53	0.100	54.29	11.99	81.59
S705	4.17	936	28.88	0.071	39.30	2.29	77.80
S710	1.61	732	22.47	0.064	28.88	1.98	73.37

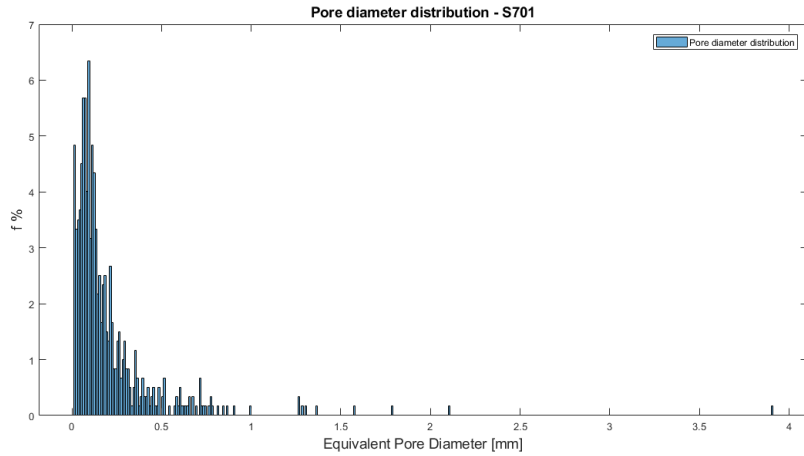


Figure 66 - Pore equivalent diameter distribution for a slice of sample S701.

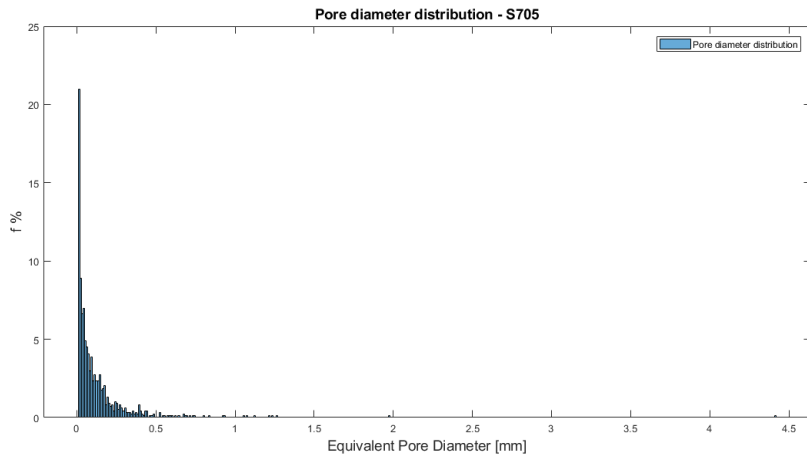


Figure 67 - Pore equivalent diameter distribution for a slice of sample S705.

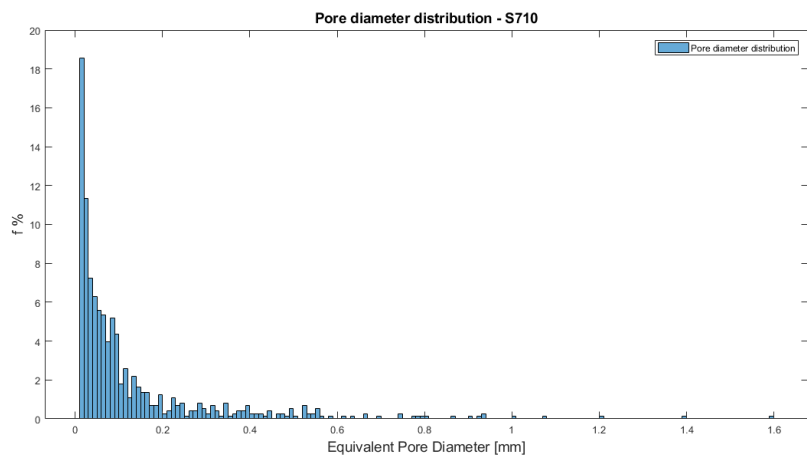


Figure 68 - Pore equivalent diameter distribution for a slice of sample S710.

Samples S705 and S710 show a frequency around 20% for pore diameters more evenly distributed in the range 0-0.5 mm and compared to S701 with a frequency of nearly 7%. Sample S710 has however a more evenly distributed 2D structure from a pore size point of

view showing less than 1% probability of pore size around 1.6 mm compared to values of around 4 mm of diameters for S705 and S710.

In order to find a connection between pores and network-shaped microstructures Table 11 shows also a parameter called pore stretching which gives an idea of how the pores are stretched with respect to their equivalent pore diameter, taking as a reference a circle shape for the pore objects. This parameter has been calculated for each pore object as follows:

$$\pi_{pore} = \left( \frac{L_{max}}{D_{eq}} \right)^{-1}$$

Where  $L_{max}$  is the major axis length of each pore without considering the orientation or a preferential direction and  $D_{eq}$  is the equivalent diameter of the pore. This parameter refers to the likelihood of elongated pores to be considered as pathways and can be collected both from cross-sectional and coronal surfaces.

According to this parameter, objects with pore stretching values near to 1 are more rounded pores and are less likely to be considered as pathways for the subsequent tortuosity analysis. On the other hand, pore stretching values near to 0 are more elongated pores, or interconnected pores. Results show that the average pore stretching ranges around 80-70 % for all the samples underlining that pores can actually be considered as network-shaped microstructures. Higher values for S701 may suggest however that a larger amount of elongated pores can be more prone to be considered as interconnected pathways in sample S701. Additional single-parameters can be selected and computed as shape descriptors in order to achieve the task of classifying objects for an overall characterization of the samples. [47]

Regardless the y direction (from top to bottom layers) being the preferential direction for the melting salt flowing during phase transition and eventually leading to leakage, the pore and pathways formation has no preferential direction resulting in a general structural anisotropy of the samples. According to this, even if the procedure can be applied on both coronal and x-y cross-section surfaces of the specimens. When applied to coronal section an additional parameter more connected to pathways formation can be estimated. Tortuosity has been calculated for this purpose and the results of the porosity and tortuosity analysis results from coronal sections have only been shown in Table 12.

The driving assumption for the tortuosity analysis to be set is related to the main hypothesis that pathways (accounted as segments in the following analysis) are effectively interconnected pores but not all the pores, especially the smallest ones, can be considered as pathways. A skeletonization procedure (conversion from pores to segments) of the porous section has allowed to quantitatively evaluate the length of the pathways and the tortuosity. At the same time, as a constraint parameter, in order to preliminary discard the lowest length segments, a default minimum threshold of 10 pixels (corresponding to 0.0995 mm) has been set. The procedure of conversion of pores into segments (skeletonization), which can be applied on both cross and coronal section slices, widely explained in Section 3, is showed in Figure 69.

In Table 12 tortuosity results has been calculated, amongst different definitions [69], with the equation:

$$\tau_{ave} = \frac{L_{path}}{D_{endpoints}}$$

Where  $L_{path}$  is the actual pathlength of the skeletonized segments and  $D_{endpoints}$  is the minimum Euclidean distance among the endpoints of the tortuous segments.

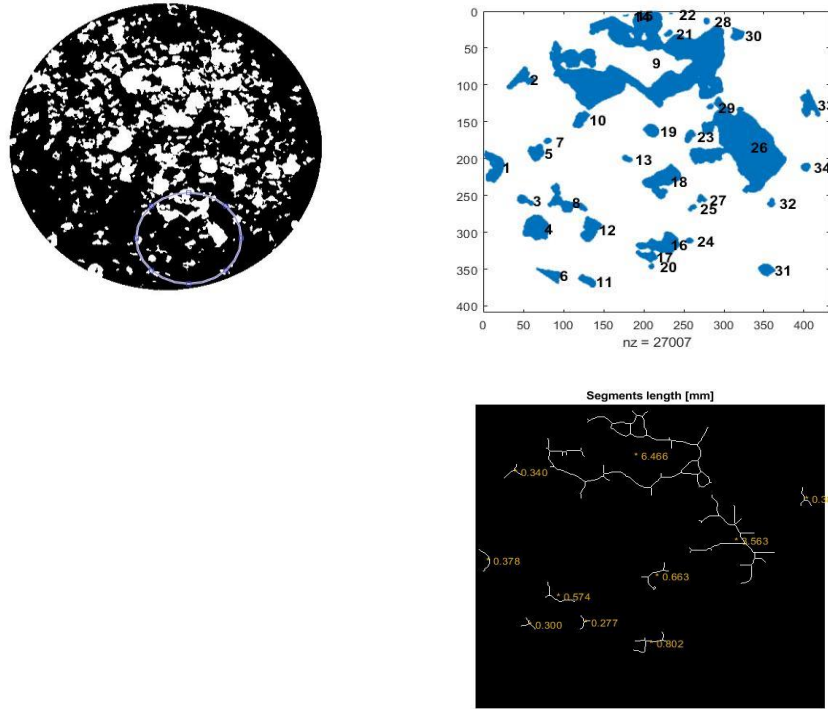


Figure 69 - Object analysis by digital imaging techniques.

Table 12 – Tortuosity analysis on coronal sections for samples S701, S705, S710.

SS	N <sub>pores</sub>	ε <sub>2D</sub> %	Av. Stretch %	Nseg	L <sub>ave,path</sub> [mm]	τ <sub>av</sub>	Nseg/ N <sub>pore</sub> %
S701	129	55.41	78.09	29	1.103	1.60	24.81
S705	246	38.25	72.95	95	0.848	2.316	27.86
S710	219	33.94	72.96	69	0.753	1.164	31.51

The comparative cross-analysis between porosity and tortuosity clearly highlights a connection among porosity and leakage in both the reference planes, showing a progressive increase in porosity in samples with decreasing loadings of graphite. Tortuosity on the other hand proved to be a less straightforward parameter, so that a correlation among those parameters on both planes has been necessary. Considering the following quantities evaluated on both directions:

$$\varepsilon_{\%} = (\varepsilon_{xy}, \varepsilon_{xz})$$

$$\pi_{pore\%} = (\pi_{xy}, \pi_{pore_{xz}})$$

$$\tau_{ave} = (\tau_{xy}, \tau_{xz})$$

Considering pores as statistically distributed and porosity and pore stretching as two mutually independent quantities, a joint probability parameter has been defined. This should refer to the likelihood to find more elongated pores in the sample as follows:

$$\varepsilon'_{\%} = \varepsilon_{\%} * \pi_{pore\%}$$

As a final step, tortuosity has been correlated to this index by collecting data on both directions from three surfaces for each sample. Graphical results of this set of data shown in Figure 70 highlights that overall, the gradual increase of this joint probability may correspond to the increasing likelihood of leakage (the sample results have been grouped accordingly). Moreover, while tortuosity is more uniformly distributed around smaller values on the xy plane for all the samples, on the other hand it presents higher and more dispersed values through coronal sections, the increased average tortuosity in z-direction proves that this is the actual preferential direction for network microstructures formation and thus leakage. Conclusively, samples S705 but especially S701 are those with both the highest probability of having pathway-like and interconnected (tortuous) pores in both directions. This representation supports the theory that more porous and tortuous pellets leads to leakage and that a maximum threshold porosity (percolation probability) must exist to maintain shape-stability as for sample S710.

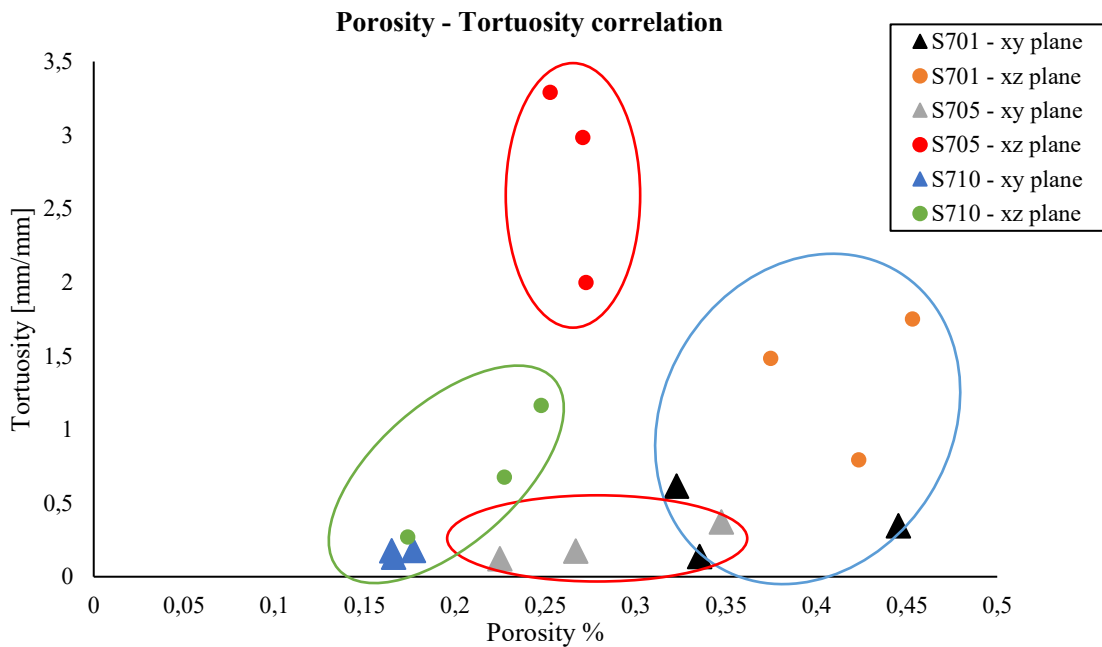


Figure 70 - Porosity-Tortuosity correlation of three example results obtained from each surface (cross and coronal section) of each sample tested (S701/S705/S710).

## 5 Considerations on the development of a LHTES device

Considering the mature level in the knowledge of the basic principles lying behind the LHTES concept, some performance and basic economic indicators may facilitate the Shape-stabilized PCMs penetration into the market from an experimental and laboratory scale to a commercial one. It is believed that once such TES technologies are fully scientifically validated, the volume in the market of such technologies will increase and in the meanwhile the storage costs connected to them will decrease, making them more affordable.

In this final section, a general cost and sizing procedure is developed, with the intention to be a starting tool allowing to understand the behaviour and the link of some sizing parameters and how their variation, considering some design constraints, may affect the overall economic value of a general FPCM-based device. This general cost and sizing procedure relies on a high-level parametric study not involving any thermo-physical modelling of the LHTES device proposed. The method introduced could be referred to by suppliers or stakeholders to have a starting understanding of the links between prices along with some design considerations.

### 5.1 Conceptual design and system requirements

The definition of a FPCM's formulation along with the investigation on its thermophysical properties is not a standalone issue, it is indeed strictly linked with the applicability of its pellets into a device for large-scale systems. The investigated properties must cope with challenges that are still open in the research world and that can pose restrictions for their application. Typical examples are compatibility issues (e.g. corrosion when in contact with containment materials) and thermal stability of the PCMs involved and contained inside the tablets.

Thanks to the experimental achievements discussed in Section 4, the main purpose of this last section is to come up with a high LHTES device which could be integrated a wide variety of sectors where waste heat resulting from processes can potentially be recovered and collected for further and/or parallel uses. As already discussed in Section 1 and 2, waste heat recovery operated by the TES not only contributes to reduce the CO<sub>2</sub> emissions but, if fully integrated in the system, it may allow to reduce primary energy consumption and provide flexibility to the process, while increasing its resiliency. Moreover, whether storing only thermal energy or also contributing to electricity production (e.g. when integrated with CSP plants [70,71] or the lately-investigated ORC plants) it may also contribute to reduce the operating expenses of the plant because it offers the opportunity of scheduling the buying and selling of energy in a more reasonable and affordable way by purchasing for example the energy in periods when it's at lower costs. In the case of active systems, applications where the TES is served for electricity generation purposes, the cost evaluation study must be extended to have a complete and effective estimation of the Levelized Cost of Energy (LCOE), or in the thermal storage field so-called Levelized Cost of Storage (LCOS). As for now, the lack of a specific regulatory framework as well as the very poor presence of FPCMs in the market do not allow to evaluate in a comparative and complete way the actual LCOS value of the single technology when non-coupled with a real production process/facility.

The final task of the study is to assess the applicability of such costing-procedure for the LHTES packed-bed to compare its economic value, along with a few other performance indicators, with the typical values assessed for the Latent Heat technologies outlined by international energy bodies and organizations [72,73] but most of all to assess their economic viability when compared to other solutions like purely Sensible and Thermo-chemical solutions but also, in some extent, with other Energy Storage technologies.

### **Conceptual design**

In this case-study, a packed-bed storage unit assembled with SSPCMs is considered. The procedure proposed may serve as an initial evaluation tool for both decision makers and stakeholders willing to integrate a compact and low-complexity and low cost LHTES storage solution mainly for passive heat recovery purposes as a first estimation of the expenditures related with amounts of materials and basic operational costs required for its realisation.

It must be highlighted that the cost value obtained is strictly connected for the specific case of SSPCMs in the medium melting temperature range and in direct contact with the Heat Transfer Fluid (HTF) but it can be extended to other SSPCMs adopting other PCM materials along with alternative manufacturing procedures, whether is possible to make an estimation of the manufacturing or extra treatment costs to take into account. Additional care must be taken when choosing the right HTF in direct contact to couple the LHTES with, if all the materials compatibility requirements mentioned throughout are met, this kind of SSPCM-based device is expected to require very low maintenance and amount of containment materials involved, thus related costs. The main cost contribution is indeed expected to be the storage material's costs.

Amongst the different possible layouts and solutions which can be adopted for the LHTES, the system considered for the study is an open-system composed by a single-tank dual-media device with the HTF in direct contact and in forced convection through the storage medium. The packed-bed considered overall is not only a PCM-based device but also can be considered as a sensible storage unit. The HTF chosen is air and it is itself a heat transfer medium allowing to collect heat during the charging phase and releasing and delivering it during discharge cycles. The adoption of a single-tank system imposes some limitations from a design point of view. Particularly, in order to keep the packed-bed well stratified, the HTF should flow from bottom to top so that the hot fluid is always placed in the upper part of the tank while the cold part is always to the bottom, this is needed to avoid mixing and as a consequence, temperature degradation. However, when thermal conversion and the transfer from one medium to the other are involved, after some cycles, some temperature degradation is inevitable during the transient, leading to lower energy storage efficiencies (also a non-complete discharge process might contribute). Additionally, the HTF flow rate must be sufficiently high to increase the heat transfer rate between the HTF and the storage medium but not too high because it would increase side and interparticle effects leading to higher thermal losses and pressure drops in the tank. The increasing impact of losses would also increase the extent of complexity of the design, and in such case, these effects must be taken into account for numerical 1D or 2D models to determine temperature evolution and their assumptions might not be sufficient but a more detailed CFD analysis might be required.

The selection of the packed-bed system with flowing air is connected not only to economic reasons, for its wide and free-of-charge availability, but also for material compatibility

reasons, both with PCM itself and for its low corrosion with pipes and containments of the system. Some non-encapsulated FPCMs may indeed react chemically with other fluids, so that this could compromise significantly the efficiency of the heat transfer and reduce the lifetime of the materials of all the components involved at a device scale. This is also the reason why other HTF are carried inside shell-and-tube or tube in tanks or other layouts widely studied in literature. [74–78]

The conceptual scheme considered for the LHTES referred to is shown in Figure 71.

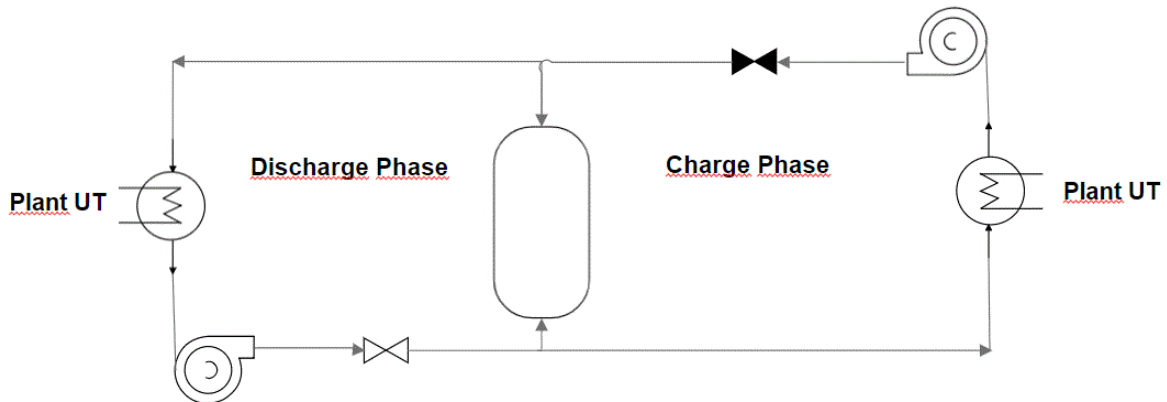


Figure 71 – Basic LHTES system layout

## 5.2 Cost of Storage evaluation methodology

In a first stage of the analysis, in order to drive the cost and materials evaluation of the storage unit, a starting 1 MWh of thermal energy stored has been considered. A scalable procedure can then be performed by setting some fixed design parameters in accordance to reported values from literature (e.g. porosity of bed in the range 0.3-0.4). In a second stage, another containment solution has been proposed to compare the impact of encapsulation costs when compared to the SSPCMs.

For the first part of the analysis, some necessary assumptions and restrictions of the proposed packed-bed procedure include:

- No heat-transfer numerical model or CFD software is applied to assess the transient temperature evolution during the charging/discharging phases, this study doesn't refer to a detailed packed-bed performance analysis. Detailed and computationally intensive further analysis could drive the evaluation of the effectiveness of the storage unit with the specific SSPCM in a more realistic way;
- No system coupled with the LHTES has been taken into account, the procedure is intended to investigate cost value of the sole storage unit;
- Spherical pellets are homogeneously arranged with a fixed porosity into the tank (Figure 72), alternative shapes can be assessed to extend this method thanks to the aid of more detailed heat transfer models;
- The HTF flow rate is constant in both charging/discharging phases as well as temperatures at the hot and cold sides of the packed-bed are set;

- As a simplifying assumption, all the heat stored is totally transferred through the contact surface to the HTF throughout the bed;
- For the Capital cost of storage estimation, the cyclic yearly operation is not considered. As defined in [73] the investment cost depends heavily on the number of charging/discharging cycles per year according to the final application of the storage unit.

The procedure has been driven by fixing some design and operating parameters as detailed into Table 13. For Case 1, the thermo-physical properties of the FPCMs spherical pellets collected from the experimental characterization are listed in Table 14.

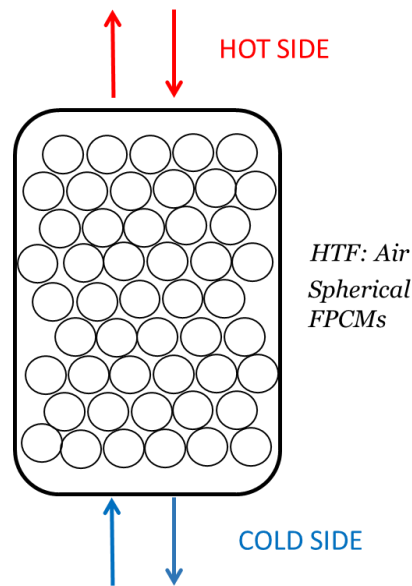


Figure 72 - Packed-bed scheme with spherical FPCMs arranged inside.

Table 13 - Design parameters for cost procedure.

Input design parameters	Value	U.M.
$\varepsilon$	40	%
$d_p$	0.05	m
Thermal energy stored	1	MWh
Power	0.166	MW
$D_t$ [m]	3	m
Charging/discharging time	6	hours
$T_{pcm,max}$	300	°C
$T_{air,in}$	50	°C
$T_{air,out}$	250	°C
$\eta_{fan}$	0.95	

Table 14 - HTF thermo-physical properties.

HTF properties:	Value	U.M
C <sub>p,htf</sub>	1.005	kJ/(kg*°C)
Cinematic viscosity $\tau$	1.50E-05	m <sup>2</sup> /s
Density $\rho_{htf}$	1.225	kg/m <sup>3</sup>
Dynamic viscosity $\mu_{htf}$	1.84E-05	Pa*s
Thermal conductivity $k_{htf}$	2.500E-05	kJ/(m*°C)
Prandtl Number Pr	0.739	

Table 15 - FPCMs thermo-physical properties.

Case 1: Form-Stable PCM (FPCM)	Value	U.M.
Specific heat C <sub>p,pcm</sub>	1.535	kJ/(kg*°C)
Density $\rho_{fpcm}$	1600	kg/m <sup>3</sup>
Thermal diffusivity $\alpha$	8.12E-04	m <sup>2</sup> /s
Thermal conductivity k <sub>pcm</sub>	1.99E+00	W/(m*°C)
Latent Heat $\Delta H_L$	79	kJ/kg
Energy density E <sub>fpcm</sub>	386	kJ/kg
T <sub>max,pcm</sub> [°C]	300	

Some of the main steps for the cost and sizing approach by setting a starting storage capacity of 1 MWh of the unit, have been listed below:

1. Heat transfer rate:

$$P_{th} = \frac{E_{th}}{\Delta t_{dis}} \quad [\text{kW}]$$

According to the assumptions previously mentioned, all the heat stored is supposed to be delivered entirely to the HTF. In more detailed performance analysis the amount of heat exchanged should be weighted by a heat transfer coefficient (effectiveness of the packed-bed widely assessed in literature [79–81]). This assumption allows to calculate the flow rate of the air which has to be blown inside the storage unit.

2.  $m_{HTF} = \frac{P_{th}}{c_{pHTF} * \Delta T} \quad \left[ \frac{\text{kg}}{\text{h}} \right]$

3. A size parameter should be set, in this case a 2 meters diameter for the thermocline has been set, this may allow to evaluate the cross-sectional area of the tank;

4. Known the PCM energy density, the actual volume of the PCM bed is derived from:

$$V_{bed} = \frac{E_{th}}{\rho_{fpcm} * E_{fpcm}} \quad \rightarrow \quad \left[ \frac{\text{kJ}}{\frac{\text{kg}}{\text{m}^3} * \frac{\text{kJ}}{\text{kg}}} \right] = \text{m}^3$$

As a consequence, the mass of the PCM bed is:

$$M_{fpcm} = \rho_{fpcm} * V_{bed}$$

5. The number of PCM spheres to arrange into the packed-bed:

$$N_{pellets} = \frac{V_{bed}}{V_{pellet}}$$

6. The porosity of the bed allows to calculate the volume and the height of the tank:

$$V_t = \frac{V_{bed}}{1-\varepsilon}$$

$$L_t = \frac{V_t}{\pi * \frac{D_t^2}{4}}$$

7. Estimate the pressure drops into the tank according to the Ergun equation widely used in literature [82–84]:

$$\frac{\Delta P}{L} = 150 * \mu_{htf} * \frac{(1-\varepsilon)^2}{\varepsilon^3 * d_p^2} * v_{htf} + 1.75 * \rho_{htf} * \frac{1-\varepsilon}{\varepsilon^3 * d_p} * v_{htf}^2$$

Where the thermo-physical properties are defined in Table 14 and are related to the heat transfer fluid (air in forced convection). The empirical Ergun correlation allows to estimate the pressure losses in a generic packed-bed reactor according to the nature of the fluid flowing throughout, whether turbulent or laminar.

8. Calculation of the velocity of the HTF inside the tank:

$$v_{htf} = \frac{m_{htf}}{\rho_{htf} * S_t} \quad [\text{m/s}]$$

9. Power to operate the air fan/blower:

$$P_{fan} = m_{htf} * \frac{\Delta P}{\rho_{htf}}$$

By following this procedure and by considering the unit price values listed in Table 16, collected from literature and open-web sources from suppliers (Stainless steel is the commodity price) it is possible start the cost estimation.

Table 16 - Unit prices for materials and equipment taken from literature and open-web sources. (a), (b) and (c) are calculated referring, as a starting point, to a 1 MWh thermal energy stored.

Unit prices and tank material properties:		U.M.
Electricity price	0.13	\$/kWh
Stainless steel price (SS)	3.82	\$/kg
SS density	7700	kg/m <sup>3</sup>
SS commodity price	29414	\$/m <sup>3</sup>
Fiberglass (E glass)	2	\$/kg
Fiberglass density	2600	kg/m <sup>3</sup>
unit price	5200	\$/m <sup>3</sup>
Pellet materials cost	1.4	\$/kg
Foundation price	1210	\$/m <sup>2</sup>
(a)	3.80	\$/kWh
Electrical and instrumentation costs (b)	0.53	\$/kWh
Piping, valves, and fittings costs (c)	0.23	\$/kWh
HTF	0	\$

Foundations, electrical and other costs have been evaluated over kWh energy stored, as a consequence they would vary according to the amount of energy stored and the size of the thermocline considered. While foundation unit cost depends on the basement surface, piping and instrumentation prices have been evaluated by means of some correlations from peer-reviewed articles [71,85,86], altogether accounting for 10% of the total tank materials price according to (a) and (b).

$$(b) \quad C_{el\&instr} = 7\% * (C_{SS} + C_{ins} + C_{found})$$

$$(c) \quad C_{piping} = 3\% * (C_{SS} + C_{ins} + C_{found})$$

In order to evaluate the Capital and Operational Costs, CAPEX and OPEX respectively, some further steps are listed below:

10. Cost to operate the fan/blower:

$$C_{fan} = el. price * P_{fan}$$

11. Indirect costs connected to operation and maintenance of instrumentation and piping:

$$C_{ind} = 20\% * (C_{fan} + C_{piping} + C_{el\&instr})$$

12. Cost of FPCM-bed per unit of energy;

$$C_{bed} = C_{fpcm} * \frac{M_{fpcm}}{E_{th}} \quad \left[ \frac{\$}{kWh} \right]$$

13. Tank materials evaluation:

- Stainless steel:

$$V_{SS} = \pi * \frac{(D_t + thickness)^2}{4} - \pi * \frac{(D_t)^2}{4}$$

$$C_{SS} = V_{SS} * \frac{C_{steel}}{E_{th}} \quad \frac{[m^3] * \left[ \frac{\$}{m^3} \right]}{[kWh]} \quad \rightarrow \quad \left[ \frac{\$}{kWh} \right]$$

- Insulation option 1: Fiberglass (E-glass)

$$C_{ins} = V_{ins} * \frac{C_{ins}}{E_{th}}$$

14. The Capital Cost of Storage estimation over stored capacity CAPEX\* [\$/kWh] is the cost evaluated by considering all the capital costs of both storage and containment materials as well as installation and instrumentation costs (it refers to the actual CAPEX).

$$CAPEX^* = C_{found} + C_{instr\&el} + C_{piping} + C_{aux} + C_{indirect} + C_{SS} + C_{ins} + C_{bed}$$

15. Another costing parameter which may be useful as an index to drive the sizing procedure for the storage unit, it has been called Total Cost of Storage (CoS) accounting for both CAPEX but also the OPEX connected to the operating of the blower. It is necessary to highlight that all the costing indexes for this procedure have been considered per unit of kWh stored.

$$C_{tot} = CAPEX + OPEX \quad [\$]$$

$$OPEX = el. price * E_{fan} \quad [\$]$$

$$CoS = \frac{CAPEX^* * CRF + el. price * E_{fan}}{E_{stored}}$$

Where the CFR is the Capital Recovery Factor considering a lifetime of 30 years.

The first results obtained from this parametric study are shown in Figure 73 which highlight, in a first stage how the storage costs indexes evaluated change when scaling-up the device storage capacity specifically from 100 kWh, 300 kWh, 500 kWh, 1 MWh, 2 MWh, 5 MWh to 10 MWh. The main design parameters fixed according to Table 13 regards a 2 meters diameter and 6 hours charge/discharge packed-bed with spherical pellets of FPCMs arranged in the tank with a porosity of 40%.

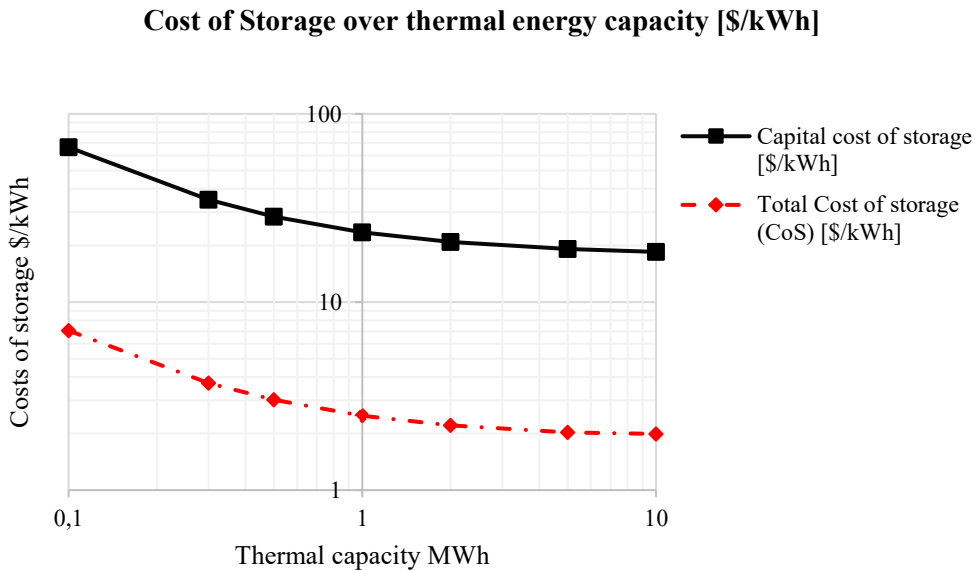


Figure 73 - Sizing procedure according to Costs of storage variations.

As shown in Figure 73, by increasing the storage capacities for the proposed packed-bed, the Capital Cost of Storage (CAPEX\*, black line), which depends on materials and installed equipment costs, has a decreasing trend stabilizing towards values around 20 \$/kWh. This trend suggests that the materials' costs like foundations are too high for lower storage capacities, or the materials are not effectively exploited. In conclusion, higher storage capacities might guarantee a better exploitation of the materials. Total cost of storage CoS shows on the other hand an almost identical trend due to the low impact of the costs for operating the blower for the proposed packing.

According to the cost of storage estimated, in order to visualize the impact of the several cost components, a pie chart corresponding to 1 MWh storage capacity of the packed-bed is shown in Figure 74. In the same way, by increasing or decreasing the storage capacity of the packed-bed proposed, the cost components would affect in a different extent onto the final cost of storage. An example Figure 75, referred to a 500 kWh-capacity, underlines that for lower storage capacities, components like foundations have a higher impact onto the final cost of storage while insulation and tank materials have almost the same impact as well as other auxiliaries' costs. As expected, viceversa for higher storage capacities, the PCM cost has a significant impact on the final storage cost, while for 1-2 MWh it ranges around 60%. However, costs of storage materials may vary greatly

according to the fluctuations of prices in the market and on the supplier but especially on the formulation of the composites.

### Cost Components - 1 MWh Storage Capacity

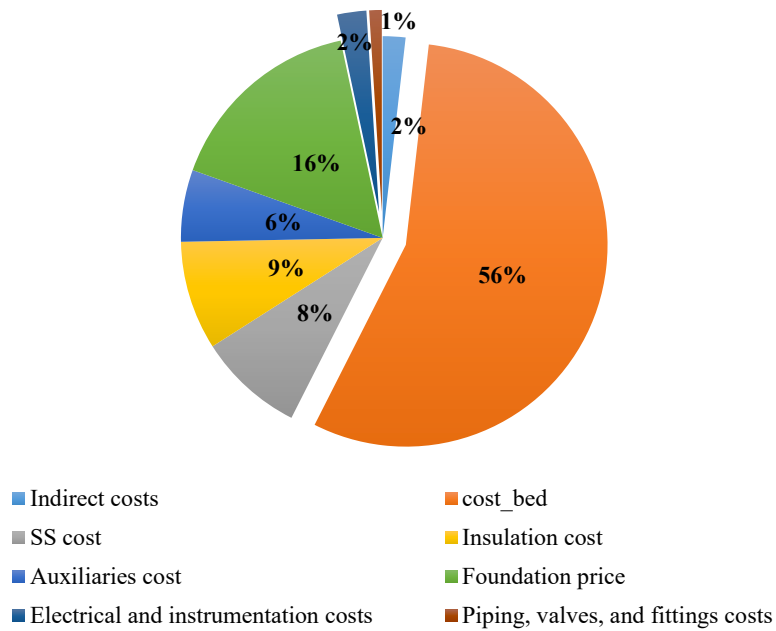


Figure 74 - Pie chart related to the cost components for a 1 MWh-storage capacity tank.

### Cost Components - 500 kWh Storage Capacity

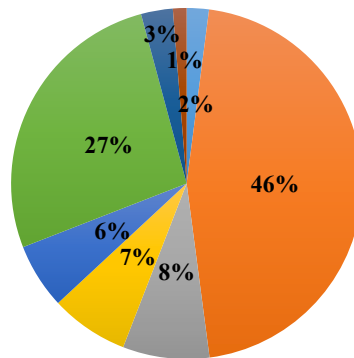


Figure 75 - Pie chart related to the cost components for a 500 kWh-storage capacity tank.

In particular, due to the scarcity in the market of pre-formulated and commercialized FPCMs, a variation in the prices of the presented S710 formulation, by considering a 1-2 MWh storage capacity option, from the starting value of 1.4 \$/kWh is proposed. PCM prices considered are +20%, +50%, +75% of the original PCM price and -20% up to -50%. The trend obtained with price variation is shown in Figure 76 where a linearly proportional increase of the capital cost of storage is detected. In figure 76 is also evident that for higher storage capacities the capital cost of storage is more restrained and this may

be due to a better exploitation of the storage material and a decrease on the foundations costs (expressed in \$/kWh stored). The change of the capital cost of storage is the primary index to immediately evaluate the storage potential of TES technology by tracking the PCM price variation.

Despite the variability of the prices of materials involved, it is believed that once characterized and fully controllable from a structural and manufacturing point of view, the form-stable PCMs, as well as other TES would experience in the next future a decrease in price.

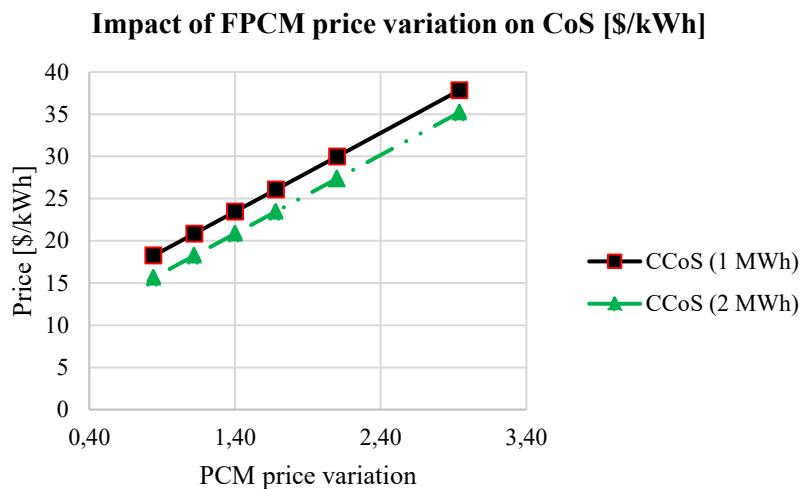


Figure 76 - Influence of the variation of PCM priced on a 1 MWh and 2 MWh capacity storage unite. Comparison between Total Cost of Storage (CoS) and Capacity Cost of storage (CAPEX\*).

Several are the additional design parameters which can be assessed for the realisation of the packed-bed by adopting this scalable procedure, an example is shown in Figure 77 where the capital cost of storage is assessed over aspect ratio corresponding to different scalable storage capacity in the range 100 kWh, 300 kWh, 500 kWh, 1 MWh, 2 MWh, 5 MWh to 10 MWh. Clearly, too high aspect ratios are not logical and practically feasible, by fixing as size parameter 2 meters height of the tank so that, to contain the cost of storage, the optimal size for the storage unit is located in the shoulder area for both the lines, namely between 500 kWh and 2 MWh. The alternative to scale-up to higher storage capacities would be to increase the diameter size of the packed-bed according to: some space constraints or according to a specific volume which corresponds to a certain amount of FPCM which is related to a specific storage capacity.

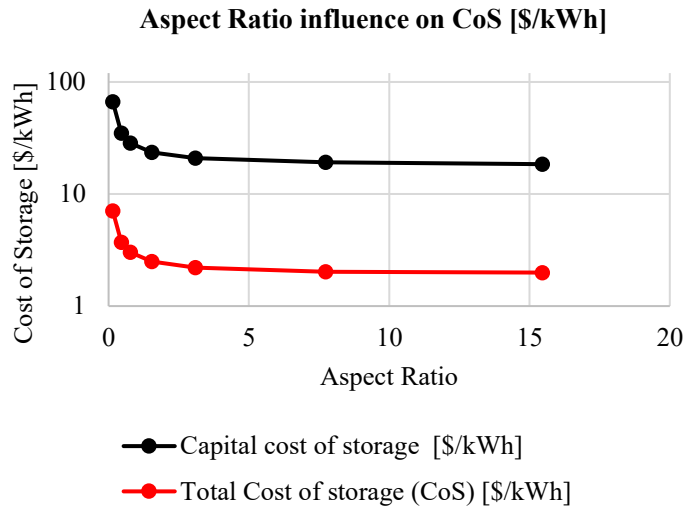


Figure 77 - Costs of Storage variations according to different aspect ratios.

Another correlation which may be useful to make design considerations is the dependency of the aspect ratio (with a fixed 2 meters diameter of the tank) from variable porosities of the bed and with variable storage capacities. As shown in Figure 78, the aspect ratio and as a consequence, the volume of the packed-bed, have an exponential trend increasing with higher capacities for the tank. The increase of the porosity lead to lower volumes (of the tank) for lower storage capacity of the TES, this means that more flexibility is allowed when choosing the packing-ratio of the pellets inside the tank and acceptable aspect ratios during the design phase. On the other hand, should higher storage capacity be the most important target, lower porosities should be selected, although not lower than 20% to accommodate the FSPCM volume expansion and additionally, for structural safety issues, the height of the tanks should not higher than twice the diameter, otherwise the best option would be to re-size the tank with another diameter than the one proposed. From Figure 78 and for this specific case with a 2 meters diameter, the ideal storage capacity would be included between 1 and 2 MWh.

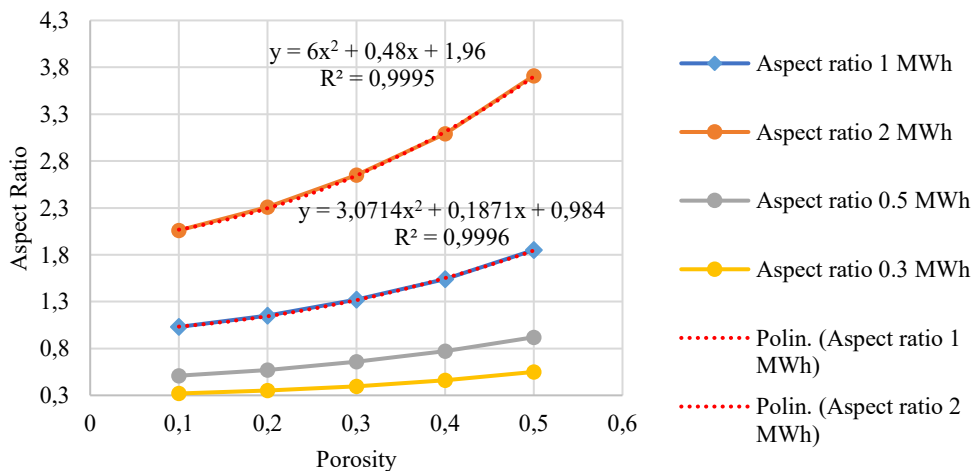


Figure 78 - Aspect Ratio variation with different porosity values of the packed-bed for the packing of FPCMs spherical pellets.

## Case 2: EPCMs

In order to set up a cost of storage comparison with Case 1, an alternative solution for LHTES with EPCMs is proposed by adopting the same layout, materials and functioning principle for the packed-bed. As a PCM a composition of the same Solar Salt and Graphite is considered, the application of Vermiculite in this case is avoided to avoid increased contact resistance between the HTF and the shell-based components. The solution proposed relies on a widely used method in industry called fluid coating process and it has been adopted for producing the shells around the PCM-graphite formulations. The procedure consists on a first coating step for a PCM prill which decomposes with heat creating a void space inside the shell which is further coated in a second phase by another surfactant. The presence of the void fraction is meant to accommodate volume expansion of the salt during melting. This process is referenced and detailed by Mathura et al' in [86] and showed in Figure 79. This process with its related prices has been selected for comparison purposes with a peer-reviewed paper, where compatibility issues between a nitrate salt and a polymer have been already tested and guaranteed [86,87]. All the starting design, operating and costing parameters have been maintained constant as given in Table 13 and results in Table 17.

For comparison between Case 1 and Case 2 the cost and sizing procedure should not be affected by significant changes considering this as a preliminary and general method to evaluate the feasibility of a LHTES-based solution. The only variations consist onto some physical properties of the PCM/Graphite formulation (75% and 25% wt% respectively) which have been averaged relying on existing properties and a few additional consideration on encapsulation expenditures referenced in both [86] and [85].

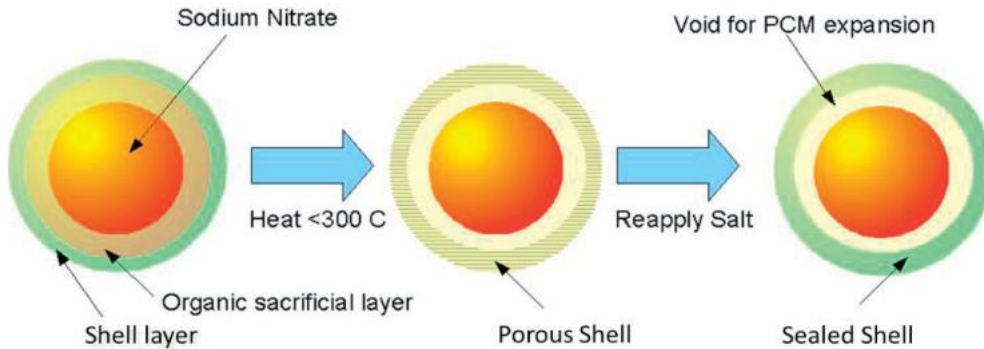


Figure 79 - Example of EPCMs by fluidized bed coating process referenced by Marturi et al's in [86].

Based on fabrication costing correlations recalled and outlined by Jacob et al's, the cost for EPCM by fluidized bed method is deduced by:

$$16. C_{EPCM_{fb}} = \left( \frac{r_{shell}}{0.005} \right)^{0.3} * C_{ref}$$

$$17. C_{EPCM_{tot}} = C_{EPCM_{fb}} * m_{PCM}$$

where  $C_{ref}$  is the reference cost for encapsulating an already-tested PCM by means of the same technique and equals 0.75 \$/kg (Nithyanandam and Pitchumani, 2014).

Unit costs for the storage media are summarized in Table 14.

Table 17 - Unit prices considered between Case 1 and Case 2.

	PCM formulation	PCM price [\$/kg]	Cost shell [\$/kg]	Cost HTF [\$/kg]
Case 1	75% SS / 15% Vermiculite/ 10% Graphite	1.4	/	/
Case 2	75% SS/ 25% Graphite	1.63	1.4	/

Results obtained from a first analysis with a 1 MWh storage capacity are shown in Table 18 while the detailed cost composition for Case 1 and 2 is shown in Figures 80-81. Where in Table 18 the cost of PCM formulation is different due to higher cost of the formulation chosen for Case 2: higher amount and price of Graphite.

Table 18 - Case 1 and Case 2 comparison: Capital cost of Storage estimation.

	Cost of PCM [\$/kWh]	Cost of EPCM [\$/kWh]	Capital Cost of Storage [\$/kWh]
Case 1	13.06	/	23.15
Case 2	17.97	15.43	45.6

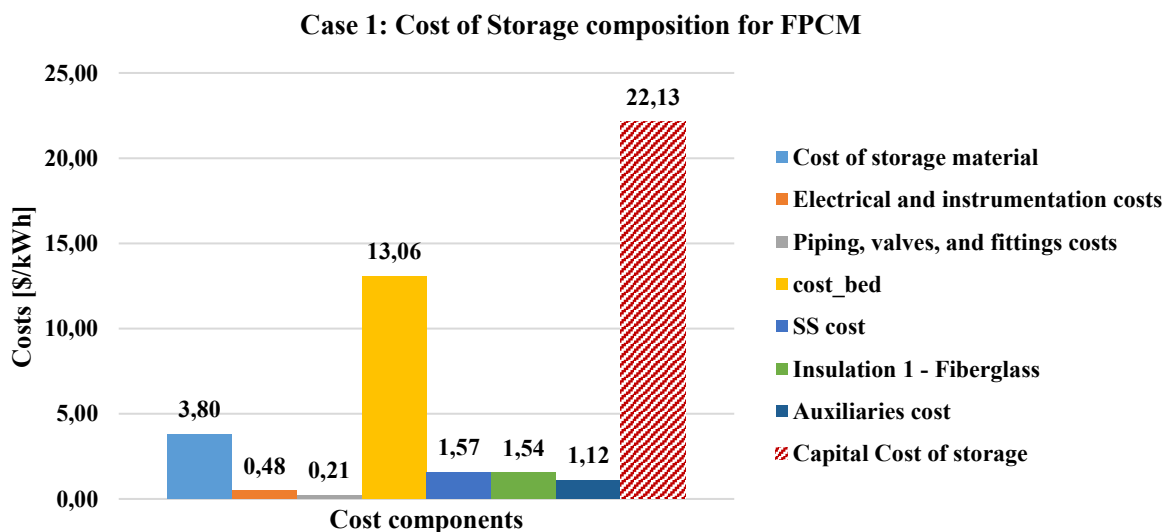


Figure 80 - Cost composition for Case 1 of the Form-stable PCM-based packed-bed.

### Case 2: Cost of Storage composition for EPCM

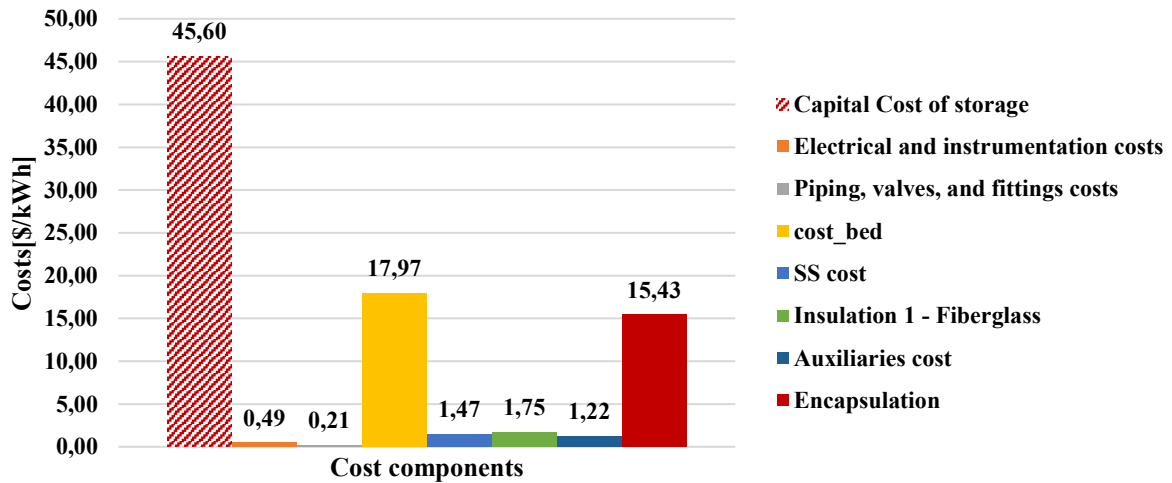


Figure 81 - Cost composition for Case 2 of the Encapsulated PCM-based packed-bed.

From the comparison it is evident the increase in the capital cost of storage of Case 2 is highly increased compared with Case 1. The cost of the storage material in Case 1 accounts for 56% of the Capital Cost of storage with a value of 1.02 \$/kWh while in Case 2 the high impact of the cost for encapsulation accounts for around 33% in the Capital Cost of Storage with a lowered 39% with 17.97 \$/kWh as for the cost of the PCM material (cost of the bed). Moreover, in Case 2 the PCM cost has increased due to a higher amount of graphite content in the PCM formulation with the idea of increasing the thermal conductivity against the increased thermal resistance procured by the interposition of the shell. In both cases however, the Capital Cost of storage is included in the range reported by IRENA [73][72] ranging between 10-50 \$/kWh calculated for the LHTES technologies. Even though highly dependent on storage materials' costs, the comparison between Case 1 and Case 2 allowed to confirm the potential of FPCMs to reduce the costs of storage per unit storage capacity while keeping its higher energy density potential which can be suitable for a wide variety of highly energy-intensive application sectors with waste heat gaseous sources (e.g. glass wares, stainless steel and cement plants) where the recovery of such sources can bring additional revenues both from primary energy consumption point of view and eventually for electricity production purposes.

### Conclusions

The present work has dealt with the selection, formulation, fabrication and testing of a novel composition of Form-Stable Phase-Change material for Latent Heat Thermal Energy Storage purpose. In order to demonstrate its high energy potential, the selection, formulation and characterization of the materials involved have been unfold.

The main focus of the experimental analysis has been primarily devoted to address the form-stability concept linked to a multi-component composite. The identification of a final high energy density formulation with 75% Solar Salt, 10% Graphite and 15% Vermiculite is a direct consequence cross-linked performance and low costs requirements. The high-thermal capacity of the supporting material Vermiculite and enhanced thermal conductivity of the added Graphite proved the studied formulation to be a valid option for waste heat recovery purposes in the medium-to-high melting temperature and allowing to exploit heat from a wider range of operating temperatures from ambient to 220-250°C by storing also the fraction of sensible heat.

The deep micro-structural and morphological analysis provided fundamental tools to shed a light onto novel-manufactured FPCMs and along with other thermo-physical properties investigated contributed to demonstrate the high-reproducibility, controllability of fabricating parameters and cost-effectiveness of the specific manufacturing procedure involving mixing, cold-compressing and final sintering of pellets-shaped composites. The state of the art on FPCMs is highly fragmented on such topic, both from composites characterization and for what univocal explanation of the reasons underlying shape-stability.

The gain from high-quality experimental analysis has highlighted that form-stability and heat transfer enhancement of the manufactured pellets is strictly connected and indiscernible from the typology of materials involved and of the chosen manufacturing process and the variable parameters connected with it. Methods like actual sintering over 1000°C temperatures and infiltration or impregnation of the PCM inside a host matrix proved to be more suitable solutions to contain and retain it during phase transitions. On the other side, when dealing with enhanced graphitic formulations, the introduction of graphite in several forms through the adoption of cold/warm compression techniques after mixing in powder form have proved to determine the higher heat enhancement compared to some infiltration and dispersion techniques. Dispersion and stirring for example allow to obtain half of the thermal conductivity enhancement obtained instead with cold compression. (Cabeza et al's, 2017). Cold-compression however generates a general anisotropy of the composite microstructure and properties. Additionally, due to the natural graphite bond structures thermal conductivity is more enhanced in the radial direction than on the axial one.

The currently accepted explanation for achieving shape-stabilized PCMs is mainly connected to the high interfacial energy of the supporting material allowing the PCM in liquid phase to spread and to be held in the host matrix. In fact, thanks to the pressure difference increase with high temperatures, the capillarity forces had pulled the inner PCM viscous grains and allowed rearrangement and densification giving more rigidity to the structure. [23,34,38,41,53,57,88] The final sintering creates a final porous structure which prevents the composite from leakage. The opposite happens with only PCM-graphite composites where salt leakage occurs due to the low interfacial energy of the graphite and the subsequent expansion of the salt vapour phase during melting which lead to expulsion from the matrix of the melted salt itself.

The novelty introduced with this work relies onto the multi-method micro-structural analysis highlighting other possible additional explanation in addition to the currently accepted version. According to this analysis, shape-stability is the outcome of complementary effects when dealing with porous materials constituting a highly-porous matrix, which accounts both for the effect of capillarity forces counterbalanced by interfacial tensions but also

because of fluid-mechanical issues. For some materials, a minimum porosity must be created to accommodate volume expansion meanwhile structurally holding the PCM throughout. Such version has been already indirectly mentioned by some researchers [22] stating that mean pore size of the support must not be too small otherwise heat capacity is reduced and not too large otherwise capillary forces to retain molten pcm are reduced. Some researchers defined the meso-pore radius limit (around 40 nm) acceptable to avoid leakage while guaranteeing good thermal properties [23], in support to this concept others confirmed the importance of tracking the pores diameter as the most significant parameter to avoid leakage of the PCM [89], while others highlighted that the adoption of a porous structuring material with lower average pores size avoids leakage because of stronger capillary forces generated by smaller size pores.[90]

As for the discussion above, it is evident that there is not a univocal and straightforward understanding behind form-stability, especially because no direct and accurate experimental testing exists to address this task. Most of all it is highly material and fabrication method-dependent.

Since it is still an open topic, this work provides more detailed insights on the experimental techniques, properties and post-processing providing guidelines to direct future works in the research field and to spread the knowledge on these relatively-new PCM-based solutions to allow stakeholders and suppliers to produce, distribute and apply these technologies. The poor availability in the market is indeed one of the barriers to overcome to develop such technologies because currently the composites applicability is strictly dependent on his value on the market, which is still quite high compared to other TES solutions as outlined by IRENA, like Sensible solutions with a price ranging 0. 1-10 \$/kWh stored capacity and some Thermo-chemical in the range 8-100 \$/kWh. Latent heat solution, especially FPCMs have the potential to become more competitive and to decrease the current value of 10-50 \$/kWh stored. Table 19 shows the main key performance and cost indicators which may allow the reader to straightforwardly place such technologies in the market and to evaluate their potential and compare them with other solutions. Other cost values like operational costs are connected to the specific size and design proposed for the packed-bed, so that they are not representative of all the cases.

*Table 19 - Key indicators to drive the selection of inorganic-salt and graphitic FPCMs.*

<b>Quantity</b>	<b>Value</b>	<b>U.M.</b>
Energy density	171.56	kWh/m <sup>3</sup>
Specific energy density	107.22	kWh/t
Cost of FPCM	13.06	\$/kWh
Capital Cost of Storage	22.13	\$/kWh

Main indicators in Table 19 are the direct results of the experimental process developed, especially for what energy density values are concerned which are totally performance-related parameters and independent from a device-application. Specific energy density may serve as a tool to firstly estimate the storage potential on 1 ton of FPCMs material and to evaluate how much material would be required for a target thermal load [kWh] to recoup and store.

Energy density on the other hand is an index of the compactness of such solution according to how much energy can be stored in a unit volume, this index provides a straightforward tool for comparison as shown in Figure 82. In Figure 82 the Solar Salt-based FPCM proposed is exactly placed in the nitrates region, proving to be an intermediate and well performing TES when compared to the most widespread sensible medium (water) and other TCM systems. Compared with the FPCM's 171.56 kWh per unit volume, water would need almost twice of the volume space for the same target thermal load. This provide manufacturers an idea of how much space the TES would occupy whether integrated inside a facility/production plant. Additionally, Figure 82 shows that nitrates in general, have the main share for energy storage capacities in the medium to high melting temperatures, being suitable from food processing industries (drying and baking processes), some low temperature pyrolysis processes, PE polymerization processes and other energy intensive processes like waste heat recovery from exhausts of cogenerating plants, from blast furnace of iron and steel industry and cement and glass industries.

Cost parameters in Table 19 on the other hand, provide a sense of the simplest application possible for FPCM, a 40% porous packed-bed has been conceived as the basic layout solution to reduce all the materials and other instrumentation and maintenance costs and maintain their affordable value of 13.06 \$/kWh stored representing around 60% of the total Capital Cost of Storage accounting for 22.13 \$/kWh. From the analysis conducted is evident that the cost evaluation at device-scale is completely materials-driven, both from a preliminary-level analysis and for more detailed further modelling.

Guidelines and commercialization of the FPCM may decrease the storage costs and help decision and policy-makers to favour the FPCM introduction and volume-ramps in the market. Cost-effective manufacturing processes and materials along with the proposed basic conceptual layout for a packed-bed prototype confirms the great future potential of such technologies.

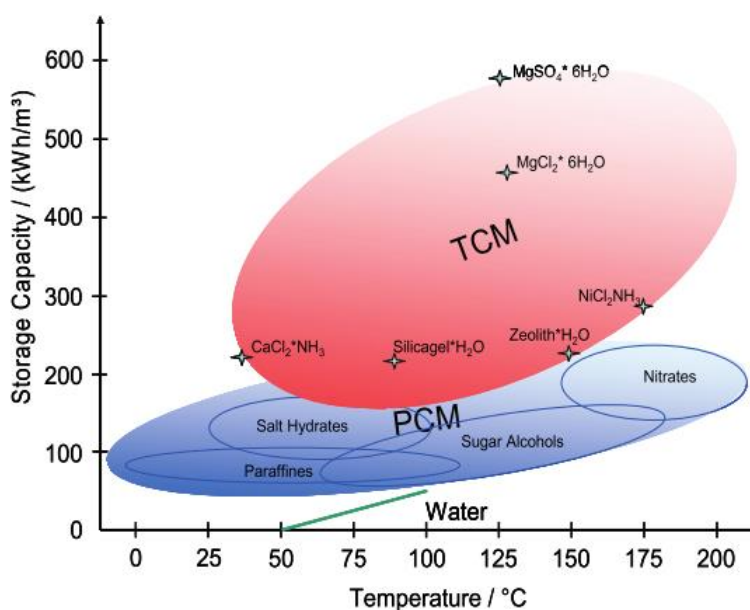


Figure 82 - Technology Roadmap for TES [73]

## Bibliography

- [1] Nithyanandam K, Pitchumani R. Cost and performance analysis of concentrating solar power systems with integrated latent thermal energy storage. *Energy* 2014;64:793–810. doi:10.1016/j.energy.2013.10.095.
- [2] Merlin K, Soto J, Delaunay D, Traonvouez L. Industrial waste heat recovery using an enhanced conductivity latent heat thermal energy storage. *Appl Energy* 2016;183:491–503. doi:10.1016/j.apenergy.2016.09.007.
- [3] Miró L, Gasia J, Cabeza LF. Thermal energy storage (TES) for industrial waste heat (IWH) recovery: A review. *Appl Energy* 2016;179:284–301. doi:10.1016/j.apenergy.2016.06.147.
- [4] [IEA] - International Energy Agency. *World Energy Outlook 2016* 2016. doi:http://www.iea.org/publications/freepublications/publication/WEB\_WorldEnergyOutlook2015ExecutiveSummaryEnglishFinal.pdf.
- [5] Foundation LR. *Foresight review of energy storage energy systems* 2017.
- [6] World Energy Council. *World Energy Resources*. @WECouncil 2016;2007:1–1028. doi:http://www.worldenergy.org/wp-content/uploads/2013/09/Complete\_WER\_2013\_Survey.pdf.
- [7] World Energy Council. *World Energy Resources - E-Storage*. *World Energy Council Rep* 2016;1:60. doi:http://www.worldenergy.org/wp-content/uploads/2013/09/Complete\_WER\_2013\_Survey.pdf.
- [8] Hauff J, Bode A, Neumann D, Haslauer F, Azevedo C, Haischer P, et al. *Global Energy Transitions* 2014.
- [9] Gracia A De, Cabeza LF. Phase change materials and thermal energy storage for buildings §. *Energy Build* 2015;103:414–9. doi:10.1016/j.enbuild.2015.06.007.
- [10] Alva G, Lin Y, Fang G. An overview of thermal energy storage systems 2018;144. doi:10.1016/j.energy.2017.12.037.
- [11] Khan Z, Khan Z, Ghafoor A. A review of performance enhancement of PCM based latent heat storage system within the context of materials , thermal stability and compatibility. *Energy Convers Manag* 2016;115:132–58. doi:10.1016/j.enconman.2016.02.045.
- [12] Agyenim F, Hewitt N, Eames P, Smyth M. A review of materials, heat transfer and phase change problem formulation for latent heat thermal energy storage systems (LHTESS). *Renew Sustain Energy Rev* 2010;14:615–28. doi:10.1016/j.rser.2009.10.015.
- [13] Jamekhorshid A, Sadrameli SM, Farid M. A review of microencapsulation methods of phase change materials (PCMs) as a thermal energy storage (TES) medium. *Renew Sustain Energy Rev* 2014;31:531–42. doi:10.1016/j.rser.2013.12.033.
- [14] Xie N, Huang Z, Luo Z, Gao X, Fang Y. *applied sciences* 2017. doi:10.3390/app7121317.
- [15] Mehling H, Cabeza LF. *2 Solid-liquid phase change materials. Heat Cold Storage with PCM An up to Date Introd into Basics Appl* 2008.
- [16] Wang T, Wang S, Geng L, Fang Y. Enhancement on thermal properties of paraffin/calcium carbonate phase change microcapsules with carbon network. *Appl Energy* 2016;179:601–8. doi:10.1016/j.apenergy.2016.07.026.
- [17] Chen P, Gao X, Wang Y, Xu T, Fang Y, Zhang Z. Metal foam embedded in

- SEBS/paraffin/HDPE form-stable PCMs for thermal energy storage. *Sol Energy Mater Sol Cells* 2016;149:60–5. doi:10.1016/j.solmat.2015.12.041.
- [18] Liang W, Zhang G, Sun H, Chen P, Zhu Z, Li A. Graphene-nickel/n-carboxylic acids composites as form-stable phase change materials for thermal energy storage. *Sol Energy Mater Sol Cells* 2014;132:425–30. doi:10.1016/j.solmat.2014.09.032.
- [19] Xie B, Cheng WL, Xu ZM. Studies on the effect of shape-stabilized PCM filled aluminum honeycomb composite material on thermal control. *Int J Heat Mass Transf* 2015;91:135–43. doi:10.1016/j.ijheatmasstransfer.2015.07.108.
- [20] Guo CX, Ma XL, Yang L. PCM/ graphite foam composite for thermal energy storage device. *IOP Conf Ser Mater Sci Eng* 2015;87. doi:10.1088/1757-899X/87/1/012014.
- [21] Gasia J, Miró L, Cabeza LF. Materials and system requirements of high temperature thermal energy storage systems: A review. Part 2: Thermal conductivity enhancement techniques. *Renew Sustain Energy Rev* 2016;60:1584–601. doi:10.1016/j.rser.2016.03.019.
- [22] Acem Z, Lopez J, Palomo Del Barrio E. KNO<sub>3</sub>/NaNO<sub>3</sub>-Graphite materials for thermal energy storage at high temperature: Part I.-Elaboration methods and thermal properties. *Appl Therm Eng* 2010;30:1580–5. doi:10.1016/j.applthermaleng.2010.03.013.
- [23] Nomura T, Zhu C, Sheng N, Tabuchi K, Sagara A, Akiyama T. Shape-stabilized phase change composite by impregnation of octadecane into mesoporous SiO<sub>2</sub>. *Sol Energy Mater Sol Cells* 2015;143:424–9. doi:10.1016/j.solmat.2015.07.028.
- [24] ma liyun, Guo C, Ou R, sun lichao, Wang Q, li liping. Preparation and Characterization of Modified Porous Wood Flour/Lauric-Myristic Acid Eutectic Mixture as a Form-Stable Phase Change Material. *Energy & Fuels* 2018;acs.energyfuels.7b03933. doi:10.1021/acs.energyfuels.7b03933.
- [25] Yang Y, Pang Y, Liu Y, Guo H. Preparation and thermal properties of polyethylene glycol/expanded graphite as novel form-stable phase change material for indoor energy saving. *Mater Lett* 2018;216:220–3. doi:10.1016/j.matlet.2018.01.025.
- [26] Liu S, Yang H. Stearic acid hybridizing coal-series kaolin composite phase change material for thermal energy storage. *Appl Clay Sci* 2014;101:277–81. doi:10.1016/j.clay.2014.09.002.
- [27] Zhang X, Huang Z, Yin Z, Zhang W, Huang Y, Liu Y, et al. Form stable composite phase change materials from palmitic-lauric acid eutectic mixture and carbonized abandoned rice: Preparation, characterization, and thermal conductivity enhancement. *Energy Build* 2017;154:46–54. doi:10.1016/j.enbuild.2017.08.057.
- [28] Karaipekli A, Sari A. Preparation, thermal properties and thermal reliability of eutectic mixtures of fatty acids/expanded vermiculite as novel form-stable composites for energy storage. *J Ind Eng Chem* 2010;16:767–73. doi:10.1016/j.jiec.2010.07.003.
- [29] Lv P, Liu C, Rao Z. Experiment study on the thermal properties of paraffin/kaolin thermal energy storage form-stable phase change materials. *Appl Energy* 2016;182:475–87. doi:10.1016/j.apenergy.2016.08.147.
- [30] Zhang N, Yuan Y, Yuan Y, Li T, Cao X. Lauric-palmitic-stearic acid/expanded perlite composite as form-stable phase change material: Preparation and thermal properties. *Energy Build* 2014;82:505–11. doi:10.1016/j.enbuild.2014.07.049.
- [31] Sari A, Biçer A. Preparation and thermal energy storage properties of building material-based composites as novel form-stable PCMs. *Energy Build* 2012;51:73–83. doi:10.1016/j.enbuild.2012.04.010.
- [32] Shen Q, Ouyang J, Zhang Y, Yang H. Lauric acid/modified sepiolite composite as a form-stable phase change material for thermal energy storage. *Appl Clay Sci* 2017;146:14–22.

doi:10.1016/j.clay.2017.05.035.

- [33] Xu B, Ma H, Lu Z, Li Z. Paraffin/expanded vermiculite composite phase change material as aggregate for developing lightweight thermal energy storage cement-based composites. *Appl Energy* 2015;160:358–67. doi:10.1016/j.apenergy.2015.09.069.
- [34] Qian T, Li J, Min X, Deng Y, Guan W, Ning L. Diatomite: A promising natural candidate as carrier material for low, middle and high temperature phase change material. *Energy Convers Manag* 2015;98:34–45. doi:10.1016/j.enconman.2015.03.071.
- [35] Jeong SG, Jeon J, Lee JH, Kim S. Optimal preparation of PCM/diatomite composites for enhancing thermal properties. *Int J Heat Mass Transf* 2013;62:711–7. doi:10.1016/j.ijheatmasstransfer.2013.03.043.
- [36] Jiang Z, Leng G, Ye F, Ge Z, Liu C, Wang L, et al. Form-stable  $\text{LiNO}_3$ - $\text{NaNO}_3$ - $\text{KNO}_3$ - $\text{Ca}(\text{NO}_3)_2$ /calcium silicate composite phase change material (PCM) for mid-low temperature thermal energy storage. *Energy Convers Manag* 2015;106:165–72. doi:10.1016/j.enconman.2015.09.035.
- [37] Djefel D, Makhlof S, Khedache S, Lefebvre G, Royon L. Preparation and characterization of stearic acid/olive pomace powder composite as form-stable phase change material. *Int J Hydrogen Energy* 2015;40:13764–70. doi:10.1016/j.ijhydene.2015.05.078.
- [38] Ge Z, Ye F, Cao H, Leng G, Qin Y, Ding Y. Carbonate-salt-based composite materials for medium- and high-temperature thermal energy storage. *Particuology* 2014;15:77–81. doi:10.1016/j.partic.2013.09.002.
- [39] Li R, Zhu J, Zhou W, Cheng X, Li Y. Thermal properties of sodium nitrate-expanded vermiculite form-stable composite phase change materials. *Mater Des* 2016;104:190–6. doi:10.1016/j.matdes.2016.05.039.
- [40] Lv P, Liu C, Rao Z. Review on clay mineral-based form-stable phase change materials: Preparation, characterization and applications. *Renew Sustain Energy Rev* 2017;68:707–26. doi:10.1016/j.rser.2016.10.014.
- [41] Ge Z, Ye F, Ding Y. Composite materials for thermal energy storage: Enhancing performance through microstructures. *ChemSusChem* 2014;7:1318–25. doi:10.1002/cssc.201300878.
- [42] Qin Y, Leng G, Yu X, Cao H, Qiao G, Dai Y, et al. Sodium sulfate-diatomite composite materials for high temperature thermal energy storage. *Powder Technol* 2015;282:37–42. doi:10.1016/j.powtec.2014.08.075.
- [43] Parker WJ, Jenkins RJ, Butler CP, Abbott GL. Flash Method of Determining Thermal Diffusivity, Heat Capacity, and Thermal Conductivity 2003;1679. doi:10.1063/1.1728417.
- [44] Callister W, Rethwisch D. *Materials science and engineering: an introduction*. vol. 94. 2007. doi:10.1016/0025-5416(87)90343-0.
- [45] Marturi N, Demb?? S, Piat N. Scanning electron microscope image signal-to-noise ratio monitoring for micro-nanomanipulation. *Scanning* 2014;36:419–29. doi:10.1002/sca.21137.
- [46] Sim KS, Thong JTL, Phang JCH. Effect of shot noise and secondary emission noise in scanning electron microscope images. *Scanning* 2006;26:36–40. doi:10.1002/sca.4950260106.
- [47] Jain AK. *Fundamentals of Digital Image Processing*. vol. 14. 1989. doi:10.1002/9780470689776.
- [48] Chaubey AK. Comparison of The Local and Global Thresholding Methods in Image Segmentation. *World J Res Rev* 2016:1–4.
- [49] Leszczyński B, Gancarczyk A, Wróbel A, Piątek M, Łojewska J, Kołodziej A, et al. Global and

Local Thresholding Methods Applied to X-ray Microtomographic Analysis of Metallic Foams. *J Nondestruct Eval* 2016;35:1–9. doi:10.1007/s10921-016-0352-x.

- [50] Lam L, Lee SW, Suen CY. Thinning methodologies - A comprehensive survey. *IEEE Trans Pattern Anal Mach Intell* 1992;14:869–85. doi:10.1109/34.161346.
- [51] Leng G, Qiao G, Xu G, Vidal T, Ding Y. Erythritol-Vermiculite form-stable phase change materials for thermal energy storage. *Energy Procedia* 2017;142:3363–8. doi:10.1016/j.egypro.2017.12.471.
- [52] Wen R, Zhang X, Huang Y, Yin Z, Huang Z, Fang M, et al. Preparation and properties of fatty acid eutectics/expanded perlite and expanded vermiculite shape-stabilized materials for thermal energy storage in buildings. *Energy Build* 2017;139:197–204. doi:10.1016/j.enbuild.2017.01.025.
- [53] Lv P, Liu C, Rao Z. Review on clay mineral-based form-stable phase change materials: Preparation, characterization and applications. *Renew Sustain Energy Rev* 2017;68:707–26. doi:10.1016/j.rser.2016.10.014.
- [54] Michot A, Smith DS, Degot S, Gault C. Thermal conductivity and specific heat of kaolinite: Evolution with thermal treatment. *J Eur Ceram Soc* 2008;28:2639–44. doi:10.1016/j.jeurceramsoc.2008.04.007.
- [55] Choi DH, Lee J, Hong H, Kang YT. Thermal conductivity and heat transfer performance enhancement of phase change materials (PCM) containing carbon additives for heat storage application. *Int J Refrig* 2014;42:112–20. doi:10.1016/j.ijrefrig.2014.02.004.
- [56] Xiao X, Zhang P, Li M. Thermal characterization of nitrates and nitrates/expanded graphite mixture phase change materials for solar energy storage. *Energy Convers Manag* 2013;73:86–94. doi:10.1016/j.enconman.2013.04.007.
- [57] Deng Y, Li J, Qian T, Guan W, Wang X. Preparation and Characterization of KNO<sub>3</sub>/Diatomite Shape-Stabilized Composite Phase Change Material for High Temperature Thermal Energy Storage. *J Mater Sci Technol* 2017;33:198–203. doi:10.1016/j.jmst.2016.02.011.
- [58] Cárdenas B, León N. High temperature latent heat thermal energy storage: Phase change materials, design considerations and performance enhancement techniques. *Renew Sustain Energy Rev* 2013;27:724–37. doi:10.1016/j.rser.2013.07.028.
- [59] Xiao J, Huang J, Zhu P, Wang C, Li X. Preparation, characterization and thermal properties of binary nitrate salts/expanded graphite as composite phase change material. *Thermochim Acta* 2014;587:52–8. doi:10.1016/j.tca.2014.04.021.
- [60] Zhang P, Cheng J, Jin Y, An X. Evaluation of thermal physical properties of molten nitrate salts with low melting temperature. *Sol Energy Mater Sol Cells* 2018;176:36–41. doi:10.1016/j.solmat.2017.11.011.
- [61] Serrano-ópez R, Fradera J, Cuesta-López S. Molten salts database for energy applications. *Chem Eng Process - Process Intensif* 2013;73:87–102. doi:10.1016/j.cep.2013.07.008.
- [62] WU Y ting, LI Y, LU Y wei, Wang H fu, MA C fang. Novel low melting point binary nitrates for thermal energy storage applications. *Sol Energy Mater Sol Cells* 2017;164:114–21. doi:10.1016/j.solmat.2017.02.021.
- [63] Suvorov SA, Skurikhin V V. Vermiculite - A promising material for high-temperature heat insulators. *Refract Ind Ceram* 2003;44:186–93. doi:10.1023/A:1026312619843.
- [64] Formula C, Covered T, Leaders T. Graphite ( C ) - Classifications , Properties and Applications of Graphite 2014:2–5. doi:10.1021/ja8021686.
- [65] Chen X, Gao H, Yang M, Dong W, Huang X, Li A, et al. Highly Graphitized 3D Network

Carbon for Shape-stabilized Composite PCMs with Superior Thermal Energy Harvesting. *Nano Energy* 2018. doi:10.1016/j.nanoen.2018.03.075.

- [66] Jiang Z, Ouyang T, Yang Y, Chen L, Fan X, Chen Y, et al. Thermal conductivity enhancement of phase change materials with form-stable carbon bonded carbon fiber network. *Mater Des* 2018;143:177–84. doi:10.1016/j.matdes.2018.01.052.
- [67] Liu Y, Yang Y. Form-stable phase change material based on  $\text{Na}_2\text{CO}_3 \cdot 10\text{H}_2\text{O}$ - $\text{Na}_2\text{HPO}_4 \cdot 12\text{H}_2\text{O}$  eutectic hydrated salt/expanded graphite oxide composite: The influence of chemical structures of expanded graphite oxide. *Renew Energy* 2018;115:734–40. doi:10.1016/j.renene.2017.08.097.
- [68] Tian B, Yang W, Luo L, Wang J, Zhang K, Fan J, et al. Synergistic enhancement of thermal conductivity for expanded graphite and carbon fiber in paraffin/EVA form-stable phase change materials. *Sol Energy* 2016;127:48–55. doi:10.1016/j.solener.2016.01.011.
- [69] Pisani L. Simple Expression for the Tortuosity of Porous Media. *Transp Porous Media* 2011;88:193–203. doi:10.1007/s11242-011-9734-9.
- [70] Galione PA, Pérez-Segarra CD, Rodríguez I, Oliva A, Rigola J. Multi-layered solid-PCM thermocline thermal storage concept for CSP plants. Numerical analysis and perspectives. *Appl Energy* 2015;142:337–51. doi:10.1016/j.apenergy.2014.12.084.
- [71] Glatzmaier G. Developing a cost model and methodology to estimate capital costs for thermal energy storage. Nrel/Tp-5500-53066 2011:21.
- [72] IEA ETSAP, IRENA. *Thermal Energy Storage-Insights for Policy Makers* 2013:9.
- [73] Zhou D, Zhao CY, Tian Y, Lott MC, Kim S-I, Eames P, et al. *Technology Roadmap*. SpringerReference 2013;92:24. doi:10.1007/SpringerReference\_7300.
- [74] Bai F, Wang Y, Wang Z, Sun Y, Beath A. Economic Evaluation of Shell-and-tube Latent Heat Thermal Energy Storage for Concentrating Solar Power Applications. *Energy Procedia* 2015;69:737–47. doi:10.1016/j.egypro.2015.03.084.
- [75] PEI-WEN LI. *Thermal Energy Storage Analyses and Designs*. 2017.
- [76] Belusko M, Tay NHS, Liu M, Bruno F. Effective tube-in-tank PCM thermal storage for CSP applications, Part 2: Parametric assessment and impact of latent fraction. *Sol Energy* 2016;139:744–56. doi:10.1016/j.solener.2015.09.034.
- [77] Castell A, Solé C. *Design of latent heat storage systems using phase change materials (PCMs)*. Woodhead Publishing Limited; 2015. doi:10.1533/9781782420965.2.285.
- [78] Mostafavi Tehrani SS, Taylor RA, Nithyanandam K, Shafiei Ghazani A. Annual comparative performance and cost analysis of high temperature, sensible thermal energy storage systems integrated with a concentrated solar power plant. *Sol Energy* 2017;153:153–72. doi:10.1016/j.solener.2017.05.044.
- [79] Zanganeh G, Pedretti A, Zavattoni SA, Barbato MC, Haselbacher A, Steinfeld A. Design of a 100 MWhth packed-bed thermal energy storage. *Energy Procedia* 2013;49:1071–7. doi:10.1016/j.egypro.2014.03.116.
- [80] Amin NAM, Belusko M, Bruno F. An effectiveness-NTU model of a packed bed PCM thermal storage system. *Appl Energy* 2014;134:356–62. doi:10.1016/j.apenergy.2014.08.020.
- [81] Amin NAM, Bruno F, Belusko M. Effectiveness-NTU correlation for low temperature PCM encapsulated in spheres. *Appl Energy* 2012;93:549–55. doi:10.1016/j.apenergy.2011.12.006.
- [82] Allen KG, Von Backström TW, Kröger DG. Packed rock bed thermal storage in power plants: Design considerations. *Energy Procedia* 2013;49:666–75. doi:10.1016/j.egypro.2014.03.072.

- [83] Scapino L, Zondag HA, Van Bael J, Diriken J, Rindt CCM. Energy density and storage capacity cost comparison of conceptual solid and liquid sorption seasonal heat storage systems for low-temperature space heating. *Renew Sustain Energy Rev* 2017;76:1314–31. doi:10.1016/j.rser.2017.03.101.
- [84] Esence T, Bruch A, Molina S, Stutz B, Fourmigué JF. A review on experience feedback and numerical modeling of packed-bed thermal energy storage systems. *Sol Energy* 2017;153:628–54. doi:10.1016/j.solener.2017.03.032.
- [85] Jacob R, Saman W, Belusko M, Bruno F. Peer Reviewed Paper Techno-Economic Analysis of Phase Change Material Thermal Energy Storage Systems in High Temperature Concentrated Solar Power Plants 2014.
- [86] Mathur A, Kasetty R, Oxley J, Mendez J, Nithyanandam K. Using encapsulated phase change salts for concentrated solar power plant. *Energy Procedia* 2013;49:908–15. doi:10.1016/j.egypro.2014.03.098.
- [87] Cáceres G, Fullenkamp K, Montané M, Naplocha K, Dmitruk A. Encapsulated nitrates phase change material selection for use as thermal storage and heat transfer materials at high temperature in concentrated solar power plants. *Energies* 2017;10. doi:10.3390/en10091318.
- [88] Feng L, Zhao W, Zheng J, Frisco S, Song P, Li X. The shape-stabilized phase change materials composed of polyethylene glycol and various mesoporous matrices (AC, SBA-15 and MCM-41). *Sol Energy Mater Sol Cells* 2011;95:3550–6. doi:10.1016/j.solmat.2011.08.020.
- [89] Nomura T, Okinaka N, Akiyama T. Impregnation of porous material with phase change material for thermal energy storage. *Mater Chem Phys* 2009;115:846–50. doi:10.1016/j.matchemphys.2009.02.045.
- [90] Goitandia AM, Beobide G, Aranzabe E, Aranzabe A. Development of content-stable phase change composites by infiltration into inorganic porous supports. *Sol Energy Mater Sol Cells* 2015;134:318–28. doi:10.1016/j.solmat.2014.12.010.
- [91] Wang X, Yu H, Li L, Zhao M. Research on temperature dependent effective thermal conductivity of composite-phase change materials (PCMs) wall based on steady-state method in a thermal chamber. *Energy Build* 2016;126:408–14. doi:10.1016/j.enbuild.2016.05.058.
- [92] Sharif MKA, Al-Abidi AA, Mat S, Sopian K, Ruslan MH, Sulaiman MY, et al. Review of the application of phase change material for heating and domestic hot water systems. *Renew Sustain Energy Rev* 2015;42:557–68. doi:10.1016/j.rser.2014.09.034.